THE UNIVERSITY OF CALGARY

# AURORA-ASSOCIATED THREE-DIMENSIONAL CURRENT SYSTEM

BY

FENGYING ZHANG

A THESIS

SUBMITTED TO THE FACULTY OF GRADUATE STUDIES

IN PARTIAL FULFILMENT OF THE REQUIREMENTS FOR THE

DEGREE OF MASTER OF SCIENCE

DEPARTMENT OF PHYSICS AND ASTRONOMY

CALGARY, ALBERTA

MAY, 1993

ISBN 0-315-88656-0

Name FENGYING ZHANG

*Dissertation Abstracts International* is arranged by broad, general subject categories. Please select the one subject which most nearly describes the content of your dissertation. Enter the corresponding four-digit code in the spaces provided.

ASTRONOMY AND ASTROPHYSICS | 0606

SUBJECT TERM | SUBJECT CODE

U·M·I

## Subject Categories

# THE HUMANITIES AND SOCIAL SCIENCES

### COMMUNICATIONS AND THE ARTS
Architecture 0729
Art History 0377
Cinema 0900
Dance 0378
Fine Arts 0357
Information Science 0723
Journalism 0391
Library Science 0399
Mass Communications 0708
Music 0413
Speech Communication 0459
Theater 0465

### EDUCATION
General 0515
Administration 0514
Adult and Continuing 0516
Agricultural 0517
Art 0273
Bilingual and Multicultural 0282
Business 0688
Community College 0275
Curriculum and Instruction 0727
Early Childhood 0518
Elementary 0524
Finance 0277
Guidance and Counseling 0519
Health 0680
Higher 0745
History of 0520
Home Economics 0278
Industrial 0521
Language and Literature 0279
Mathematics 0280
Music 0522
Philosophy of 0998
Physical 0523
Psychology 0525
Reading 0535
Religious 0527
Sciences 0714
Secondary 0533
Social Sciences 0534
Sociology of 0340
Special 0529
Teacher Training 0530
Technology 0710
Tests and Measurements 0288
Vocational 0747

### LANGUAGE, LITERATURE AND LINGUISTICS
Language
- General 0679
- Ancient 0289
- Linguistics 0290
- Modern 0291

Literature
- General 0401
- Classical 0294
- Comparative 0295
- Medieval 0297
- Modern 0298
- African 0316
- American 0591
- Asian 0305
- Canadian (English) 0352
- Canadian (French) 0355
- English 0593
- Germanic 0311
- Latin American 0312
- Middle Eastern 0315
- Romance 0313
- Slavic and East European 0314

### PHILOSOPHY, RELIGION AND THEOLOGY
Philosophy 0422
Religion
- General 0318
- Biblical Studies 0321
- Clergy 0319
- History of 0320
- Philosophy of 0322

Theology 0469

### SOCIAL SCIENCES
American Studies 0323
Anthropology
- Archaeology 0324
- Cultural 0326
- Physical 0327

Business Administration
- General 0310
- Accounting 0272
- Banking 0770
- Management 0454
- Marketing 0338

Canadian Studies 0385
Economics
- General 0501
- Agricultural 0503
- Commerce-Business 0505
- Finance 0508
- History 0509
- Labor 0510
- Theory 0511

Folklore 0358
Geography 0366
Gerontology 0351
History
- General 0578
- Ancient 0579
- Medieval 0581
- Modern 0582
- Black 0328
- African 0331
- Asia, Australia and Oceania 0332
- Canadian 0334
- European 0335
- Latin American 0336
- Middle Eastern 0333
- United States 0337

History of Science 0585
Law 0398
Political Science
- General 0615
- International Law and Relations 0616
- Public Administration 0617

Recreation 0814
Social Work 0452
Sociology
- General 0626
- Criminology and Penology 0627
- Demography 0938
- Ethnic and Racial Studies 0631
- Individual and Family Studies 0628
- Industrial and Labor Relations 0629
- Public and Social Welfare 0630
- Social Structure and Development 0700
- Theory and Methods 0344

Transportation 0709
Urban and Regional Planning 0999
Women's Studies 0453

# THE SCIENCES AND ENGINEERING

### BIOLOGICAL SCIENCES
Agriculture
- General 0473
- Agronomy 0285
- Animal Culture and Nutrition 0475
- Animal Pathology 0476
- Food Science and Technology 0359
- Forestry and Wildlife 0478
- Plant Culture 0479
- Plant Pathology 0480
- Plant Physiology 0817
- Range Management 0777
- Wood Technology 0746

Biology
- General 0306
- Anatomy 0287
- Biostatistics 0308
- Botany 0309
- Cell 0379
- Ecology 0329
- Entomology 0353
- Genetics 0369
- Limnology 0793
- Microbiology 0410
- Molecular 0307
- Neuroscience 0317
- Oceanography 0416
- Physiology 0433
- Radiation 0821
- Veterinary Science 0778
- Zoology 0472

Biophysics
- General 0786
- Medical 0760

### EARTH SCIENCES
Biogeochemistry 0425
Geochemistry 0996
Geodesy 0370
Geology 0372
Geophysics 0373
Hydrology 0388
Mineralogy 0411
Paleobotany 0345
Paleoecology 0426
Paleontology 0418
Paleozoology 0985
Palynology 0427
Physical Geography 0368
Physical Oceanography 0415

### HEALTH AND ENVIRONMENTAL SCIENCES
Environmental Sciences 0768
Health Sciences
- General 0566
- Audiology 0300
- Chemotherapy 0992
- Dentistry 0567
- Education 0350
- Hospital Management 0769
- Human Development 0758
- Immunology 0982
- Medicine and Surgery 0564
- Mental Health 0347
- Nursing 0569
- Nutrition 0570
- Obstetrics and Gynecology 0380
- Occupational Health and Therapy 0354
- Ophthalmology 0381
- Pathology 0571
- Pharmacology 0419
- Pharmacy 0572
- Physical Therapy 0382
- Public Health 0573
- Radiology 0574
- Recreation 0575
- Speech Pathology 0460
- Toxicology 0383

Home Economics 0386

### PHYSICAL SCIENCES

**Pure Sciences**

Chemistry
- General 0485
- Agricultural 0749
- Analytical 0486
- Biochemistry 0487
- Inorganic 0488
- Nuclear 0738
- Organic 0490
- Pharmaceutical 0491
- Physical 0494
- Polymer 0495
- Radiation 0754

Mathematics 0405
Physics
- General 0605
- Acoustics 0986
- Astronomy and Astrophysics 0606
- Atmospheric Science 0608
- Atomic 0748
- Electronics and Electricity 0607
- Elementary Particles and High Energy 0798
- Fluid and Plasma 0759
- Molecular 0609
- Nuclear 0610
- Optics 0752
- Radiation 0756
- Solid State 0611

Statistics 0463

**Applied Sciences**

Applied Mechanics 0346
Computer Science 0984
Engineering
- General 0537
- Aerospace 0538
- Agricultural 0539
- Automotive 0540
- Biomedical 0541
- Chemical 0542
- Civil 0543
- Electronics and Electrical 0544
- Heat and Thermodynamics 0348
- Hydraulic 0545
- Industrial 0546
- Marine 0547
- Materials Science 0794
- Mechanical 0548
- Metallurgy 0743
- Mining 0551
- Nuclear 0552
- Packaging 0549
- Petroleum 0765
- Sanitary and Municipal 0554
- System Science 0790

Geotechnology 0428
Operations Research 0796
Plastics Technology 0795
Textile Technology 0994

### PSYCHOLOGY
General 0621
Behavioral 0384
Clinical 0622
Developmental 0620
Experimental 0623
Industrial 0624
Personality 0625
Physiological 0989
Psychobiology 0349
Psychometrics 0632
Social 0451

Nom ______________________________

*Dissertation Abstracts International* est organisé en catégories de sujets. Veuillez s.v.p. choisir le sujet qui décrit le mieux votre thèse et inscrivez le code numérique approprié dans l'espace réservé ci-dessous.

______________________________ ☐☐☐☐ U·M·I

SUJET — CODE DE SUJET

## Catégories par sujets

# HUMANITÉS ET SCIENCES SOCIALES

### COMMUNICATIONS ET LES ARTS
Architecture 0729
Beaux-arts 0357
Bibliothéconomie 0399
Cinéma 0900
Communication verbale 0459
Communications 0708
Danse 0378
Histoire de l'art 0377
Journalisme 0391
Musique 0413
Sciences de l'information 0723
Théâtre 0465

### ÉDUCATION
Généralités 515
Administration 0514
Art 0273
Collèges communautaires 0275
Commerce 0688
Économie domestique 0278
Éducation permanente 0516
Éducation préscolaire 0518
Éducation sanitaire 0680
Enseignement agricole 0517
Enseignement bilingue et multiculturel 0282
Enseignement industriel 0521
Enseignement primaire. 0524
Enseignement professionnel 0747
Enseignement religieux 0527
Enseignement secondaire 0533
Enseignement spécial 0529
Enseignement supérieur 0745
Évaluation 0288
Finances 0277
Formation des enseignants 0530
Histoire de l'éducation 0520
Langues et littérature 0279
Lecture 0535
Mathématiques 0280
Musique 0522
Orientation et consultation 0519
Philosophie de l'éducation 0998
Physique 0523
Programmes d'études et enseignement 0727
Psychologie 0525
Sciences 0714
Sciences sociales 0534
Sociologie de l'éducation 0340
Technologie 0710

### LANGUE, LITTÉRATURE ET LINGUISTIQUE
Langues
- Généralités 0679
- Anciennes 0289
- Linguistique 0290
- Modernes 0291

Littérature
- Généralités 0401
- Anciennes 0294
- Comparée 0295
- Mediévale 0297
- Moderne 0298
- Africaine 0316
- Américaine 0591
- Anglaise 0593
- Asiatique 0305
- Canadienne (Anglaise) 0352
- Canadienne (Française) 0355
- Germanique 0311
- Latino-américaine 0312
- Moyen-orientale 0315
- Romane 0313
- Slave et est-européenne 0314

### PHILOSOPHIE, RELIGION ET THÉOLOGIE
Philosophie 0422
Religion
- Généralités 0318
- Clergé 0319
- Études bibliques 0321
- Histoire des religions 0320
- Philosophie de la religion 0322

Théologie 0469

### SCIENCES SOCIALES
Anthropologie
- Archéologie 0324
- Culturelle 0326
- Physique 0327

Droit 0398
Économie
- Généralités 0501
- Commerce-Affaires 0505
- Économie agricole 0503
- Économie du travail 0510
- Finances 0508
- Histoire 0509
- Théorie 0511

Études américaines 0323
Études canadiennes 0385
Études féministes 0453
Folklore 0358
Géographie 0366
Gérontologie 0351
Gestion des affaires
- Généralités 0310
- Administration 0454
- Banques 0770
- Comptabilité 0272
- Marketing 0338

Histoire
- Histoire générale 0578
- Ancienne 0579
- Médiévale 0581
- Moderne 0582
- Histoire des noirs 0328
- Africaine 0331
- Canadienne 0334
- États-Unis 0337
- Européenne 0335
- Moyen-orientale 0333
- Latino-américaine 0336
- Asie, Australie et Océanie 0332

Histoire des sciences 0585
Loisirs 0814
Planification urbaine et régionale 0999
Science politique
- Généralités 0615
- Administration publique 0617
- Droit et relations internationales 0616

Sociologie
- Généralités 0626
- Aide et bien-àtre social 0630
- Criminologie et établissements pénitentiaires 0627
- Démographie 0938
- Études de l' individu et de la famille 0628
- Études des relations interethniques et des relations raciales 0631
- Structure et développement social 0700
- Théorie et méthodes 0344
- Travail et relations industrielles 0629

Transports 0709
Travail social 0452

# SCIENCES ET INGÉNIERIE

### SCIENCES BIOLOGIQUES
Agriculture
- Généralités 0473
- Agronomie. 0285
- Alimentation et technologie alimentaire 0359
- Culture 0479
- Élevage et alimentation 0475
- Exploitation des péturages 0777
- Pathologie animale 0476
- Pathologie végétale 0480
- Physiologie végétale 0817
- Sylviculture et faune 0478
- Technologie du bois 0746

Biologie
- Généralités 0306
- Anatomie 0287
- Biologie (Statistiques) 0308
- Biologie moléculaire 0307
- Botanique 0309
- Cellule 0379
- Écologie 0329
- Entomologie 0353
- Génétique 0369
- Limnologie 0793
- Microbiologie 0410
- Neurologie 0317
- Océanographie 0416
- Physiologie 0433
- Radiation 0821
- Science vétérinaire 0778
- Zoologie 0472

Biophysique
- Généralités 0786
- Medicale 0760

### SCIENCES DE LA TERRE
Biogéochimie 0425
Géochimie 0996
Géodésie 0370
Géographie physique 0368
Géologie 0372
Géophysique 0373
Hydrologie 0388
Minéralogie 0411
Océanographie physique 0415
Paléobotanique 0345
Paléoécologie 0426
Paléontologie 0418
Paléozoologie 0985
Palynologie 0427

### SCIENCES DE LA SANTÉ ET DE L'ENVIRONNEMENT
Économie domestique 0386
Sciences de l'environnement 0768
Sciences de la santé
- Généralités 0566
- Administration des hipitaux 0769
- Alimentation et nutrition 0570
- Audiologie 0300
- Chimiothérapie 0992
- Dentisterie 0567
- Développement humain 0758
- Enseignement 0350
- Immunologie 0982
- Loisirs 0575
- Médecine du travail et thérapie 0354
- Médecine et chirurgie 0564
- Obstétrique et gynécologie 0380
- Ophtalmologie 0381
- Orthophonie 0460
- Pathologie 0571
- Pharmacie 0572
- Pharmacologie 0419
- Physiothérapie 0382
- Radiologie 0574
- Santé mentale 0347
- Santé publique 0573
- Soins infirmiers 0569
- Toxicologie 0383

### SCIENCES PHYSIQUES
#### Sciences Pures
Chimie
- Genéralités 0485
- Biochimie 487
- Chimie agricole 0749
- Chimie analytique 0486
- Chimie minérale 0488
- Chimie nucléaire 0738
- Chimie organique 0490
- Chimie pharmaceutique 0491
- Physique 0494
- PolymÇres 0495
- Radiation 0754

Mathématiques 0405
Physique
- Genéralités 0605
- Acoustique 0986
- Astronomie et astrophysique 0606
- Electronique et électricité 0607
- Fluides et plasma 0759
- Météorologie 0608
- Optique 0752
- Particules (Physique nucléaire) 0798
- Physique atomique 0748
- Physique de l'état solide 0611
- Physique moléculaire 0609
- Physique nucléaire 0610
- Radiation 0756

Statistiques 0463

#### Sciences Appliqués Et Technologie
Informatique 0984
Ingénierie
- Généralités 0537
- Agricole 0539
- Automobile 0540
- Biomédicale 0541
- Chaleur et ther modynamique 0348
- Conditionnement (Emballage) 0549
- Génie aérospatial 0538
- Génie chimique 0542
- Génie civil 0543
- Génie électronique et électrique 0544
- Génie industriel 0546
- Génie mécanique 0548
- Génie nucléaire 0552
- Ingénierie des systämes 0790
- Mécanique navale 0547
- Métallurgie 0743
- Science des matériaux 0794
- Technique du pétrole 0765
- Technique minière 0551
- Techniques sanitaires et municipales 0554
- Technologie hydraulique 0545

Mécanique appliquée 0346
Géotechnologie 0428
Matières plastiques (Technologie) 0795
Recherche opérationnelle 0796
Textiles et tissus (Technologie) 0794

### PSYCHOLOGIE
Généralités 0621
Personnalité 0625
Psychobiologie 0349
Psychologie clinique 0622
Psychologie du comportement 0384
Psychologie du développement 0620
Psychologie expérimentale 0623
Psychologie industrielle 0624
Psychologie physiologique 0989
Psychologie sociale 0451
Psychométrie 0632

**THE UNIVERSITY OF CALGARY**

**FACULTY OF GRADUATE STUDIES**

The undersigned certify that they have read, and recommend to the Faculty of Graduate Studies for acceptance, a thesis entitled, "AURORA-ASSOCIATED THREE-DIMENSIONAL CURRENT SYSTEM" submitted by Fengying Zhang in partial fulfilment of the requirements for the degree of Master of Science.

L L Cogger

Supervisor, Dr. L. L. Cogger
Department of Physics and Astronomy

Dr. J. S. Murphree
Department of Physics and Astronomy

V I Birss

Dr. V. I. Birss
Department of Chemistry

Date Aug 31/93

## ABSTRACT

In this thesis ground-based measurements from the CANOPUS All-sky Imager (ASI), the Bistatic Auroral Radar System (BARS) and the Magnetometer And Riometer Array (MARIA) are combined to infer a three-dimensional current system of finite width and length in the auroral zone using a new method of quantitative analysis. In this new method, the auroral emission rates I(427.8nm) and I(630.0nm) were used to calculate the Pedersen and Hall height-integrated conductivities in the auroral arc region. Electric fields were measured from the BARS. Ohm's law and the current continuity equation were used to derive the current system. The resulting current system consisted of 400 ionospheric (horizontal) current vectors and 400 field-aligned current vectors in the field of view. The three cases selected were near midnight. The current system found is a combination of two types of Boström current systems within a small region. The magnetic perturbations on the ground resulting from the current system were calculated and compared with the magnetic observations from MARIA. The good agreement shows that the inferred current system is reasonable, and the major current source producing the magnetic perturbations on the ground is the current system in the auroral region overhead.

## ACKNOWLEDGEMENTS

I wish to express my gratitude to my supervisor, L. L. Cogger, for his kindness, guidance, encouragement and patience that were given to me throughout the course of the study.

I am greatly indebted to Dr. A. Brekke for his brilliant ideas and deep guidance in conceptualization of the study.

I would like to thank Dr. J. S. Murphree, Dr. A. Louro and Mr. R. Elphinstone for their helpful suggestions and valuable discussions in the data analysis. I like to thank Mr. G. Enno and Mr. C. Marcellus for the assistance in the use of computers and Mr. R. Condon in the use of word processors. Thanks are also given to Mr. Qi Pao for his help in the calibration of ASI data and the data analysis.

I acknowledge the Canadian Space Agency and the National Research Council of Canada for supplying the CANOPUS facilities and experimental data (ASI, BARS, and MARIA) and the financial assistance given to me by the University of Calgary during the period of my Master program. I also acknowledge the Natural Sciences and Engineering Research Council through Operating Grants and the Canadian Network for Space Research for the summer support.

Finally, I like to thank my husband for his support and encouragement throughout my study.

## TABLE OF CONTENTS

## LIST OF TABLES

## LIST OF FIGURES

## LIST OF SYMBOLS

| SYMBOLS | MEANINGS |
|---|---|
| **A** | matrix containing the magnetic field values due to the "source" cells in the Forward method |
| b | external portion of the observed magnetic field in KRM method |
| **B** | magnetic field matrix in the Forward method |
| $\vec{B}$ | vertical magnetic field in the ionosphere |
| $\Delta\vec{B}_{mn}$ | magnetic perturbation produced by the mnth ionospheric current vector |
| $\Delta B'_{mn}$ , $\Delta B''_{mn}$ and $\Delta B'''_{mn}$ | x, y and z components of $\Delta\vec{B}_{mn}$ , respectively |
| $\Delta B'_{I}$ , $\Delta B''_{I}$ and $\Delta B'''_{I}$ | x, y and z components of the total perturbation produced by all the ionospheric current vectors on the BARS map, respectively |
| $(\Delta\vec{B}_{mn})_{\parallel}$ | perturbation on the ground produced by the field-aligned current vector at the mnth pixel |
| $(\Delta B'_{mn})_{\parallel}$ and $(\Delta B''_{mn})_{\parallel}$ | x and y components of $(\Delta\vec{B}_{mn})_{\parallel}$ , respectively |
| $\Delta\vec{B}_{\parallel}$ | total perturbation produced by all field-aligned current vectors |

| | |
|---|---|
| $\Delta B_{\parallel}'$ and $\Delta B_{\parallel}''$ | x and y components of $\Delta \vec{B}_{\parallel}$, respectively |
| $E_M$ | average energy of precipitating electrons |
| E | the magnitude of the electric field in the magnetosphere |
| $E_0$ | characteristic energy of precipitating electrons |
| $\vec{E}_{\perp}$ | horizontal electric field in the ionosphere |
| $E_{\perp}'$ and $E_{\perp}''$ | x and y components of $\vec{E}_{\perp}$, respectively |
| g | correction factor for the effects of the field-aligned currents, the latitudinal width of the current sheet and the relative location of the magnetic observation with respect to the electrojet centre in " equivalent " overhead current vectors |
| H, D and Z | northward, eastward and downward components of magnetic field in local magnetic coordinate system |
| $\vec{I}_T$ | toroidal horizontal sheet current in KRM method |
| $\vec{I}_{\varphi}$ | "potential" current in KRM method |
| I(427.8nm) | auroral intensity at wavelength of 427.8nm |
| $j_{\parallel}$ and $J_{\parallel}$ | field-aligned current density |
| $(j_{mn})_{\parallel}$ | field-aligned current density at the mnth pixel |
| $\vec{J}_{\perp}$, $\vec{J}$ and $\vec{I}$ | horizontal ionospheric current intensity |
| $J_{\perp}'$ and $J_{\perp}''$ | x and y components of $\vec{J}_{\perp}$, respectively |

| | |
|---|---|
| $\Delta J_{\perp}^{\prime}$ and $\Delta J_{\perp}^{\prime\prime}$ | changes of $J_{\perp}^{\prime}$ and $J_{\perp}^{\prime\prime}$ along the x and y axes for the neighbouring two pixels, respectively |
| $\vec{J}_{mn}$ | ionospheric current vector at mnth pixel |
| $J_{mn}^{\prime}$ and $J_{mn}^{\prime\prime}$ | x, y components of $\vec{J}_{mn}$ , respectively |
| k | correction factor for the induced current effect in " equivalent " overhead current vectors |
| $k_p$ | 3 hour global index of magnetic activity |
| $\vec{n}_r$ | unit radial vector |
| **P** | current intensity matrix in the forward method |
| $\vec{r}_{mn}^{\prime}$ | vector from the mnth current source to the origin |
| $\vec{v}_e$ | electron drift velocity |
| $v_r$ | radial doppler velocity |
| V | wind velocity for a dynamo in the magnetosphere in Bostrom type 2 current system |
| $\alpha$ | coefficient including effects of the induced currents in the earth, the field-aligned currents, the latitudinal width of the current sheet and the relative location of the magnetic observatory with respect to the electrojet centre in " equivalent " overhead current vectors |
| $\psi$ | equivalent current function in KRM method |
| $\Phi$ | electrostatic potential |

| | |
|---|---|
| $\Phi_E$ | energy flux of precipitating electrons |
| $\theta$ | colatitude in spherical coordinates |
| $\lambda$ | east longitude in spherical coordinates |
| $\sigma_P$ | height dependent ionospheric Pedersen conductivity |
| $\sigma_H$ | height dependent ionospheric Hall conductivity |
| $\Sigma_P$ | height-integrated Pedersen conductivity |
| $\Sigma_H$ | height-integrated Hall conductivity |

# INTRODUCTION

Problem Identification:

In order to obtain the three-dimensional current system in the ionosphere, simultaneous observations of ionospheric electric field, the E region conductivities and the E region wind profile are needed. However, to obtain all the information needed is hardly possible. One can only try to construct a current system that is close to the real one.

In the past there have been many different instruments used to study the real three-dimensional current system (ionospheric current and field-aligned current system) in the auroral zone, such as ground-based magnetometer networks, coherent and incoherent auroral radars, balloon, rockets and satellites. (e.g. Kisabeth and Rostoker 1971, 1973; Kamide and Akasofu, 1975; Rostoker and Hughes, 1979). There have also been many different models developed to estimate the intensity or density of the ionospheric current in the system, such as line current approximations and sheet current approximations (Baumjohann et al., 1980; Brekke et al., 1974; Chapman and Bartels, 1940; Nagata and Fukushima, 1971). Since magnetic variations can be easily recorded on the ground, ground-based magnetometers have been the primary instruments used to study the three-dimensional current system until the last decade. However, using a single instrument has limitations. As well, the recent studies by combining ground-based magnetometers with another instrument (e.g. an incoherent radar) also indicate some problems due to the limitations of the models developed and the shortage of the information supplied from the instruments( e.g. Baumjohann et al., 1980, 1981; Brekke et al., 1974).

Magnetic variations measured by ground-based magnetometers, generally speaking, are influenced by many current sources in the ionosphere and magnetosphere and even in the interior of the earth. The study based on ground magnetic measurements becomes more complicated and more difficult. So, in principle it is impossible to determine uniquely the distribution of the ionospheric current density and field-aligned current density from magnetic observations made at the earth's surface alone. Brekke et al. (1974) overcame this problem by combining data from the incoherent scatter radar located at Chatanika, Alaska with data from a magnetometer located at College, Alaska. But in their study, they used a sheet current approximation which assumes an infinite current sheet flowing in the ionosphere without field-aligned currents. Their currents were also derived at only one point from the radar data. The field of view for the radar was also different from that for the magnetometer. This difference may give rise to a different time variation between the observation of the radar and the magnetometer. Another group, Baumjohann et al.(1980), combined electric fields measured by the Scandinavian Twin Auroral Radar Experiment (STARE) with magnetic perturbations simultaneously measured by the Scandinavian Magnetometer Array (SMA). In their study their current vectors were " equivalent " overhead ionospheric current vectors deduced from observed magnetometer data, which is also equivalent to the sheet current approximation. Conventionally, the sheet current approximation has been used to represent the observed ground magnetic perturbations. Therefore, they could only qualitatively analyze their three-dimensional current system when comparing the "equivalent" overhead ionospheric current vectors with simultaneously measured electric field vectors. In addition, it is generally accepted that polar geomagnetic perturbations are related to auroral activity, and are caused by current systems in the auroral region, but no one has examined directly how much perturbation on the ground is produced by the ionospheric current ( and field-aligned current ) in the auroral region.

Significance of the Study:

This study is the first attempt to combine ground-based measurements from the CANOPUS All-sky Imager (ASI), Bistatic Auroral Radar System (BARS) and the Magnetometer And Riometer Array (MARIA) to infer a three-dimensional current system with a finite width and length in the auroral zone. It has established a new method of quantitative study on the subject. The CANOPUS means the Canadian Auroral Network for the OPEN Program Unified Study.

In the new method, Ohm's law and the current continuity condition are used to derive the current system. Based on ASI auroral emission rates I(630.0nm) and I(427.8nm), height-integrated Pedersen and Hall conductivity for each pixel in the auroral arc of the BARS field of view can be estimated from the electron energy distribution. A background conductivity must be assumed. The corresponding electric field vectors in the same field can be measured by the BARS. The resulting current system consists of 400 ionospheric (horizontal) current vectors and 400 field-aligned current vectors in the field of view. In order to check the current system, the magnetic perturbation calculated from the computed current system can be compared with the magnetic observations from the MARIA.

Outline of the Study:

Seven chapters are included in this thesis. Chapter I contains a review of the relevant theory and experimental background including the importance of field-aligned currents, the relationship between field-aligned currents and ionospheric currents, Boström type 1 and type 2 theoretical three-dimensional current systems, and the "Matreshka" model, then more specifically the two advanced modelling codes developed by Kisabeth et al (1979) and Kamide et al.(1981), respectively. Chapter II briefly describes the instruments - All-sky Imager(ASI), Bistatic Auroral Radar System(BARS) and Magnetometer And Riometer Array(MARIA) - which were used to collect the data. In Chapter III a new method to investigate the three-dimensional current system in the auroral zone by combining three ground-based instruments ( ASI, BARS and MARIA) is introduced. The criteria of data selection and the procedure of data processing are given in Chapter IV. Chapter IV also contains the computed three-dimensional current system in the BARS field of view of the auroral region and the comparison of the computed magnetic perturbations with the observation of MARIA for three selected cases. Chapter V summarizes the whole thesis, discusses the results and recommends further work to be undertaken.

# CHAPTER I. BACKGROUND

## 1.1 Introduction

Birkeland (1908) first constructed a three-dimensional current system after he predicted that there might be field-aligned currents, the existence of which was confirmed later by Zmuda et al. (1974). Since then many theoretical and experimental studies have been undertaken to infer the real three-dimensional current system including the field-aligned currents, the relationship between ionospheric currents and field-aligned currents, especially the determination of the spatial distributions of ionospheric currents and field-aligned currents, and so on.

Boström (1964) constructed the Boström type 1 and type 2 three-dimensional current systems which have been very popular. Other theoretical models have been constructed by Atkinson (1967), Fukushima (1971), Vondrak (1975), Zmuda and Armstrong (1974), and Yusuhara et al. (1975). Progress at inferring the three-dimensional current system has been mainly based on ground-based magnetic observations (Baumjohann, 1980; Hughes and Rostoker, 1979; Kamide et al.,1981; Kamide et al., 1982a; Kisabeth, 1979; and others). The most commonly used models to infer the intensity of the ionospheric electric current or current density are a line current approximation and a sheet current approximation. The line current approximation was first used by Birkeland (1913) in estimating the height where the auroral electrojet flows. The sheet current approximation is the overhead current with infinitely large width and length that conventionally has been used to represent the observed ground magnetic perturbations (Baumjohann et al., 1980; Brekke et al., 1974; Chapman and Bartels, 1940; Nagata and Fukushima, 1971). The sheet current approximation with a finite latitudinal width has also been used (Walker, 1964; Scrase, 1967; Czechowsky, 1971). The " equivalent " overhead ionospheric current intensity came from the sheet current approximation. Two advanced computer simulation codes were developed by Kisabeth et al. (1979) and Kamide et al. (1981) for estimating three-dimensional current systems based on ground magnetometer data. Three-dimensional current systems for both steady and active magnetic periods have been simulated or modeled. Other methods to estimate ionospheric currents have been developed (Oldenburg, 1978; Kamide et al., 1982b).

There have been many North-South chains of densely spaced magnetometers installed in the auroral zone. Such meridian chains were installed in Alaska (Akasofu et al., 1971), Canada (Kisabeth and Rostoker, 1971), Greenland (Wilhjelm and Friis-Christensen, 1976), north-eastern Scandinavia (Maurer and Theile, 1978), and along two geomagnetic meridians in the northern part of the Soviet Union (Loginov et al., 1978). The results from the Canadian chain have been important in revealing the spatial and temporal behaviour of auroral electrojets (Kisabeth and Rostoker, 1971; Kisabeth and Rostoker, 1974; Rostoker and Hron, 1975; Hughes and Rostoker, 1977). Data from the Alaska chain were used to investigate the relationship between auroral electrojets and field-aligned currents (Yasuhara et al., 1975; Kamide et al., 1976; Kamide and Rostoker, 1977). During the 1980's the Canadian Auroral Network for the OPEN Program Unified Study (CANOPUS) network was set up in Northern Canada (for a general description of CANOPUS, see Vallance Jones et al., 1986). This network includes the All-Sky Imager (ASI), the Bistatic Auroral Radar System (BARS), the Meridian Photometer Array (MPA) and the Magnetometer And Riometer Array (MARIA).

In this chapter I will state the importance of field-aligned current, the relationship of field-aligned current and ionospheric current, and introduce a few very important theoretical and empirical models of three-dimensional current systems. Finally I will also describe the concept of " equivalent " overhead ionospheric current and the two major modelling methods - the " Forward " method developed by Kisabeth et al. (1979) and the KRM method by Kamide et al. (1981).

## 1.2 Importance of Field-aligned Currents

The existence of the field-aligned currents in the auroral zone gives rise to the three-dimensional current system in that region. In fact, the field-aligned currents are the medium which connects the solar wind-magnetosphere system with the ionosphere.

Birkeland (1908) suggested that observed magnetic disturbances were caused by field-aligned currents after he discovered the polar magnetic substorm during 1902 and 1903. He first constructed a three-dimensional current system by means of a field-aligned current. This was developed further by Alfven (1939) and Boström (1964). Chapman (1918) introduced a two-dimensional current system without a field-aligned current, which had the same effects on the ground as those from a three-dimensional system. It was not clear which current system was correct until the existence of field-aligned currents was confirmed ( Zmuda et al., 1974 and others ). Exploring how field-aligned currents relate to ionospheric currents in the auroral zone can help explain how field-aligned currents connect the outer magnetosphere to the ionosphere.

The following are the findings about field-aligned currents, summarized by Kamide et al.(1976):

(1) The field-aligned currents are confined essentially to the region of the statistical auroral oval;

(2) The upward and downward field-aligned currents appear as a pair at all local times;

(3) In the evening sector the upward field-aligned current locates in the poleward part of the auroral oval and the downward field-aligned current in the equatorward part; the directions of field-aligned currents in the morning sector are reversed;

(4) Intensities of field-aligned currents are in general not equal, so that there is a net field-aligned current flowing into or away from the ionosphere depending on the local time;

(5) The closure current of field-aligned currents in the ionosphere is the N-S segment of ionospheric currents (ie, the Pedersen current).

(6) The field-aligned currents appear to be present even during periods of very low geomagnetic activity.

## 1.3 Relationship of Ionospheric and Field-aligned Currents

The height-integrated ionospheric horizontal current intensity (A/m) consisting of

Pedersen current and Hall current can be expressed by

$$\vec{J}_{\perp} = \Sigma_P \vec{E}_{\perp} + \Sigma_H \frac{\vec{E}_{\perp} \times \vec{B}}{B} \tag{1.1}$$

where $\Sigma_P$ and $\Sigma_H$ are height-integrated Pedersen and Hall conductivities, respectively, $\vec{E}$ is the horizontal electric field and $\vec{B}$ is the vertical magnetic field in the ionosphere. According to the condition for current continuity, the relationship between horizontal current in the ionosphere and field-aligned current can be written as

$$j_{\parallel} = \nabla \cdot \vec{J}_{\perp} \tag{1.2}$$

where $j_{\parallel}$ represents field-aligned current density (A/m$^2$) and $\vec{J}_{\perp}$ represents horizontal current intensity (A/m).

Figure 1.1 gives the schematic diagram of the relationship between Pedersen currents and field-aligned currents (Baumjohann, 1983), in which the arrows show the direction of Pedersen current and circles with crosses and dots denote the downward and upward field-aligned currents, respectively. The Pedersen current flows northward in the afternoon and evening sector, closing the balanced upward field-aligned current poleward and downward field-aligned current equatorward. In the postmidnight and morning sector the Pedersen current is southward and balanced field-aligned currents provide current continuity by flowing upward in the equatorward side of the oval and downward in the poleward side. The discontinuity part is more complicated and unclear yet. Figure 1.2 (Baumjohann, 1983) shows the relationship of the electrojets and field-aligned currents. Both eastward and westward electrojets are Hall currents which originate around noon time and are fed by downward 'net' field-aligned currents. Their current intensities (from 0.5 to 1 A/m) increase toward midnight due to the increasing Hall conductivity. The eastward electrojet terminates in the Harang discontinuity region. It partially flows up magnetic field lines as net field-aligned current. It also partially diverges northward in the region of westward electric fields to join the westward electrojet which typically extends into the evening sector along the poleward border of the auroral oval and diverges as upward net field-aligned current. The picture presented here seems to be almost the same as the result of Kamide et al. (1977) from substorm events. They found that in the morning sector both the upward and the downward field-aligned currents are in general confined to the region of the westward electrojet, but that in the evening sector the upward current could flow away from the ionosphere poleward of the eastward electrojet. However, Hughes et al.(1979) found that the westward electrojet penetrates up to the dusk meridian for periods of moderate activity even though substorms are not necessarily in progress.

## 1.4 Boström types of three-dimensional current system

A simplified picture of Boström type 1 three-dimensional current system is shown in Figure 1.3 (Boström, 1964). A current flows along the field lines from the outer magnetosphere to one end of the arc, continues as a jet current along the auroral arc, and returns to the outer magnetosphere where it is closed. This type of current system was suggested by Boström (1964) when he considered the magnetosphere as a driving force of the current system. As a result of computation, he showed that it was necessary to apply an electric field of 25 mV/m along the arc to drive the current in the arc. The corresponding longitudinal electric field is about 1.5 mV/m in the magnetosphere.

A Boström type 2 current system is shown in Figure 1.4 (Boström, 1964), where there must be an electric field of the strength 56 mV/m perpendicular to the arc to explain the magnetic disturbances and the motion of irregularities. The current along the arc is a Hall current, whereas the current perpendicular to the arc is a Pedersen current. The two sheets of field-aligned currents are closed by the Pedersen current perpendicular to the arc in the auroral zone. The Hall current that flows along the arc must be closed, either by currents in the ionosphere or by currents from the end points of the arc to the outer magnetosphere. There is a dynamo in the magnetosphere to drive the field-aligned currents. The electric field E in the magnetosphere and the wind velocity V for the dynamo are shown in Figure 1.4.

Timofeev et al. (1990) considered the schematics of auroral electrodynamical patterns from various selected experimental data sets. They constructed an extended Boström current loop model, called the " Matreshka " model, which is the hierarchy of three encircled two sheet Boström current loops of different sizes. The largest current loop has the scale of the region 1 or region 2 which are defined respectively as the poleward side and the equatorward side in the ionosphere (Iijima and Potemra, 1976). The intermediate one has the scale of an inverted-V (the definition is in the reference of Lin and Hoffman, 1979) of order of 100 km and the smallest one has an auroral arc scale of about 10 km. Each current loop has the same direction. The model is limited to the cases of steady conditions with homogenous auroral bands and visual arcs. Dynamic

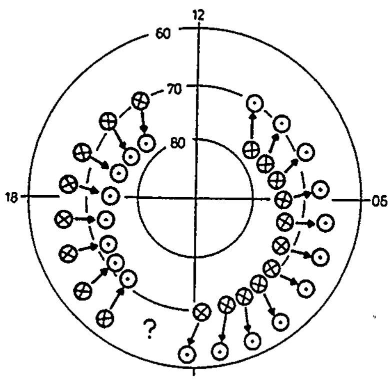


Figure 1.1 the relationship of Pedersen currents and balanced field-aligned currents in the auroral oval (in invariant latitude - magnetic local time coordinates) (Baumjohann, 1983).

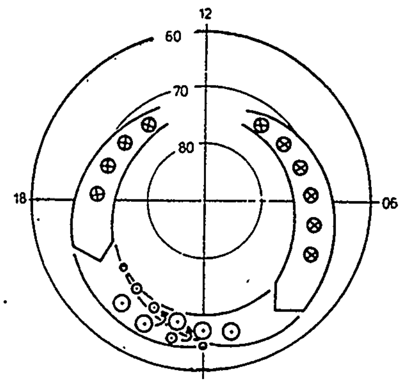


Figure 1.2 the relationship of Hall currents and field-aligned currents in the auroral oval (in invariant latitude - magnetic local time coordinates) (Baumjohann, 1983).

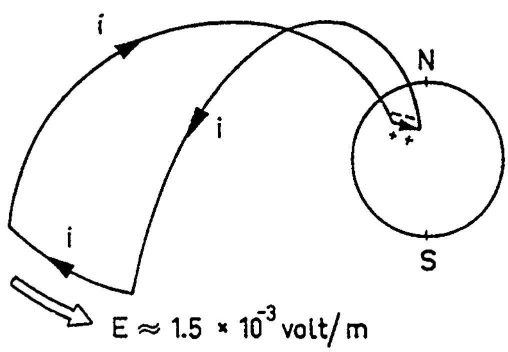


Figure 1.3 Simplified Boström type 1 current system. A current flows into the ionosphere at one end of the arc and out at the other (Boström, 1964).

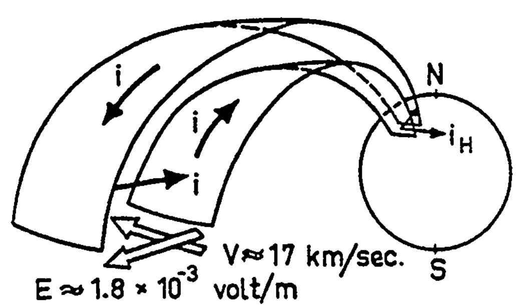


Figure 1.4 Simplified Boström type 2 current system. A current flows into the ionosphere on the equatorward side of the arc all the way along the arc and flows out of the ionosphere on the poleward side (Boström, 1964).

cases with moving and burst-like rayed arcs are not covered.

In this section several interesting theoretical models have been briefly introduced. In fact, the actual ionospheric and field-aligned current system is more complicated than any type of current system mentioned above.

## 1.5 " Equivalent " Overhead Ionospheric Currents

Relationships of ionospheric currents and components of ground magnetic variation have been suggested by many researchers (e.g. Brekke et al, 1974; Chapman and Bartels, 1940; Nagata and Fukushima, 1971; Walker, 1964). If a thin spherical electric current sheet is assumed to flow in the ionosphere, the current intensity $\vec{J}$ in magnitude is approximately proportional to the magnitude of horizontal ground magnetic variation, but rotates $90^0$ clockwise in direction. For example, the E-W ionospheric current intensity is related to the N-S component of the ground magnetic variation H, by

$$J_{EW}(A/km) = \alpha\ H(nT) = k\ g\ \frac{10}{2\pi} H(nT) \qquad (1.3)$$

where $\alpha$ is a coefficient which includes effects of the induced currents in the earth, the field-aligned currents, the latitudinal width of the current sheet and the relative location of the magnetic observation with respect to the electrojet centre. Specifically, k is the correction factor for the induced current effect and g denotes the effects for all others. H is a component in local magnetic coordinate system, where the H component is defined as positive northward. The D component is defined as positive eastward and the z component is defined as positive downward. We can choose g = 1 for the infinite equivalent ionospheric current approximation ( Chapman and Bartels, 1940). k = 1 means no induced current and k = 0.5 requires a perfectly conducting earth. When assuming k = 0.6 the equation above can be written by

$$J_{EW}(A/km) = 0.6 \times 1 \times \frac{10}{2\pi} H(nT) \approx H(nT) \qquad (1.4)$$

Brekke et al.(1974) made a systematic comparison of the current deduced from incoherent scatter radar at Chatanika and the magnetic field at College, and found that the E-W D component of the magnetic observation disagreed with the N-S current in a manner that cannot be explained, unless currents parallel to the earth's magnetic field are present. Kamide et al. (1976) showed that the disagreement can be removed by introducing field-aligned currents for which the density is different on the poleward side and equatorward side of the auroral oval. It should also be noted that a magnetometer observes an integrated magnetic field due to currents flowing in a wide range of the ionosphere (and magnetosphere as well as the interior of the earth), while from the radar data currents are derived at one point (Brekke et al., 1974). This difference in the field of view may result in a different time variation between the observation of the radar and the magnetometer. Therefore, it is necessary to average many single measurements in order to obtain an accurate relationship between an ionospheric current and the corresponding magnetic field ( Araki and Schlegel, 1989).

## 1.6 Three-dimensional Current Systems Estimated from Ground-based Magnetic Measurements

### 1.6.1 The " Forward " method

This method was developed by Kisabeth (1979). Its procedure is summarized in Figure 1.5. Ground magnetic components H, D and Z are input and ionospheric currents and field-aligned currents are output. A spherical earth with a dipole field is considered. The high latitude ionospheric region is divided into 168 cells, configured in seven current rings with equal latitude width of $3^0$ extending from $61^0$ to $82^0$ and 24 cells longitudinally for each current cell ring. Each cell is associated with two elementary three-dimensional current systems — Boström type 1 and type 2 current systems mentioned in the above sections. It is assumed that the field-aligned currents flow along dipole field lines and close in the equatorial plane. The purpose is to find a set of E-W and N-S ionospheric currents for all cells and the associated field-aligned currents which best produce the input data.

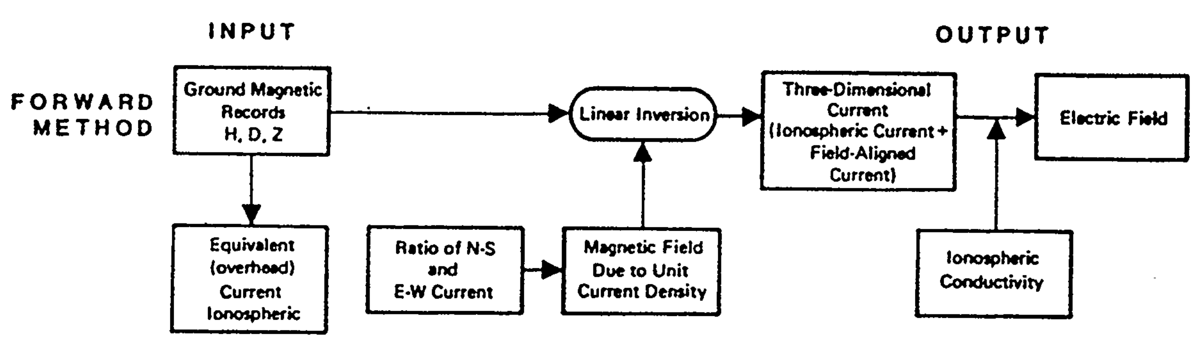


Figure 1.5 Flow chart of the " Forward " method

The key step in this method is to calculate the magnetic field at 240 observation points (10 points along each magnetic local time hour meridian) due to a chosen set of unit current intensities in each cell (the "source cell"), 1 A/m for the E-W current and -0.5 A/m for the N-S current in this case. This choice of current intensities is equivalent to utilizing a height-integrated Hall to Pedersen conductivity ratio of 2.0, in which only a N-S ionospheric electric field is present. The current intensity matrix **P** and the corresponding magnetic field matrix **B** (the input data set) are related to each other by the matrix **A** which is a complicated arrangement of the magnetic field values due to the "source" cells. The equation is

$$\boldsymbol{B} = \boldsymbol{AP} \tag{1.5}$$

In this particular situation, the **P**, **B** and **A** matrices consist of (168 $\times$ 1), (720 $\times$ 1) and (720 $\times$ 168) elements, respectively. Through a linear inversion the E-W or N-S component of the horizontal current can be determined by

$$\boldsymbol{P} = (\boldsymbol{A}^T\boldsymbol{A})^{-1}\boldsymbol{A}^T\boldsymbol{B} \tag{1.6}$$

where $\mathbf{A}^T$ is the transpose matrix of **A**. Then the upward or downward field-aligned currents can be estimated by calculating the divergence of the horizontal current at the corners of the grid cells. It is possible to derive the electric field from the ionospheric current using the given ionospheric conductivities. Figure 1.6 shows an example of the

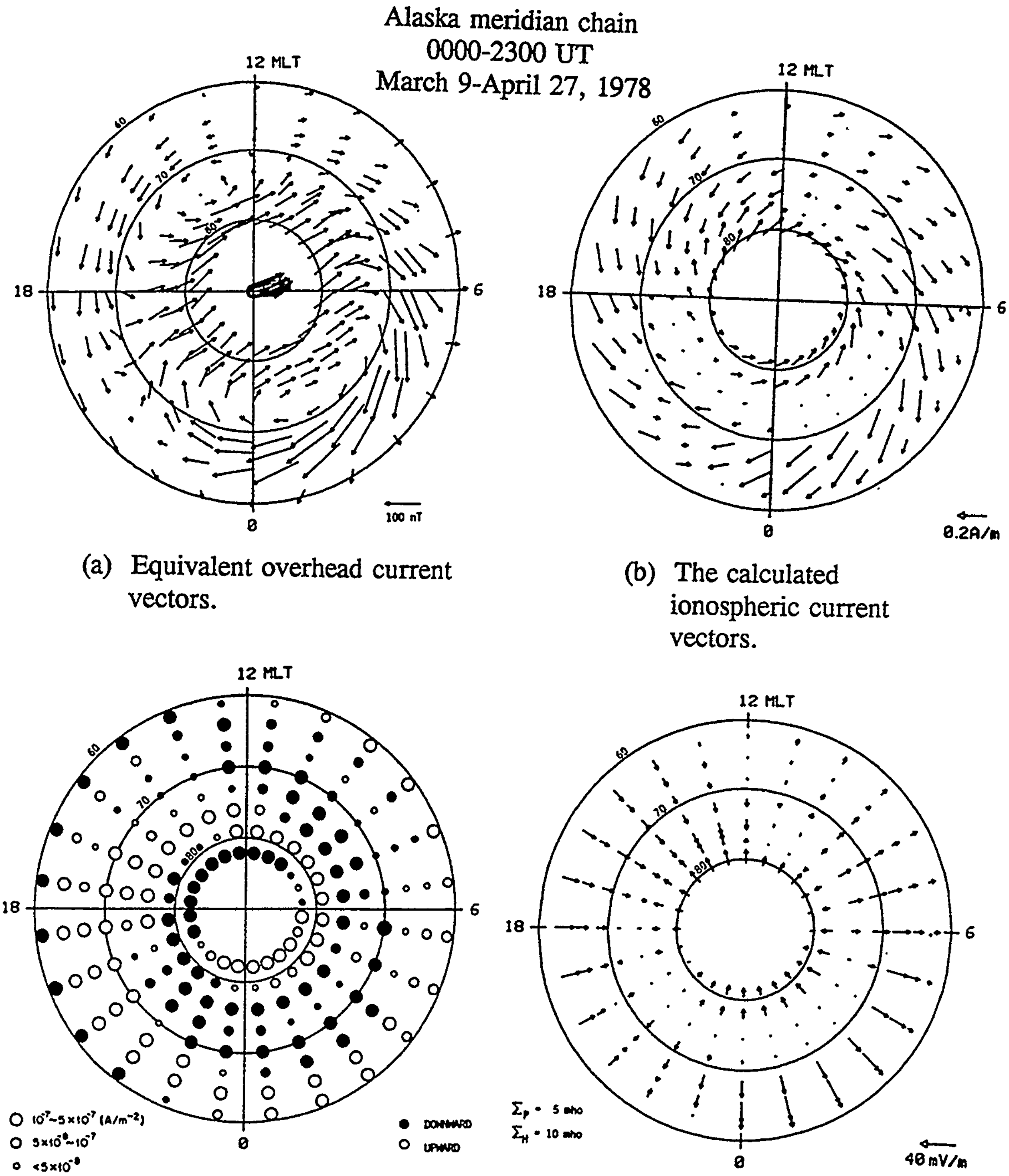


(a) Equivalent overhead current vectors.

(b) The calculated ionospheric current vectors.

(c) The estimated field-aligned currents.

(d) The estimated electric field vectors

Figure 1.6 An example of forward method (Akasofu et al., 1981) equivalent current vectors, calculated ionospheric current vectors, field-aligned currents and electric fields obtained from "Forward" method (Akasofu et al., 1981).

The assumptions considered in this method include (1) geomagnetic field lines are equipotentials; (2) the effects of ionospheric winds are ignored; (3) the effects of the magnetospheric ring current, the magnetopause current and tail current are ignored; (4) all the ionospheric currents are confined to latitudes from $61^0$ to $82^0$; (5) only the N-S component of the electric field is considered.

### 1.6.2 The KRM method

The KRM (Kamide, Richmond and Matsushita) method was developed by Kamide et al.(1981). This method is significantly different from the " Forward " method in principle. The procedure is shown in Figure 1.7. The equivalent current system in this method is defined as a toroidal horizontal sheet current $\vec{i}_T$ flowing in a shell at 110 km

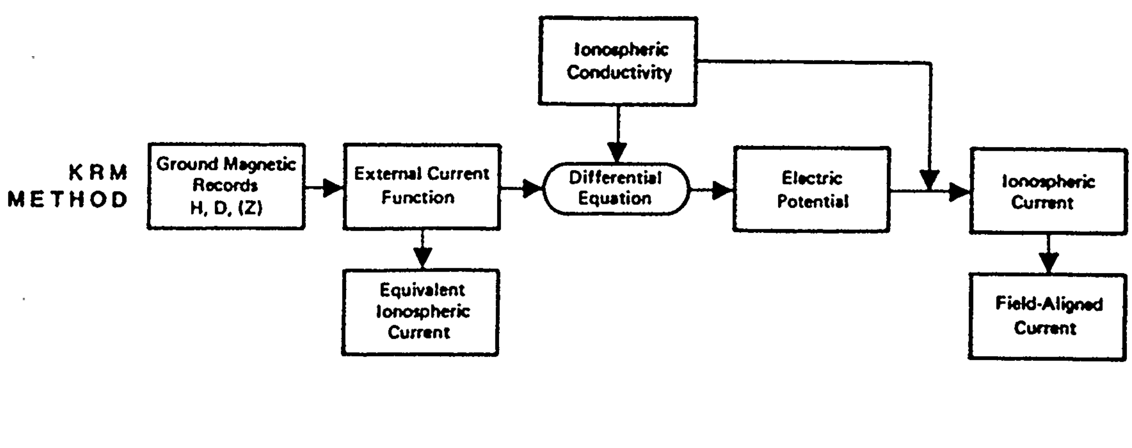


Figure 1.7 Flow chart of the KRM method

altitude, whose associated magnetic field matches the external portion of the observed magnetic variation field b. A minor portion of b is caused by electric currents induced within the earth. The toroidal current $\vec{\imath}_T$ can be expressed in terms of an equivalent current function $\psi$ as

$$\vec{\imath}_T = \vec{n}_r \times \nabla\psi \qquad (1.7)$$

where $\vec{n}_r$ is a unit radial vector. The equivalent current function has often been estimated by assuming that $\vec{\imath}_T$ is proportional to the horizontal magnetic variation in magnitude, but rotated $90^0$ clockwise in direction (e.g. Nagata and Fukushima, 1971). In addition, the height-integrated ionospheric Pedersen and Hall conductivities are required. With a given equivalent current function and conductivities, it is possible to derive ionospheric electric fields, ionospheric currents and field-aligned currents under some assumptions which we discuss later.

The total height-integrated horizontal current $\vec{\imath}$ is the sum of the toroidal (equivalent) current $\vec{\imath}_T$ and a "potential" current $\vec{\imath}_\varphi$ ,

$$\vec{\imath} = \vec{\imath}_T + \vec{\imath}_\varphi \qquad (1.8)$$

The potential component can be considered a closing current for the field-aligned current. Since $\vec{\imath}_T$ is by definition divergence free, the current continuity gives the field-aligned current density as

$$J_\parallel = \nabla\cdot\vec{\imath} = \nabla\cdot\vec{\imath}_\varphi \qquad (1.9)$$

Note that the current system represented by $J_{\parallel}$ and $\vec{I}_{\varphi}$ together produces no ground magnetic variations under the assumption of radial geomagnetic field lines, implying that the toroidal component of $\vec{I}$ is just the equivalent current.

Ohm's law relates the horizontal ionospheric current to the electric field by

$$\vec{I} = \Sigma_P \vec{E} + \Sigma_H \vec{E} \times \vec{n}_r \qquad (1.10)$$

The electric field can be written as an electrostatic potential $\Phi$ by

$$\vec{E} = -\nabla\Phi \qquad (1.11)$$

A partial differential equation for $\Phi$ in terms of $\psi$ and ionospheric conductivities $\Sigma_P$ and $\Sigma_H$ can be obtained by combining the equations (1.7), (1.8), (1.10) and (1.11), taking the curl of the resulting equation. In spherical coordinates $\theta$ (colatitude) and $\lambda$ (east longitude) the equation for $\Phi$ is

$$A\frac{\partial^2\Phi}{\partial\theta^2} + B\frac{\partial\Phi}{\partial\theta} + C\frac{\partial^2\Phi}{\partial\lambda^2} + D\frac{\partial\Phi}{\partial\lambda} = F \qquad (1.12)$$

where the coefficients are give by

$$A = \sin\theta\ \Sigma_H \qquad (1.13)$$

$$B = \frac{\partial}{\partial\theta}(\sin\theta\Sigma_H) + \frac{\partial}{\partial\lambda}\Sigma_P \tag{1.14}$$

$$C = \frac{\Sigma_H}{\sin\theta} \tag{1.15}$$

$$D = \frac{\partial}{\partial\theta}\Sigma_P - \frac{\partial}{\partial\lambda}(\frac{\Sigma_H}{\sin\theta}) \tag{1.16}$$

$$F = \frac{\partial}{\partial\theta}(\sin\theta\frac{\partial\psi}{\partial\theta}) + \frac{1}{\sin\theta}\frac{\partial^2\psi}{\partial\lambda^2} \tag{1.17}$$

In solving the equation (1.12), the following boundary conditions are adopted:

$$\phi(0,\lambda)=0 \tag{1.18}$$

$$\frac{\partial\phi}{\partial\theta}(90^0 , \lambda) = 0 \tag{1.19}$$

The equation is solved numerically by a finite difference scheme over a network of points spaced $1^0$ in colatitude and $15^0$ in longitude. Once the electrostatic potential is obtained, the electric field from Eqn.(1.11), the ionospheric current from Eqn.(1.10) and field-aligned current from Eqn.(1.9) are obtained. Figure 1.8 gives an example of the equivalent current vectors, ionospheric current vectors, field-aligned currents and electric fields derived from the KRM method (Akasofu et al., 1981).

The assumptions considered in this method include (1) the electric field is

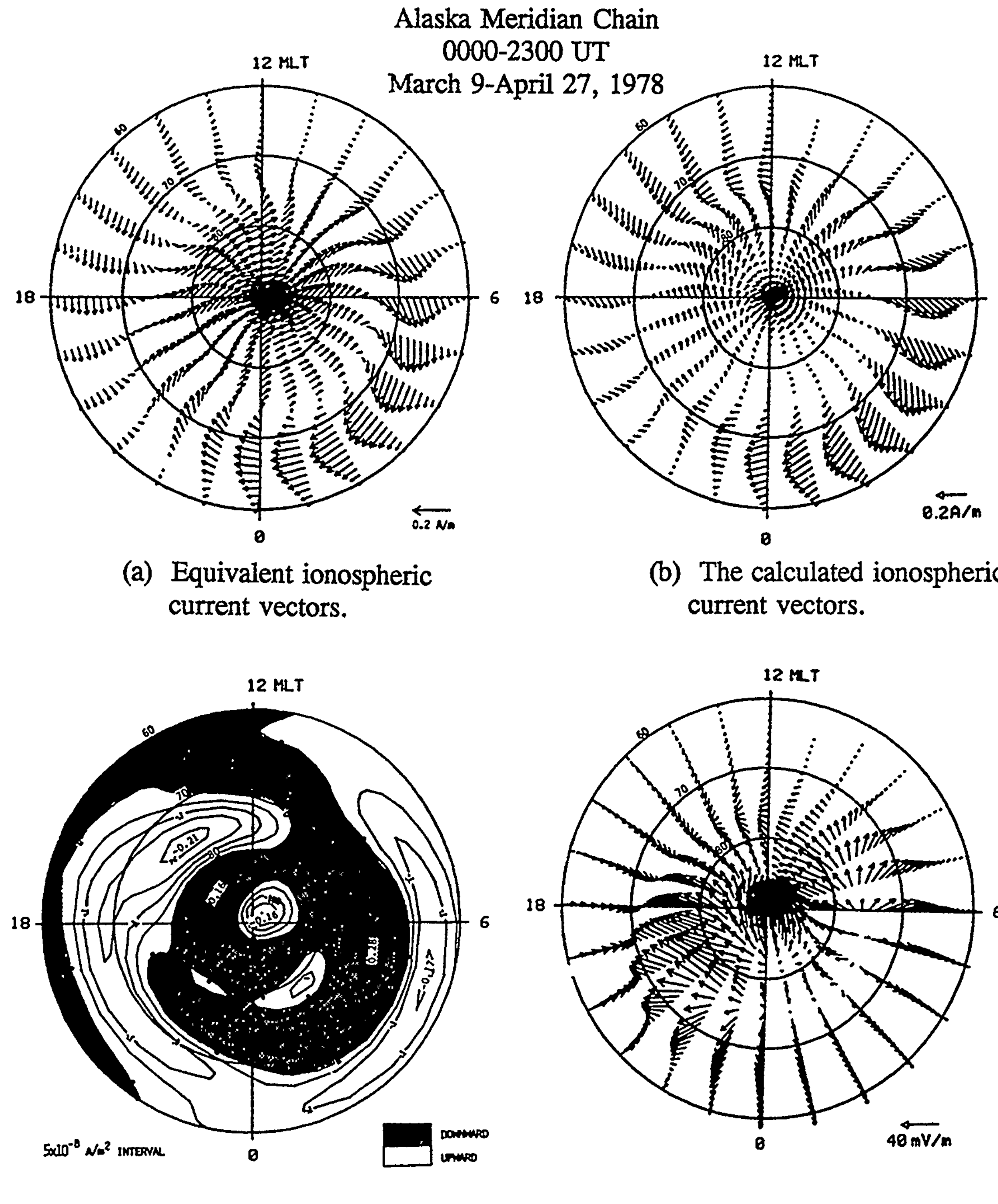


(a) Equivalent ionospheric current vectors.

(b) The calculated ionospheric current vectors.

(c) The estimated field-aligned currents.

(d) The estimated electric field vectors.

Figure 1.8 An example of KRM method (Akasofu et al., 1981) electrostatic; (2) geomagnetic field lines are equipotential; (3) the dynamo effects of ionospheric winds can be ignored; (4) the magnetic conditions of magnetospheric ring current, magnetopause currents and tail currents to the equivalent current function can be neglected; (5) geomagnetic field lines are effectively radial.

## 1.7 The Analysis Method Used in this Thesis

The analysis method used in this thesis is a first attempt to combine measurements from three kinds of ground-based instruments to infer a three-dimensional current system with a finite width and length within the field of view of the instruments in the auroral region. In this method, the auroral emission rates for the wavelengths of 427.8nm and 630.0nm observed by the ASI are used to estimate the Pedersen and Hall height-integrated conductivities in the auroral region. The conductivities in the background region outside the arc are assumed. The electric fields are measured by the BARS. Therefore, with the height-integrated Pedersen and Hall conductivities and the electric fields as inputs, the horizontal ionospheric current can be calculated by Ohm's law and the vertical field-aligned current can be obtained from the divergence of the horizontal current. The result can be verified by comparing the magnetic perturbations calculated from the current system with the magnetic observations. Brekke et al. (1974) used a similar method to construct a current system, but it was a two-dimensional infinite sheet current without field-aligned currents. They used Ohm's law and also compared the result with the magnetic observation.

# CHAPTER II. INSTRUMENTATION

## 2.1 Introduction

The Canadian Auroral Network for the OPEN Program Unified Study, so-called CANOPUS, was set up during the 1980's. It consists of an array of automatic ground-based instruments located in northern Canada, shown in Figure 2.1. The information about the location of those instruments is supplied in Table 2.1. The CANOPUS facility provides very high resolution optical auroral and electric field observations together with lower spatial resolution but high sensitivity magnetic field observation. The optical auroral images are produced by the All-sky Imager (ASI), the electric field observation can be estimated from the Bistatic Auroral Radar System (BARS) and the magnetic field perturbation can be measured by the Magnetometer And Riometer Array (MARIA). By using ASI data, we can estimate energy input and average energy of the precipitating electrons from the magnetosphere. Because those observing facilities are all coincidently located and complementary, they provide a unique data set for magnetospheric and ionospheric studies. In the following sections we will describe those three instruments briefly.

## 2.2 All-sky Imager (ASI)

The All-sky Imager is located at Gillam, Manitoba ( $56.85^0$ N, $265.58^0$ E in geographic and $63.9^0$ N, $336.06^0$ E in eccentric dipole field line (EDFL) magnetic

Table 2.1 Station Locations of the CANOPUS System

| MAP ID | Station | Geographic | | Eccentric Dipole | | Site |
|---|---|---|---|---|---|---|
| | | Lat.(N) | Long.(E) | Lat.(N) | Long.(E) | |
| PI | Pinawa | 50.20 | 263.96 | 57.80 | 335.02 | M, P |
| IL | Island Lake | 53.88 | 265.32 | 61.51 | 336.36 | M |
| GI | Gillam | 56.85 | 265.58 | 63.90 | 336.06 | M, P, I |
| BA | Back | 57.68 | 265.77 | 65.26 | 336.59 | M |
| CH | Churchill | 58.80 | 265.90 | 66.43 | 336.66 | M |
| EP | Eskimo Point | 61.10 | 265.93 | 68.74 | 336.47 | M |
| RI | Rankin Inlet | 62.80 | 267.67 | 70.47 | 338.66 | M, P |
| RA | Rabbit Lake | 58.20 | 256.33 | 65.49 | 324.46 | M |
| MC | Fort McMurray | 56.73 | 248.62 | 63.53 | 315.20 | M |
| FS | Fort Smith | 58.00 | 246.00 | 64.60 | 311.56 | M, P |
| CL | Contwoyto Lake | 65.48 | 249.65 | 72.38 | 312.97 | M |
| SI | Fort Simpson | 61.75 | 238.77 | 67.71 | 300.92 | M |
| DA | Dawson | 64.07 | 220.58 | 67.87 | 277.57 | M |
| NI | Nipawin | 53.47 | 256.23 | 60.74 | 325.28 | R |
| RL | Red Lake | 50.90 | 266.53 | 58.57 | 338.05 | R |

I = ASI, R = BARS, P = MPA, and M = MARIA.

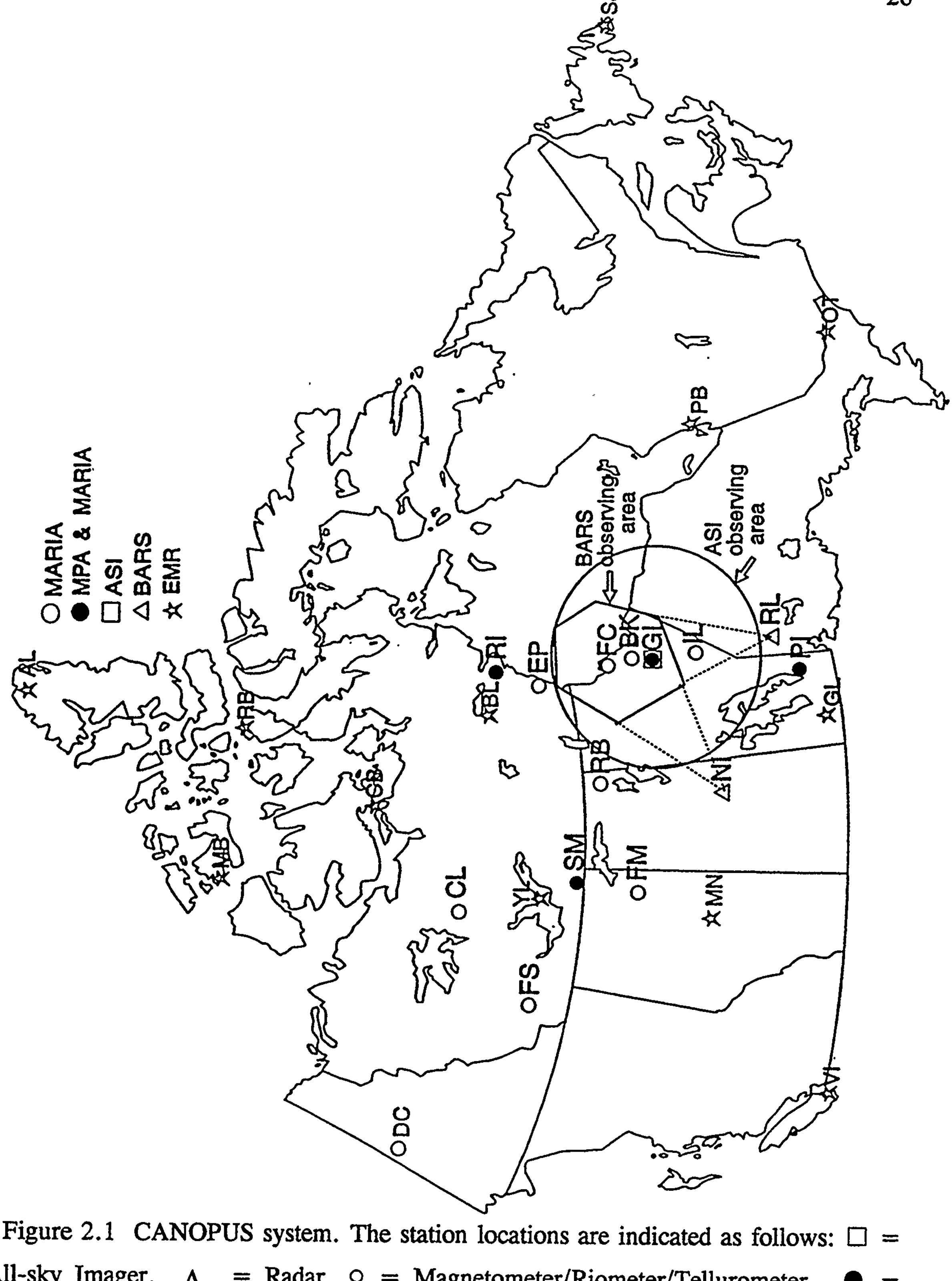


Figure 2.1 CANOPUS system. The station locations are indicated as follows: □ = All-sky Imager, Δ = Radar, ○ = Magnetometer/Riometer/Tellurometer, ● = Meridian Photometer.

coordinate system ). It consists of two main systems, the camera unit containing the optics , image intensifier and CCD ( charge-coupled device ) detector, and the control unit regulating instrument operation. The camera unit is mounted outside on a platform and contains an environmental package to control temperatures as well as keep the optics clear of snow and ice. The control unit is mounted in an electronics cabinet in the heated site structure. The ASI provides quantitative information about visual auroral emissions at wavelengths of 427.8nm ($N_2^+$), 557.7nm ($O(^1S)$), 630.0nm ($O(^1D)$) and background channel 440.0nm. It has a spatial format of 256 $\times$ 256 CCD pixels and a temporal resolution of 20 seconds. In the standard operating mode, images are obtained at 5-s intervals from each of the those wavelengths in turn, followed by a background channel exposure, giving an image at each wavelength once every 20s. In order to match the BARS field of view ( which will be described below), each CCD image has to be reduced to a 25 $\times$ 16 superpixel auroral image having spatial resolution of 20 km $\times$ 20 km. Thus the total observation area of ASI is equivalent to that of BARS (500 km $\times$ 320 km, from $63.0^0$ to $67.8^0$ in EDFL latitude and from $333^0$ to $340.5^0$ in EDFL longitude ).

A CCD detector in ASI is actually a photon-to-electron convertor, so what we obtain from ASI is the number of counts. To convert back from counts to intensities of the auroral emissions, a calibration process is needed to determine the conversion efficiency. Before the ASI was operated in 1986, a set of calibration constants of R(x) (x=1,4) for the four wavelengths were determined experimentally by means of a Low Brightness Source (LBS). A procedure to convert raw counts to intensities was used (detailed description is presented in Pao's thesis, 1991). The final result obtained was a calibrated dark count corrected and background channel subtracted intensity. After conversion, some data were compared with the Meridian Photometer Array (MPA) (Pao, 1991) and showed a very good agreement. However, after the ASI was broken at the end of 1989, the 1990's ASI data required a new set of calibration constants of R(x) which were supplied but not obtained experimentally. This set of calibration constants were suspect due to the fact that the ASI intensities using this new set of calibration constants were not only unreasonably high but also far different from the intensities measured by MPA. Since it was not realistic to obtain the calibration constants experimentally, a cross calibration was used in this thesis by means of MPA. Assuming the calibration in MPA was correct, the intensities obtained from MPA could be used to calculate ASI calibration constants of three R(x) (x=1,3) (except the background channel) which converts counts to Rayleigh units. Since MPA does not observe the emission at 427.8nm but 470.9nm , a theoretical value of a factor of I(427.8nm)/I(470.9nm) = 5 (Vallance Jones, 1974) was used for the cross calibration. Then a similar processing procedure was used except that the background channel intensity was not subtracted from each auroral channel.

## 2.3 Bistatic Auroral Radar System (BARS)

A dual pulsed Bistatic Auroral Radar System (BARS) in CANOPUS is designed for mapping ionospheric electric fields in the auroral region using the STARE techniques. The system consists of two radars, one in Nipawin (53.47$^0$ N, 256.23$^0$ E in geographic, 60.74$^0$ N, 325.28$^0$ E in EDFL ) in central Saskatchewan and the other in Red lake

($50.90^0$ N, $266.53^0$ E in geographic, $58.7^0$ N, $338.05^0$ E in EDFL ) in Northwestern Ontario. The frequency at which the system operates is 50 MHz. Antenna systems for BARS are designed to yield a 16-beam fan with a beam separation of $3.6^0$, from which 8 beams are selected for signal processing. The aspect angles from the two BARS radars range from $3.6^0$ to $5.2^0$ off-perpendicularity for Red Lake and from $4.7^0$ to $8.9^0$ for Nipawin. The field of view formed by the two radar beams shown in Figure 2.2 is a two dimensional map of 500 km $\times$ 320 km from $63.0^0$ N to $67.8^0$ N in geomagnetic latitudes, and from $333^0$ W to $340.5^0$ W in geomagnetic longitudes, with a spatial resolution of about 20 km $\times$ 20 km. The total measurement points in a BARS map is 25 $\times$ 16 = 400. The temporal resolution of BARS is 30 seconds. The radar system measures the radial doppler velocity which is the phase velocity of the plasma waves propagating along the radar k-vector. Such plasma waves are usually generated by the streaming of electrons relative to the ions in the auroral electrojet region at heights near 110 km. The measured radial doppler velocity varies as the cosine of the angle between the radar wave vector and the irregularity drift direction. The observed radial velocity is related to the electron drift by $v_r = \vec{k} \cdot \vec{v}_e$ . Two doppler measurements from different directions will give the electron drift velocity $\vec{v}_e$ . Since the electrons are $\vec{E} \times \vec{B}$ drifting at E-region heights, we obtain

$$\begin{aligned} \vec{v}_e &= \frac{\vec{E}_\perp \times \vec{B}}{B^2} \\ \vec{E}_\perp &= -\vec{v}_e \times \vec{B} \end{aligned} \tag{2.1}$$

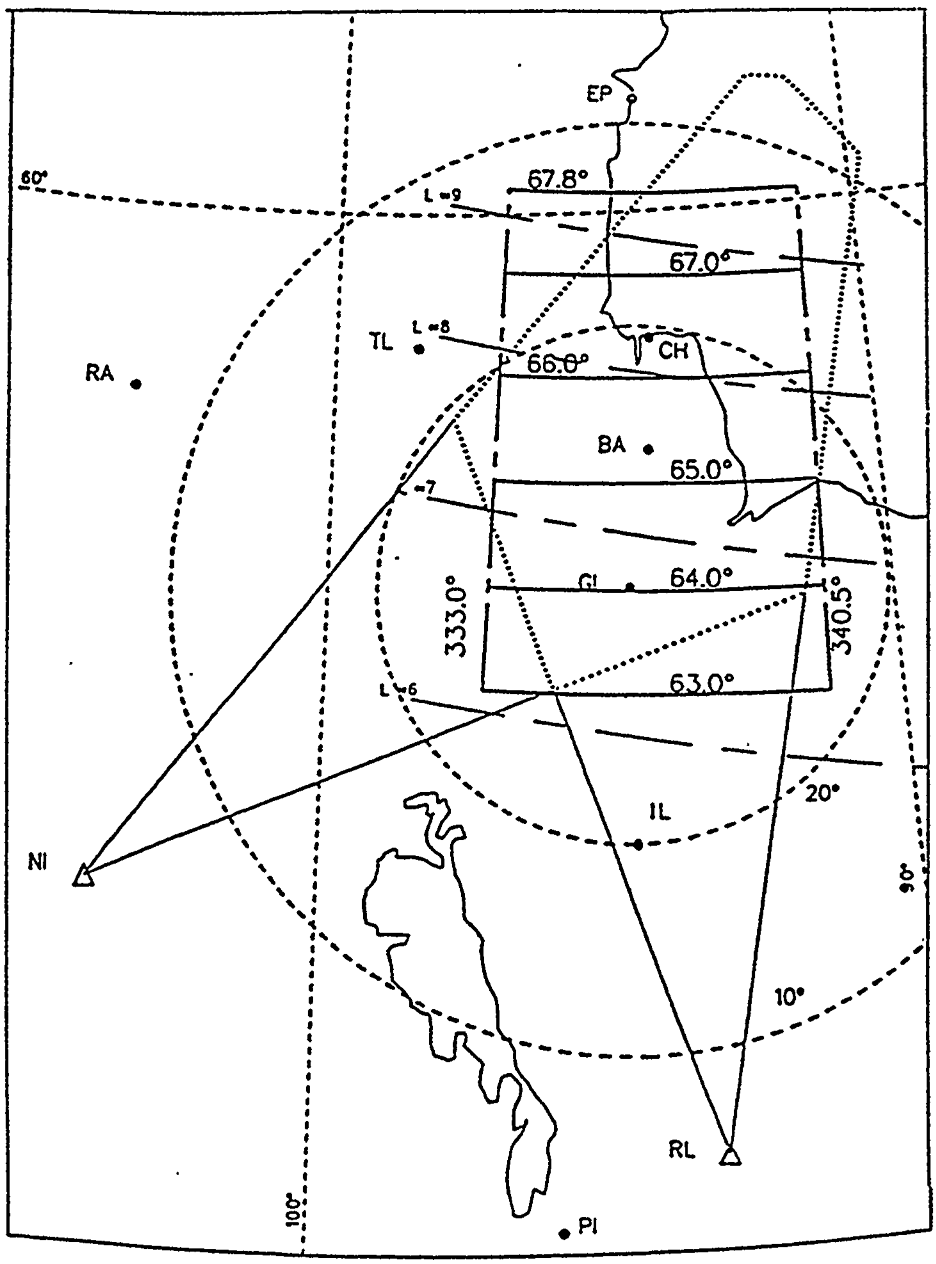


Figure 2.2 BARS viewing area and grid. The 16×25 cell grid lines within the heavy solid lines for which the EDFL magnetic coordinates are indicated. The light dashed grid shows geographic coordinates (user manual for BARS).

The observed doppler shift provides information about the ionospheric ( horizontal ) electric field. An electric field vector map consisting of 25 $\times$ 16 elements can be created at the height of 110 km and within the field of view. The system is described in detail by McNamara et al.(1983).

## 2.4 Magnetometer And Riometer Array (MARIA)

The MARIA system consists of 13 sites at each of which is installed a magnetometer, a 30 MHz zenith riometer and a 2-component earth current (telluric ) instrument, shown in Figure 2.1 and Table 2.1. The first 7 sites constitute a meridian line and the remaining 6 sites form an east-west line according to their locations. Since we are only interested in the magnetometers, the remaining instruments will not be described here. The information about them can be found in the MARIA manual (1988). Each magnetometer consists of a three-component fluxgate. The resolution of the magnetometers is 0.1 nT at 8 Hz and the range of the measurement is from 0 to 100000 nT for the vertical component and 50000 nT for the horizontal components.

# CHAPTER III. ANALYSIS METHOD

## 3.1 Introduction

The energetic plasma in the magnetosphere can precipitate into the auroral zone in the ionosphere due to the high conductivity along geomagnetic field lines and interact with the cold ionospheric plasma. Since the ionospheric plasma is far more dense than the magnetospheric plasma and is not collisionless, the ionization produced by energetic electrons impinging on the ionosphere causes enhancement of conductivity in the auroral region. In addition, the magnetospheric electric fields can be mapped into the ionosphere also due to the high conductivity along geomagnetic field lines. Electric fields normal to magnetic fields cause differential motion of ions and electrons, giving rise to the horizontal current flowing in the ionosphere. Therefore the horizontal current would produce magnetic perturbations on the ground, as would the field-aligned currents which flow along the geomagnetic field lines. If the current systems around the earth other than the aurora-associated current system discussed above are ignored, the perturbation observed on the ground is affected only by the ionospheric currents and field-aligned currents in the auroral region. Figure 3.1 shows the flow chart of electric dynamic processes associated with aurora.

This chapter introduces a new method, which will utilize data observed from ASI and BARS, to construct an ionospheric current and field-aligned current system ( three-dimensional current system ) in the auroral region. This current system can be tested by comparing the perturbation on the ground calculated from it with the magnetic observations from MARIA. This chapter consists of three parts. Section 3.2 describes how to calculate the horizontal current in the auroral region and the field-aligned current flowing into or out of the auroral region. Auroral height-integrated Pedersen and Hall conductivities can be estimated from ASI column emission rates. Ionospheric electric fields in the auroral region can be measured by BARS. Section 3.3 and 3.4 introduces

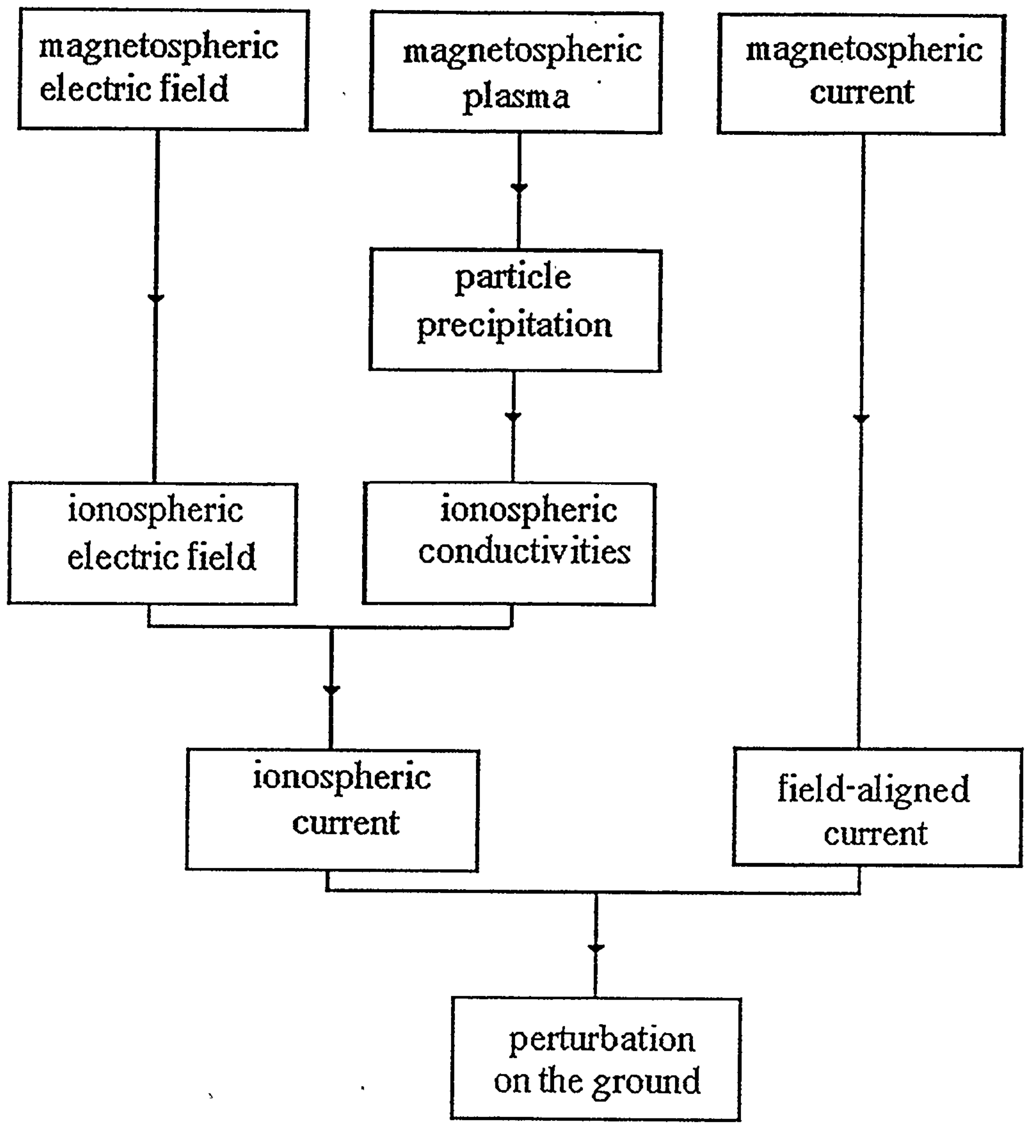


Figure 3.1. Flow chart of electric dynamic processes associated with aurora

a method comparing the results obtained from ASI and BARS data (Section 3.2 of this chapter), with the observations from MARIA . It examines the current system obtained from ASI and BARS data and also the consistency and correlation between these different observations. Section 3.5 briefly summarizes the new method, which enables a quantitative study of the three-dimensional current system in the auroral region. It also discusses the limitations of the application of this new method.

## 3.2 Ionospheric Current and Field-aligned Current Deduced from ASI and BARS Data

### 3.2.1 Height-integrated Pedersen and Hall Conductivities in the Auroral Region

The height-integrated conductivities in the auroral region can be divided into two different regions, the high conductivity region associated with the auroral arc in which the Pedersen and Hall conductivities are due mainly to precipitating particles, and the background region in which the conductivities are the result of solar radiation and cosmic rays.

The height dependent ionospheric Pedersen and Hall conductivities $\sigma_P$ and $\sigma_H$, respectively, are functions of the height distribution of electron density, ion - neutral collision frequency and ion gyro frequency( Brekke et al., 1974). The height-integrated values can be represented by

$$\Sigma_H = \int_{Z_1}^{Z_2} \sigma_H \, dZ \qquad (3.1)$$

$$\Sigma_P = \int_{Z_1}^{Z_2} \sigma_P \, dZ \tag{3.2}$$

where $\Sigma_P$ and $\Sigma_H$ are the height-integrated Pedersen and Hall conductivities, respectively, integrated from height $Z_1$ to $Z_2$.

In most cases, height-integrated Pedersen and Hall conductivities are estimated from equations (3.1) and (3.2) by using the electron density profiles. Vickrey et al. (1981) and Vondrak and Robinson (1985) have shown that conductivities can be calculated from the electron energy distribution. Robinson and Vondrak et al. (1987) found that for conductivities in auroral arcs it is efficient to use simple expressions that relate the energy flux and average energy of precipitating electrons to the height-integrated Pedersen and Hall conductivities by assuming Maxwellian electron energy distributions for which the average energy is twice the characteristic energy. The expressions relating Pedersen and Hall conductivities to the average energy and energy flux of the electrons can be expressed by (Robinson and Vondrak et al., 1987)

$$\Sigma_P = \frac{40\ E_M}{16 + E_M^2}\ \Phi_E^{\frac{1}{2}} \tag{3.3}$$

$$\frac{\Sigma_H}{\Sigma_P} = 0.45\ E_M^{0.85} \tag{3.4}$$

where $\Sigma_P$ and $\Sigma_H$ are the height-integrated Pedersen and Hall conductivities in mhos, respectively, $E_M$ is the average energy in kev and $\Phi_E$ is the energy flux in ergs / cm$^2$ · s. $\Sigma_P$ and $\Sigma_H$ in the equations (3.3) and (3.4) correspond to the height-integrated

Pedersen and Hall conductivities integrated between 80 km and 200 km altitude (Robinson et al., 1987).

Aurora is the light emitted by upper atmospheric species which are excited and /or ionized by an oncoming electron beam and also by complicated chains of photochemical processes after the electron collision (Chamberlain, 1961; Omholt, 1971; Vallance and Jones, 1974). The observed features of the spectrum are almost all due to lines and bands of neutral or ionized $N_2$, O, $O_2$ and N roughly in descending order of importance (Vallance Jones, 1974). The most familiar lines and bands of the auroral arc are:

the $N_2^+$ 1NG vibrational band at 427.8nm;

$O(^1D)$ - $O(^1S)$ line at 557.7nm (the green line);

$O(^3P)$ - $O(^1D)$ line at 630.0nm (the red line).

Rees and Luckey (1974) showed that the emissions from the forbidden red oxygen line (O I (630.0nm)) and from the permitted blue $N_2^+$ (0,1) first negative band ($N_2^+$ (427.8nm)) can be used to infer a characteristic energy $E_0$ and the energy flux $\Phi_E$ of the precipitating auroral electrons. Rees and Roble (1986) and Rees et al. (1988) related auroral emission rates I(630.0nm), I(427.8nm) and I(557.7nm) to the characteristic energy $E_0$ and the energy flux $\Phi_E$ of precipitating electrons. One of these expressions is written as (Rees and Roble, 1986)

$$\frac{4\pi\cdot I(427.8nm)\ (kR)}{\phi_E(ergs/cm^2\cdot s)} = 0.213E_0^{0.0735}(kev) \tag{3.5}$$

Steele and McEwen (1990) found that the relationship between the auroral column emission rate ratio I(630.0nm)/I(427.8nm) and the characteristic energy $E_0$ is the following formula:

$$\frac{4\pi I(630.0nm)}{4\pi I(427.8nm)} \simeq 3.3E_0^{-2.1}\ (kev) \tag{3.6}$$

Combining the equations (3.6), (3.5), (3.4) and (3.3), we can find height-integrated conductivities in the auroral arc region by noting that the average energy is twice the characteristic energy.

The height-integrated conductivities $\Sigma_P$ and $\Sigma_H$ in the background region are solely caused by the solar radiation and cosmic rays. Models have been established for computing $\Sigma_P$ and $\Sigma_H$ as functions of solar zenith angle ( Brekke et al., 1988; Metha, 1978; Vickrey et al., 1981, de la Beaujardiere et al., 1982; Robinson and Vondrak, 1984; Schlegel, 1987; Rasmussen et al., 1987). The models showed that the magnitude of the height-integrated Pedersen conductivity decreases with increasing solar zenith angle. When the zenith angle is bigger than $90^0$, there is a background level for $\Sigma_P$ caused by cosmic rays. In our situation we mostly choose the cases around midnight, so the solar zenith angle in our cases is bigger than $90^0$. Pedersen and Hall conductivities of 1 mho and 2 mhos (Brekke, private communication in 1991), respectively for our cases would be reasonable choices for the background levels.

### 3.2.2 Ionospheric Current and Field-aligned Current in the auroral region

The relationship of ionospheric ( horizontal ) current to the height-integrated Pedersen and Hall conductivities and electric fields in the auroral region can be expressed by Ohm's law, ignoring the ionospheric neutral wind:

$$\vec{J}_{\perp} = \Sigma_P \vec{E}_{\perp} - \Sigma_H \vec{E}_{\perp}\times\frac{\vec{B}}{B} \qquad (3.7)$$

where $\vec{J}_{\perp}$ is the height-integrated horizontal current intensity ( A/m), $\Sigma_P$ and $\Sigma_H$ are the height-integrated Pedersen and Hall conductivities in mhos, respectively, $\vec{E}_{\perp}$ is the ionospheric electric field in V/m which can be obtained from Eqn.(2.1) using the electron drift velocity that is measured by BARS. $\vec{B}$ is the vertical magnetic field at the auroral altitude. The magnitude of $\vec{B}$ overhead of Gillam is about $5 \times 10^{-5}$ T according to the earth's dipole magnetic field (user manual for BARS, 1989). In Eqn.(3.7), there is a sign difference. The reason is that BARS measures electron $\vec{E}\times\vec{B}$ drift velocities which are opposite to the current direction.

A geomagnetic cartesian coordinate system shown in Figure 3.3 and 3.4 is chosen to solve the problem. The x, y axis in the coordinate system are the geomagnetic north , east on the BARS map, respectively and the z axis is pointing down to the earth. Then, Equation (3.7) can be rewritten as:

$$J_{\perp}' = \Sigma_P E_{\perp}' - \Sigma_H E_{\perp}'' \qquad (3.8)$$

where $J_{\perp}'$ and $J_{\perp}''$ are the x and y components of $\vec{J}_{\perp}$ , $E_{\perp}'$ and $E_{\perp}''$ are the x and y

$$J_{\perp}'' = \Sigma_P E_{\perp}'' + \Sigma_H E_{\perp}' \qquad (3.9)$$

components of $\vec{E}_{\perp}$ .

According to the current continuity, the field-aligned ( parallel ) current can be obtained by

$$j_{\parallel} = \nabla \cdot \vec{J}_{\perp} \qquad (3.10)$$

where $j_{\parallel}$ is the field-aligned current in A/m$^2$ flowing in or out of the auroral region. If making an assumption that $j_{\parallel}$ is perpendicular to the horizontal plane, $j_{\parallel}$ at a certain pixel in the BARS field of view can be estimated by means of

$$j_{\parallel} = \frac{\Delta J_{\perp}'}{2\Delta x} + \frac{\Delta J_{\perp}''}{2\Delta y} \qquad (3.11)$$

where $\Delta J_{\perp}'$ and $\Delta J_{\perp}''$ are the changes of $J_{\perp}'$ and $J_{\perp}''$ along the x and y axes for the neighbouring two pixels and $\Delta x = \Delta y = 20$ km. In our field of view in the auroral region, because there are 25 x 16 pixels, which means there are 400 elements of Pedersen, Hall conductances and 400 electric field vectors, respectively, 400 horizontal current vectors and 400 parallel current vectors based on the equations (3.8), (3.9) and (3.10) can be produced.

## 3.3 Perturbations Produced by the Deduced Three-dimensional Current System in the Auroral Region

### 3.3.1 Perturbation Produced by the Ionospheric Current

The perturbation produced at each station in the Churchill line below the BARS map can be calculated by using the same geomagnetic cartesian coordinate system as above with the origin at the same station, where x, y axes along geomagnetic North and East, respectively and z axis pointing down to the earth. For example, Gillam is chosen as the origin of the coordinate system shown in Figure 3.3 in order to calculate the perturbation at Gillam. In such a coordinate system, let us first determine the position of each electric current vector on the BARS map. If m and n are used to represent the number of the rows and columns for this electric current vector on the BARS map, the coordinate of this current vector will be $[(m - m_0)\Delta x, (n_0 - n)\Delta y, -h]$, where $m_0$ and $n_0$ are the number of rows and columns, respectively, of the pixel just above Gillam, $\Delta x$ and $\Delta y$ are equal to 20 km, respectively, and h is equal to 110 km. Then the perturbation on the ground produced by each ionospheric current vector overhead can be calculated by means of Biot-Savart's law.

In this coordinate system, the following parameters are defined

$$\begin{aligned} \vec{J}_{mn} &= J'_{mn}\vec{i} + J''_{mn}\vec{j} \\ \Delta\vec{B}_{mn} &= \Delta B'_{mn}\,\vec{i} + \Delta B''_{mn}\,\vec{j} + \Delta B'''_{mn}\,\vec{k} \end{aligned} \qquad (3.12)$$

where, $\Delta\vec{B}_{mn}$ is the perturbation produced by the mnth ionospheric current vector $\vec{J}_{mn}$ . $\Delta B'_{mn}$ , $\Delta B''_{mn}$ and $\Delta B'''_{mn}$ are the x, y and z components of $\Delta\vec{B}_{mn}$ , respectively

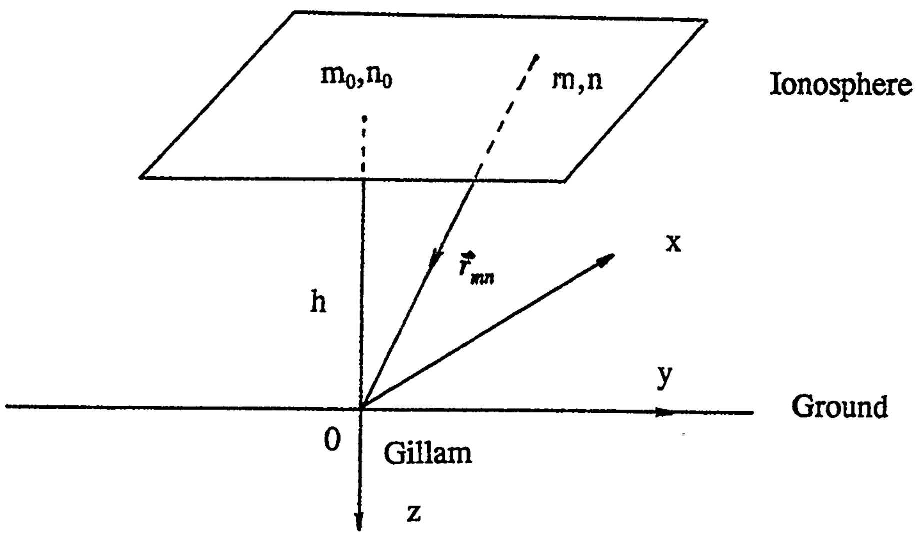


Figure 3.2 The geomagnetic cartesian coordinate system for calculating the perturbation due to ionospheric current vectors

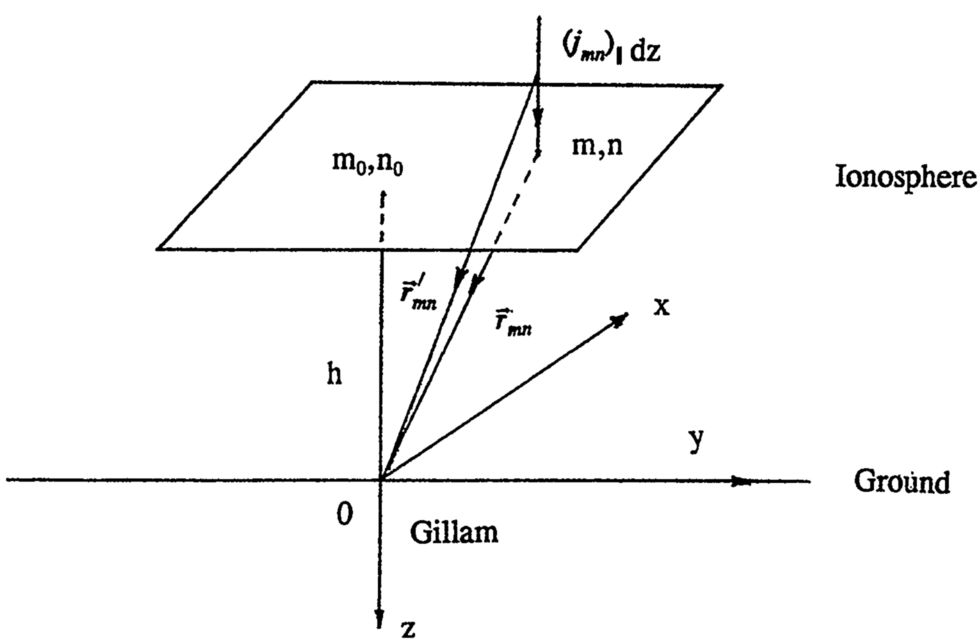


Figure 3.3 The geomagnetic cartesian coordinate system for calculating the perturbation due to field-aligned current vectors

and $J'_{mn}$ , $J''_{mn}$ and $J'''_{mn}$ are the x, y and z components of $\vec{J}_{mn}$ , respectively. Then, the Biot-Savart's law is expressed as

$$\Delta\vec{B}_{mn}=\frac{\mu_0}{4\pi}\frac{\vec{J}_{mn}\Delta x\Delta y\times\vec{r}_{mn}}{|\vec{r}_{mn}|^3} \tag{3.13}$$

where,

$$\vec{r}_{mn} = (m-m_0)\,\Delta x\;\vec{i} + (n_0-n)\,\Delta y\;\vec{j} - h\;\vec{k}$$

So, Eqn.(3.13) can be rewritten in a matrix format:

$$\begin{pmatrix}\Delta B'_{mn}\\ \Delta B''_{mn}\\ \Delta B'''_{mn}\end{pmatrix}=\frac{\mu_0}{4\pi}r_{mn}^{-3}\begin{pmatrix}J''_{mn}\Delta x\Delta y\;h\\ -J'_{mn}\Delta y\Delta x\;h\\ (n_0-n)\,\Delta y J'_{mn}\Delta x^2+(m_0-m)\,J''_{mn}\Delta x\Delta y^2\end{pmatrix} \tag{3.14}$$

Since $\Delta$x and $\Delta$y are equal in our case, Equation (3.14) can be changed to

$$\begin{pmatrix}\Delta B'_{mn}\\ \Delta B''_{mn}\\ \Delta B'''_{mn}\end{pmatrix}=\frac{\mu_0}{4\pi}r_{mn}^{-3}\Delta x^2 h\begin{pmatrix}J''_{mn}\\ -J'_{mn}\\ [\,(n_0-n)\,J'_{mn}+(m_0-m)\,J''_{mn}]\,\dfrac{\Delta x}{h}\end{pmatrix} \tag{3.15}$$

Finally, the total perturbation produced by the total ionospheric current vectors on the BARS map is equal to

$$\begin{pmatrix}\Delta B'_{I}\\ \Delta B''_{I}\\ \Delta B'''_{I}\end{pmatrix}=\frac{\mu_0}{4\pi}\sum_{m=1}^{25}\sum_{n=1}^{16}r_{mn}^{-3}\Delta x^2 h\begin{pmatrix}J''_{mn}\\ -J'_{mn}\\ [\,(n_0-n)\,J'_{mn}+(m_0-m)\,J''_{mn}]\,\dfrac{\Delta x}{h}\end{pmatrix} \tag{3.16}$$

where $\Delta B'_I$ , $\Delta B''_I$ and $\Delta B'''_I$ are, respectively, x, y and z components of the total perturbation produced by all the ionospheric current vectors on the BARS map.

Similar expressions can be found for calculating the perturbation at Back and other stations by choosing corresponding $m_0$ and $n_0$.

### 3.3.2 Perturbation Produced by the Field-Aligned Current

The same coordinate system as above is chosen, shown in Figure 3.4, to calculate the perturbation on the ground produced by the field-aligned current vectors. If the field-aligned current vectors overhead are assumed to extend an infinite distance above the field of view to flow into or out of the ionosphere, the expression of the perturbation produced by the field-aligned current vector at the mnth pixel by Biot-Savart's law is written as,

$$(\Delta\vec{B}_{mn})_{\parallel} = \frac{\mu_0}{4\pi}\int_{-\infty}^{-h} \frac{(j_{mn})_{\parallel}\Delta x\ \Delta y\ d\vec{z} \times \vec{r}'_{mn}}{|\vec{r}'_{mn}|^3} \qquad (3.17)$$

where $(\Delta\vec{B}_{mn})_{\parallel}$ is the perturbation on the ground produced by the field-aligned current vector at the mnth pixel, $(j_{mn})_{\parallel}$ is the field-aligned current density ( $A/m^2$ ) at the mnth pixel, $\Delta x$ and $\Delta y$ are still equal to 20 km, respectively and $\vec{r}'_{mn} = [\,(m-m_0)\,\Delta x,\ (n_0-n)\,\Delta y,\ -z]$ is the vector from the mnth current source to the origin. Then,

$$(\Delta\vec{B}_{mn})_{\parallel} = \frac{\mu_0}{4\pi}\,[\,(n-n_0)\,(j_{mn})_{\parallel}\Delta x^3\vec{i} - (m_0-m)\,(j_{mn})_{\parallel}\Delta x^3\vec{j}\,]\int_{-\infty}^{-h}\frac{dz}{|\vec{r}'_{mn}|^3}$$

or

$$= \frac{\mu_0}{4\pi}(j_{mn})_{\parallel}\Delta x^3[(n-n_0)\vec{i} - (m_0-m)\vec{j}]\int_{-\infty}^{-h} \frac{dz}{[(m_0-m)^2\Delta x^2+(n-n_0)^2\Delta y^2+z^2]}$$

$$= \frac{\mu_0}{4\pi}(j_{mn})_{\parallel}\Delta x^3[(n-n_0)\vec{i}-(m_0-m)\vec{j}]\frac{1-\frac{h}{r_{mn}}}{(m_0-m)^2\Delta x^2+(n-n_0)^2\Delta y^2}$$

$$= \frac{\mu_0}{4\pi}(j_{mn})_{\parallel}\,\Delta x\,\frac{(n-n_0)\vec{i} - (m_0-m)\vec{j}}{(m_0-m)^2+(n-n_0)^2}(1-\frac{h}{r_{mn}}) \quad (3.18)$$

$$\begin{pmatrix}(\Delta B'_{mn})_{\parallel}\\(\Delta B''_{mn})_{\parallel}\end{pmatrix} = \frac{\mu_0}{4\pi}(j_{mn})_{\parallel}\Delta x\frac{1-\frac{h}{r_{mn}}}{[(m_0-m)^2 + (n-n_0)^2]}\begin{pmatrix}(n-n_0)\\-(m_0-m)\end{pmatrix} \quad (3.19)$$

where, $(\Delta B'_{mn})_{\parallel}$ and $(\Delta B''_{mn})_{\parallel}$ are the x and y components of $(\Delta \vec{B}_{mn})_{\parallel}$ . The total perturbation produced by the total field-aligned current vectors on the BARS map is equal to

$$\begin{pmatrix}\Delta B'_{\parallel}\\\Delta B''_{\parallel}\end{pmatrix} = \frac{\mu_0}{4\pi}\Delta x\sum_{m=1}^{25}\sum_{n=1}^{16}(j_{mn})_{\parallel}\frac{1-\frac{h}{r_{mn}}}{(m_0-m)^2+(n-n_0)^2}\begin{pmatrix}(n-n_0)\\-(m_0-m)\end{pmatrix} \quad (3.20)$$

where $\Delta B'_{\parallel}$ and $\Delta B''_{\parallel}$ are x and y components of the total perturbation $\Delta\vec{B}_{\parallel}$ produced by all field-aligned current vectors.

## 3.4 Comparison of the Deduced Perturbations with the Magnetic Observation by

MARIA

The MARIA data are magnetic perturbations on the ground recorded by the Magnetometer and Riometer Array (MARIA), which consists of 13 magnetometers, riometers and tellurometers shown in Figure 2.1.

From ASI and BARS data, the distribution of a three-dimensional current system in our field of view of the auroral region can be found, so that the total perturbation on the ground produced by such a current system can be calculated. For a selected period of time, the time variation of the calculated perturbation at Gillam or Back station can be obtained and then it can be compared with observed MARIA data to see if they are correlated or consistent with each other and examine the current system derived from the method developed.

## 3.5 Summary and Discussion

As shown above, a method to construct a three-dimensional current system in the auroral region based on ASI, BARS and MARIA data was introduced. First, ionospheric current and field-aligned current vectors are calculated from ASI and BARS data. Then, these current vectors are converted into a magnetic perturbation on the ground. Finally, the perturbation calculated from ASI and BARS data can be compared with the magnetic observations from MARIA data. A flow chart in Figure 3.5 indicates a procedure of this analysis.

This new method of studying three-dimensional current systems in auroral region has two limitations: (1) It ignores the disturbances produced by other current sources in

MARIA data when comparing, such as the ones in the magnetosphere and those induced in the interior of the earth; (2) It neglects the uncertainties of all measurements. These two factors may affect the accuracy of the examination.

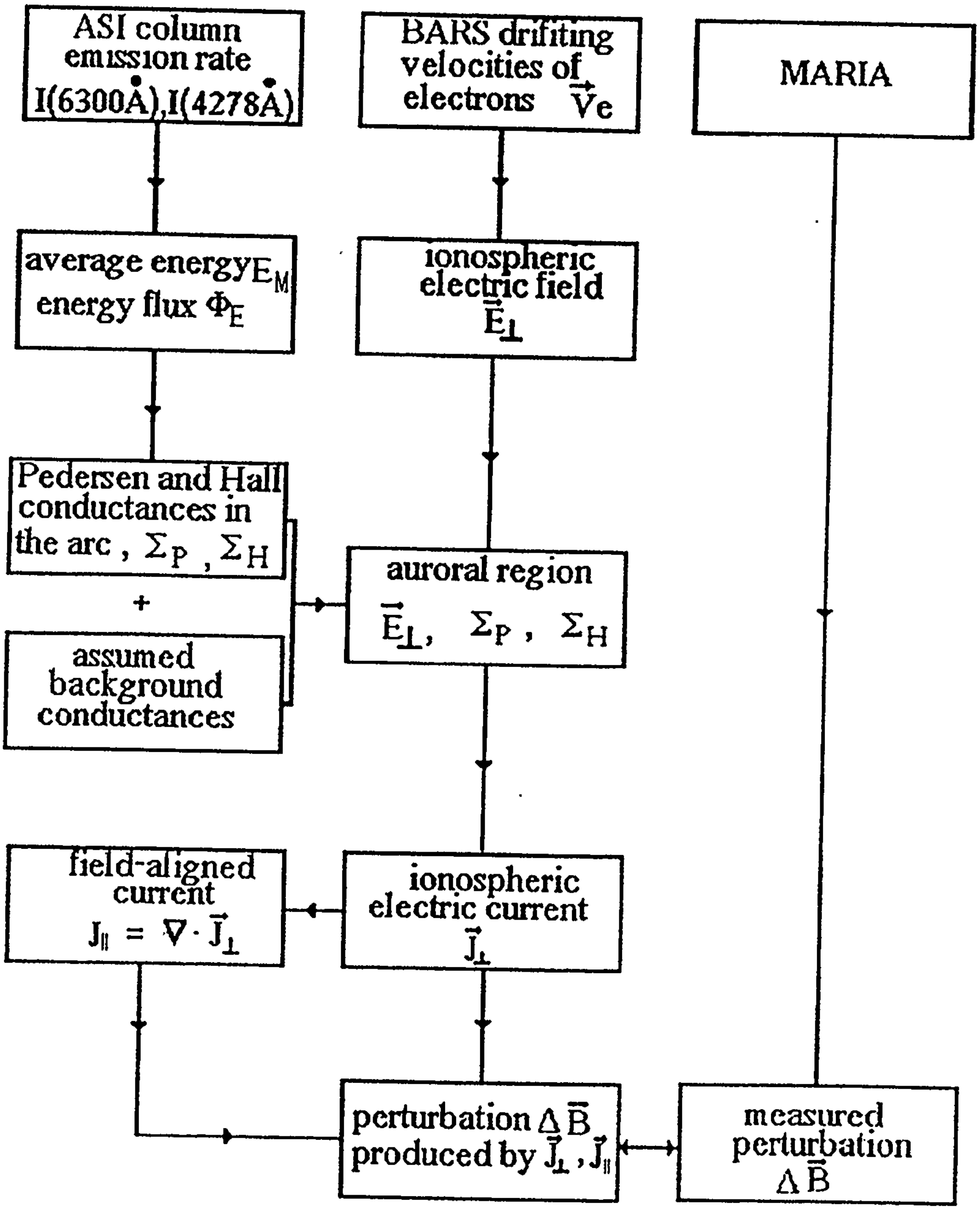


Figure 3.4 Flow chart of a three-dimensional current system constructed from ASI, BARS and MARIA data

# CHAPTER IV. DATA ANALYSIS

## 4.1 Data Selection and Data Processing

### 4.1.1 Data Selection

Since we need three kinds of data to solve our problem, the data selection is important.

There are several requirements when selecting data for processing. First, we must have ASI images, BARS electric fields and magnetic perturbations from MARIA observed at the same time. This condition is hard to satisfy because these three measurements may not be consistently obtained. These three instruments function differently and the field of view of MARIA is different from that of the other two. Second, we require that both 427.8nm and 630.0nm auroral emissions were observed over a time period of seven minutes or so. Third, we desire BARS data to have many electric field vectors in its field of view. Due to the principle of the Bistatic Auroral Radar System, we do not have BARS electric field vectors when the two radars did not observe the irregularities of the plasma at the same region. Finally, it is desirable to have magnetic perturbations observed by MARIA at the specific station above which BARS electric field vectors were observed.

The above requirements were satisfied by the three cases in 1990 that were selected for analysis. The information about these three cases are listed in Table 4.1.

Table 4.1 List of the three cases

| Days (M,D,Y) | time period (UT) | $k_p$ index in time period | Max.I(427.8nm), I(630.0nm)(kR) | Electric field $E_\perp$ (V/m) |
|---|---|---|---|---|
| 02/24/90 | 02:09-02:17 | 5+ | 8, 9 | ~0.01 |
| 02/25/90 | 04:34-04:40 | 5 | 27, 8.8 | ~0.01 |
| 03/21/90 | 03:39-03:48 | 6- | 2, 9.4 | ~0.01 |

### 4.1.2 Data Processing

Based upon the theory outlined above, a computer code was developed to process the data in the BARS field of view which consists of 25 $\times$ 16 superpixels. In the first step the Pedersen and Hall conductivities for each pixel of the BARS field of view was computed. In this step, the BARS field of view was simply divided in two regions, auroral arc region and its background region. The conductivity for each pixel in the auroral arc was computed based on the empirical formulas of Eqn.3.3, Eqn.3.4, Eqn.3.5 and Eqn.3.6 provided in Chapter III. Before the computation was begun a background value was subtracted from the arc intensities for each column of the images. The conductivities for the background region were assumed to be 1 mho for Pedersen and 2 mhos for Hall conductivity ( Brekke, private conversation in 1991). Any conductivity caused by diffuse aurora in this region outside of the arc was not considered. In the second step, the horizontal ionospheric current vector and vertical field-aligned current vector for each pixel were computed by combining the computed conductivities from the first step and the measured BARS electric field vectors using Equations 3.8, 3.9 and 3.11 in Chapter III. Since the time resolutions for ASI and BARS are different ( ASI images are collected every 20 seconds and BARS vectors are recorded every 30 seconds ), both ASI and BARS data were averaged over one minute to avoid this problem , which means three ASI images and two BARS measurements in one minute were used to calculate the average, then ionospheric or field-aligned current vectors in the BARS map could be obtained every minute. The last step was to calculate the perturbation at a station caused by all calculated ionospheric current vectors and field-aligned current vectors in the BARS map. The calculated magnetic perturbation was compared with the observed magnetic perturbation from MARIA data. Since all the stations in the entire Churchill line except Gillam and Back are at the edge or outside of the field of view, only these two stations will be discussed in the following chapters.

MARIA observes total magnetic field variations on the ground. To determine magnetic perturbations from MARIA data, the choice of a baseline is very important. Dr. D. D. Wallis (private conversation, 1992) developed a computing code to use some parameters found from all the quiet days in the year of 1990 to calculate baselines. The baseline changes during 24 hrs, but it remains the same within a short period of several minutes. Another method is to take an average value over 24 hrs. These two methods are not very useful for the cases which will be discussed in the following sections. In these cases the time period is only about nine minutes, so the baseline cannot change much in this period. Besides, the aurora outside this period is weak enough to be relatively unimportant. In other words, the magnetic observation outside the period should be the baseline to determine the perturbation within the period. Obviously, this baseline is not a DC value, but a value containing some perturbation caused by other current sources. As a result, this study tends to compare the magnetic perturbation caused by only the current source within the BARS field of view which ASI could observe and avoid the part of the perturbation from the current sources outside the field of view as much as possible.

## 4.2 Feb.24, 1990

The $k_p$ index sum for this day is 32+. The ASI images during the time period from UT02:09:00 to UT02:17:00 for the two wavelengths of 427.8nm and 630.0nm on this day are shown in Figure 4.2.1(a) and (b), where each image is formed by an average value of the three images in each minute, since the temporal resolution of the ASI is 20s. Figure 4.2.1 shows the intensities of the auroral emissions for the wavelengths of 427.8nm and 630.0nm during that time period within the BARS field of view and the intensities are colour coded with black indicating the minimum intensity and red indicating the maximum intensity. The coordinate system in Figure 4.2.1(a) and (b) is in EDFL ( eccentric dipole field line ) latitudes from $63.0^0$ to $67.8^0$ for the north direction and EDFL longitude from $333^0$ to $340.5^0$ for the east direction. The aurora during this period is more quiet and narrower for the last six minutes and in a spiral situation for the first three minutes according to the counterclockwise rotation of the arc (viewed from the magnetic field lines), seen from Figure 4.2.1(a). The aurora before and after this time period was relatively weak and hardly visible in the ASI images. The electric field vectors, deduced from the BARS-measured electron drift velocities, overlaid on the auroral arc contours for the wavelength 427.8nm at each minute in the same time period are shown in Figure 4.2.2. In Figure 4.2.2 the electric field for each picture is an average over one minute (temporal resolution of the BARS is 30s) and the arc's first contour is 1 kR (Kilo-Rayleigh) and the interval between two contours is 2 kR. From Figure 4.2.2 the spatial and temporal variation of the electric field in the BARS field of view can be studied and the relative location of the electric field vectors and the auroral arc can also be seen. The electric field vectors are partially on the north side of the arc and partially in the arc for this case. Those on the north side of the arc mainly point toward the arc in the southwestward direction for the first six minutes and turn to almost northward in the last three minutes. The electric field vectors in the arc point toward the centre of the spiral arc in the first three minutes and change to cross the arc in a southwestward direction when the aurora becomes more quiet in the last few minutes. The magnitudes of the electric field vectors are not noticeably different outside and inside the arc. Figure 4.2.2 also shows that the arc was located almost directly above the Gillam station.

### 4.2.1 The Calculated Ionospheric (horizontal) Current Vectors and Field-aligned Currents in the BARS Field of View

After calculating the Pedersen and Hall conductivities in the auroral arc for this case from the equations of (3.3), (3.4), (3.5) and (3.6), the equations of (3.8) and (3.9) were applied to calculate the ionospheric (horizontal) current vectors. The calculated ionospheric current vectors overlaid on the auroral arc contours for the wavelength of

427.8nm at each minute in this period of this case are shown in Figure 4.2.3, where the arc contours start from 1 kR and increase every 2 kR. The calculated Pedersen and Hall conductivities in the auroral arc are high, up to 26 mhos and 55 mhos, respectively. The ratio between the two conductivities is about 2 in the arc and also outside the arc. The calculated current vectors outside the arc are very small compared to the ones inside the arc due to the high conductivities in the arc. The current vectors outside the arc flow around the edge of the arc and in the northwestward direction. The current vectors inside the arc flow around the spiral pattern counterclockwise for the first three minutes and along the arc pattern in the westward direction for the more quiet situation in the last six minutes. They become more intense when the auroral arc gets more active. The intensities of the current vectors in Figure 4.2.3 are indicated by the lengths of the vectors and of the order of $10^{-1}$ A/m. Figure 4.2.4 shows the calculated field-aligned currents from the current continuity of Eqn.(3.11), overlaid on the auroral arc contours for the wavelength of 427.8nm. In Figure 4.2.4 the densities of the field-aligned currents are colour coded and the group of the 16 colours are divided to two region by the colour labelled zero, where the upper colour region indicates downward field-aligned currents and the lower region indicates upward field-aligned currents. The magnitudes for either downward field-aligned currents or upward field-aligned currents are represented by different colours and increase from the colour labelled zero. The arc contours in Figure 4.2.4 start from 1 kR and increase every 2 kR. The coordinate system in Figure 4.2.4 is in EDFL latitudes from $63.0^0$ to $67.8^0$ for the north direction and EDFL longitudes from $333.0^0$ to $340.5^0$ for the east direction. In Figure 4.2.4, the field-aligned currents

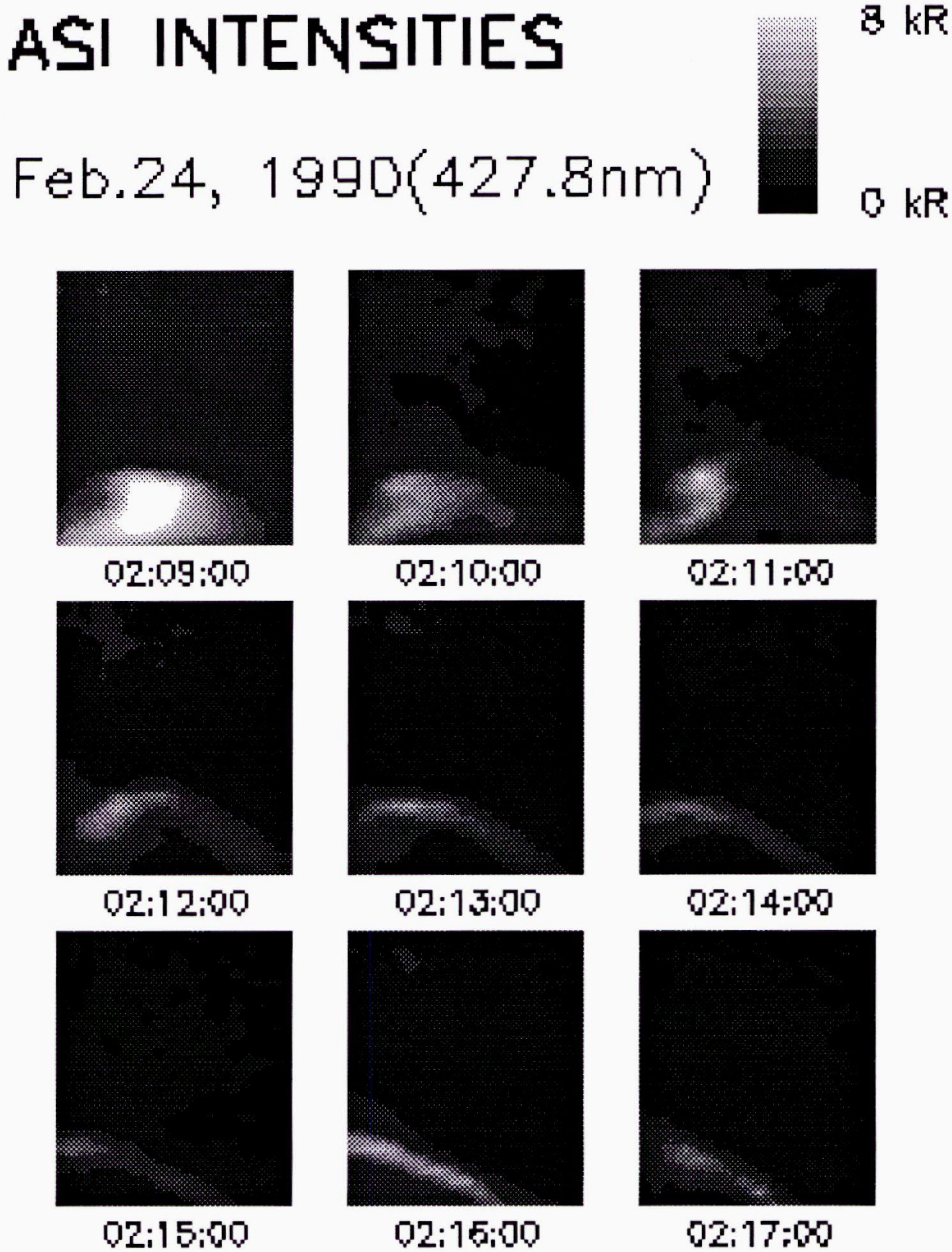


Figure 4.2.1(a) The one-minute averaged ASI images for the wavelength of 427.8nm during the time period from UT 02:09:00 to UT 02:17:00 on Feb.24, 1990. The intensities in Kilo-Rayleighs are colour coded with black indicating the minimum intensity and red indicating the maximum intensity. The coordinate system is in EDFL latitudes from $63.0^0$ to $67.8^0$ on the north and EDFL longitudes from $333.0^0$ to $340.5^0$ on the east.

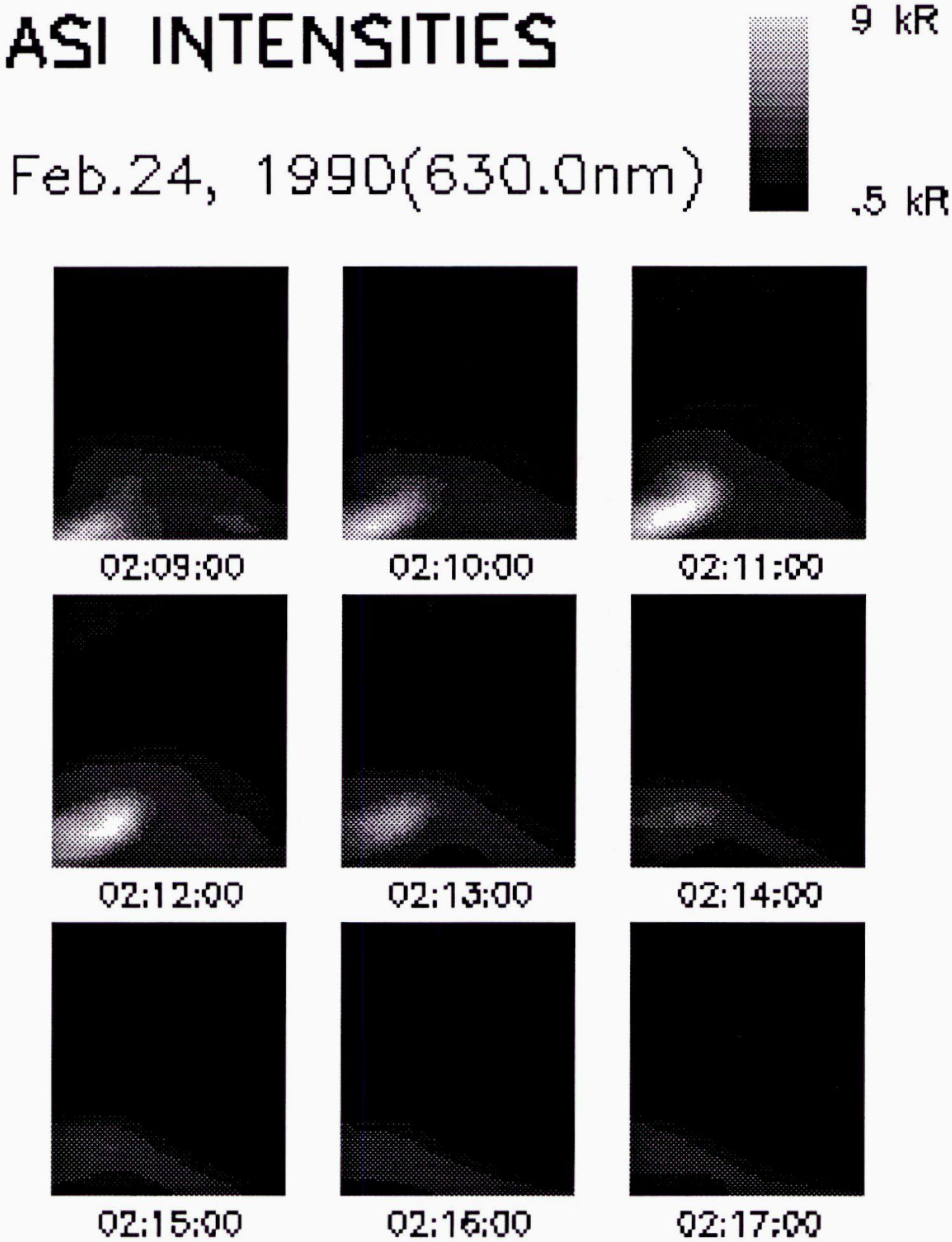


Figure 4.2.1(b) The one-minute averaged ASI images for the wavelength of 630.0nm during the time period from UT 02:09:00 to UT 02:17:00 on Feb.24, 1990. The intensities in Kilo-Rayleighs are colour coded with black indicating the minimum intensity and red indicating the maximum intensity. The coordinate system is in EDFL latitudes from $63.0^0$ to $67.8^0$ on the north and EDFL longitudes from $333.0^0$ to $340.5^0$ on the east.

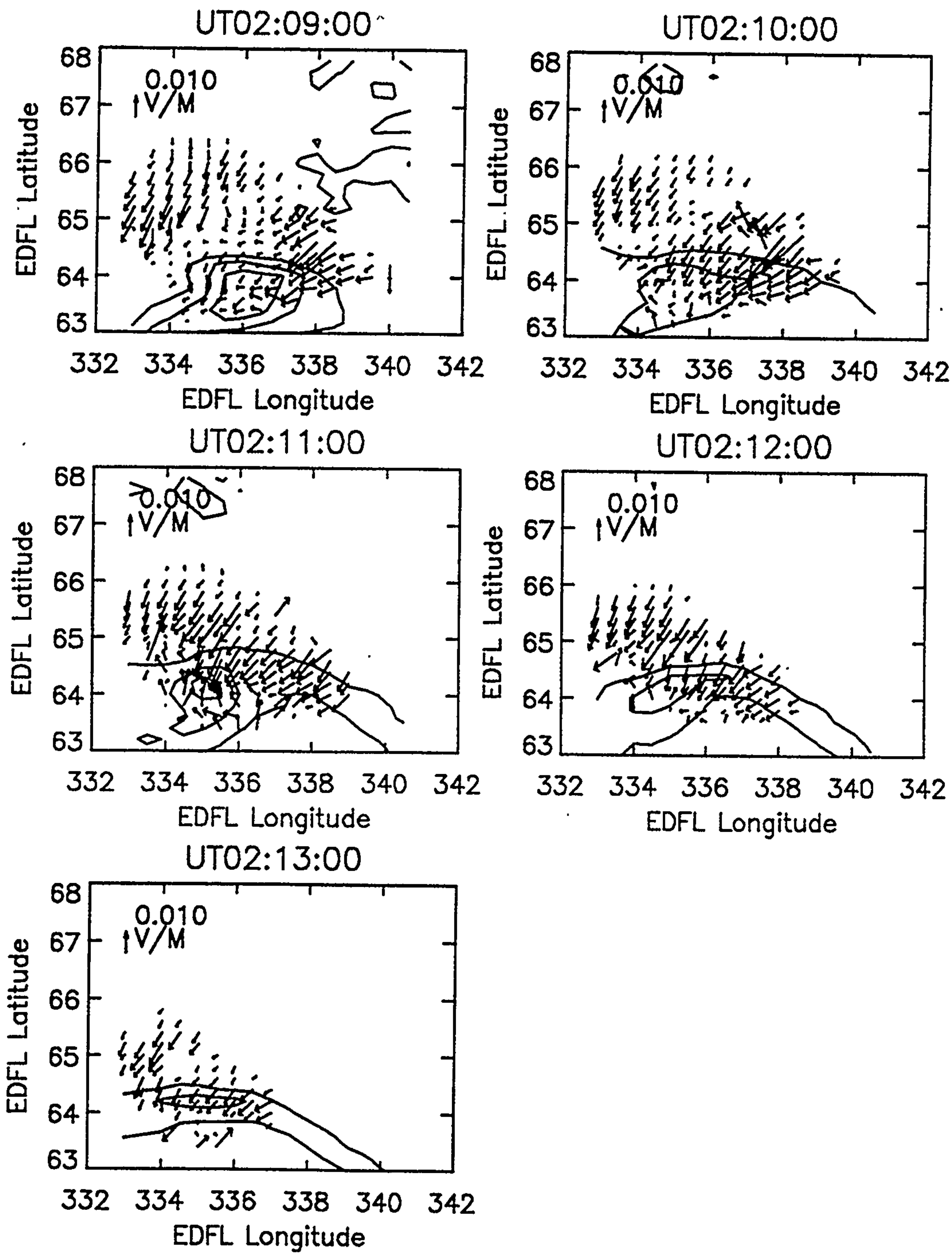


Figure 4.2.2(a) The electric fields, measured from the BARS, overlaid on the auroral contour during the time period of UT02:09:00 to UT02:13:00 on Feb.24, 1990. The vector length denotes the magnitudes of the electric field vectors referenced by the scale defined on the top. The arc contours start from 1 kR and increase by steps of 2 kR.

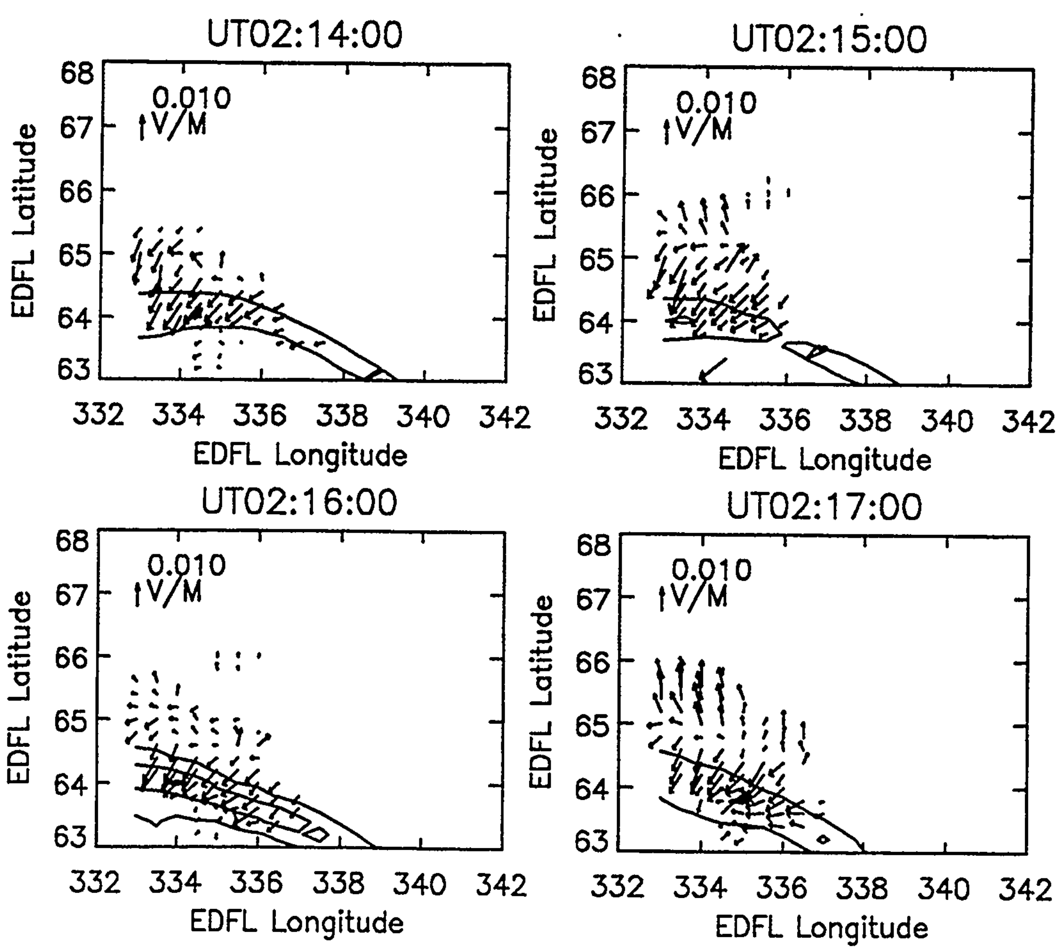


Figure 4.2.2(b) The electric fields, measured from the BARS, overlaid on the auroral contour during the time period of UT02:14:00 to UT02:17:00 on Feb.24, 1990. The vector length denotes the magnitudes of the electric field vectors referenced by the scale defined on the top. The arc contours start from 1 kR and increase by steps of 2 kR.

change their configurations within one minute especially for the first three minutes. The field-aligned currents outside the auroral arc are very weak and mainly downward currents, but the ones inside the arc are relatively strong. The upward and downward field-aligned currents inside the arc are formed mainly in two sheets. The upward current is on one side and downward current on the other side. When the arc is relatively quiet, such as in the last six minutes, the downward current is on the east side and the upward current is on the west side since the ionospheric current flows along the arc in the westward direction shown in Figure 4.2.3. When the arc is more active and has a spiral, such as the situation in the first three minutes, the upward current is on the north side and the downward current is on the south side because there is a northward component of the ionospheric current shown in Figure 4.2.3. Therefore, the upward and downward field-aligned currents and the ionospheric current consist of a three-dimensional current system in the BARS field of view in the ionosphere and satisfy the current continuity. For this case the densities of the calculated field-aligned currents are high, up to the order of $10^{-5}$ $A/m^2$.

### 4.2.2 Comparison of the Perturbations at Gillam station

The time variations of the calculated and observed magnetic perturbations at the Gillam station is shown in Figure 4.2.5, where the baseline was chosen to determine the observed magnetic perturbation according to the method described in the first part of this chapter. In Figure 4.2.5 a factor was used to magnify each of the x, y and z components of the calculated magnetic perturbation in order to compare the temporal variation. The factors for x, y and z are 2, 2 and 9, respectively. From Figure 4.2.5, it is clearly seen

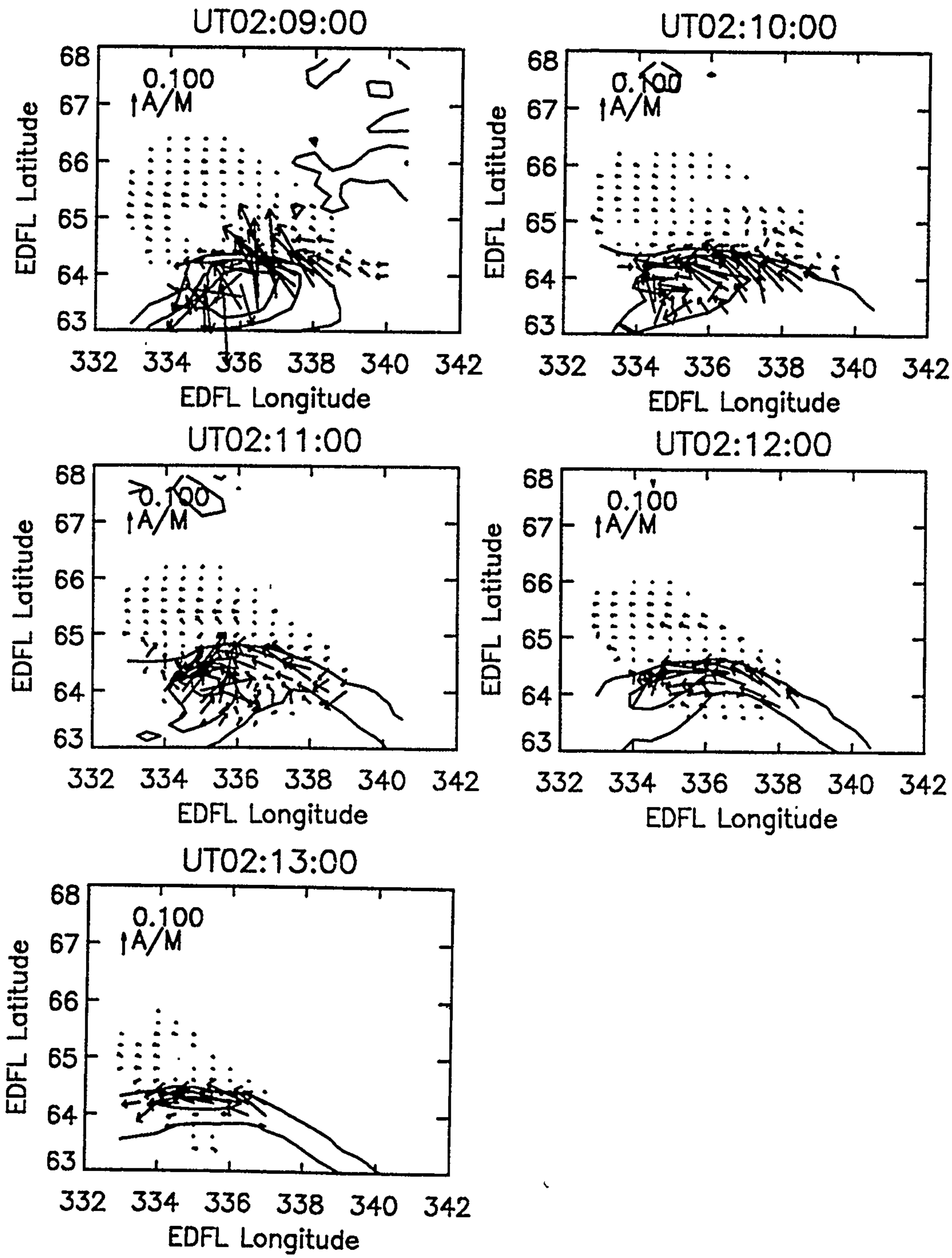


Figure 4.2.3(a) The calculated horizontal ionospheric electric current vectors, overlaid on the auroral contour during the time period of UT02:09:00 to UT02:13:00 on Feb.24, 1990. The vector length denotes the magnitudes of the current referenced by the scale defined on the top. The arc contours start from 1 kR and increase by steps of 2 kR.

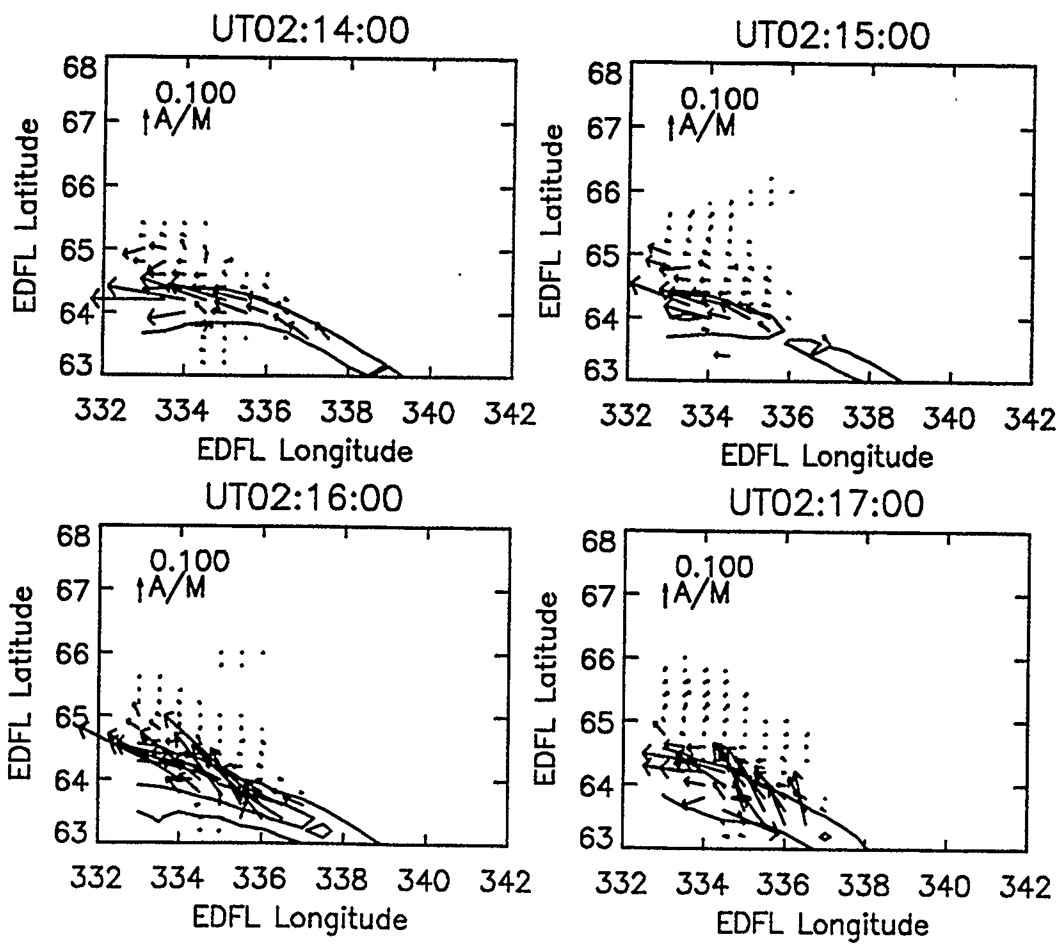


Figure 4.2.3(b) The calculated horizontal ionospheric electric current vectors, overlaid on the auroral contour during the time period of UT02:14:00 to UT02:17:00 on Feb.24, 1990. The vector length denotes the magnitudes of the current referenced by the scale defined on the top. The arc contours start from 1 kR and increase by steps of 2 kR.

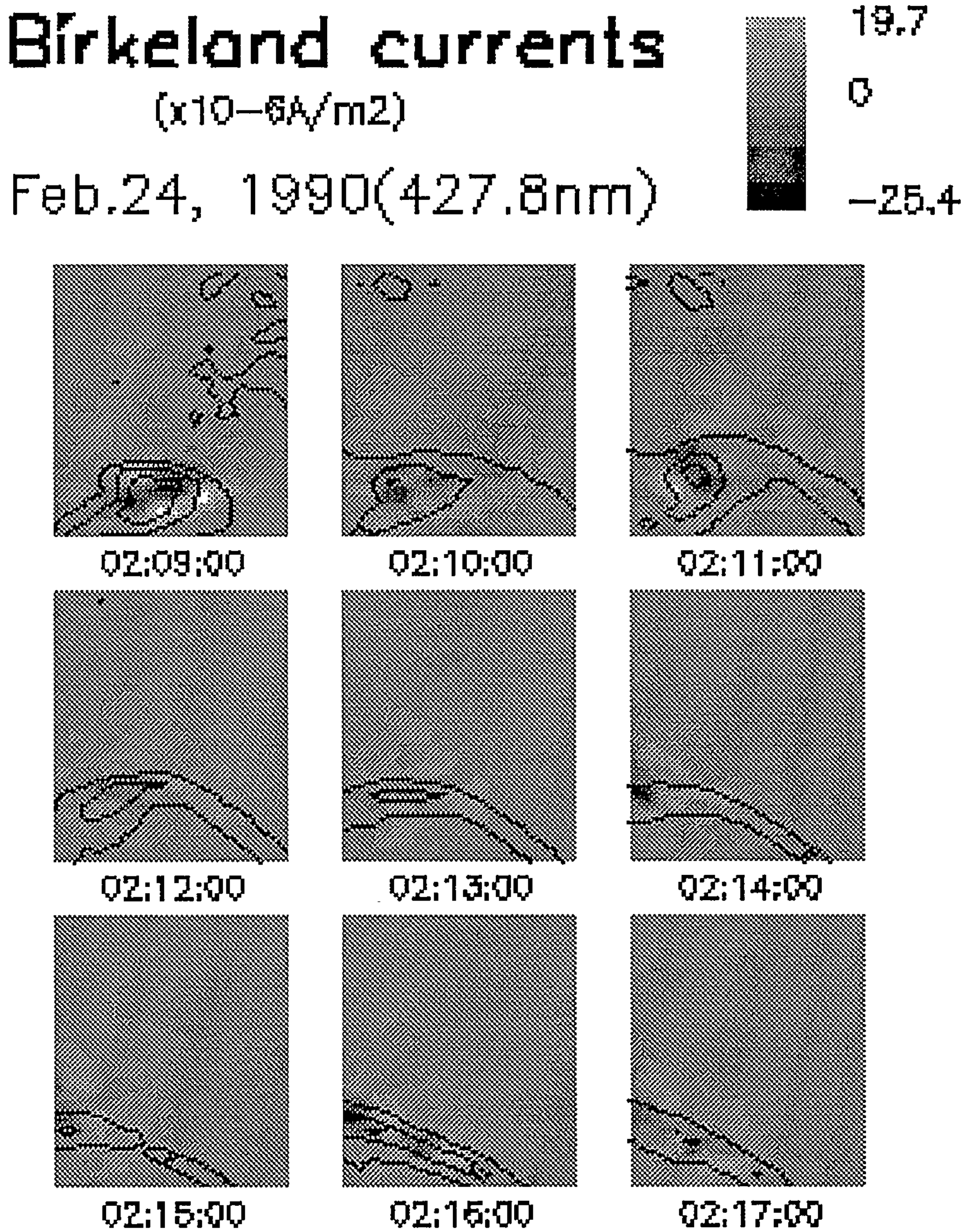


Figure 4.2.4 The calculated field-aligned currents overlaid on the auroral contour of the wavelength of 427.8nm during the time period from UT 02:09:00 to UT 02:17:00 on Feb.24, 1990. The densities in $\mu A/m^2$ are colour coded and the colour labelled zero divides the colour region to two region, with top colours indicating downward field-aligned currents and bottom colours indicating upward field-aligned currents. The coordinate system is in EDFL latitudes from $63.0^0$ to $67.8^0$ on the north and EDFL longitudes from $333.0^0$ to $340.5^0$ on the east.

that the time variation of the calculated magnetic perturbation follows that of the observation very well. The calculated horizontal ionospheric current vectors and field-aligned vectors for this case locate about overhead of the Gillam station ($63.9^0$ N, $336.06^0$ E in EDFL), seen from Figure 4.2.3 and 4.2.4. Those current vectors have a strong magnetic influence on the Gillam station.

### 4.2.3 Comparison of the Perturbations at Back Station

Figure 4.2.6 shows the time variations of the calculated and observed magnetic perturbations at Back station. The magnifying factor for each of the x, y and z components of the calculated perturbation at Back station, shown in Figure 4.2.6, is 2, 5 and 2, respectively. In Figure 4.2.6, the x component of the computed magnetic perturbation agree with the observation, and its z component is only slightly different from the observation but an obvious difference exists in the y components.

## 4.3 Feb.25, 1990

The $k_p$ index sum for this day is 33-. The one-minute averaged ASI images during the time period from UT04:34:00 to UT04:40:00 for the two different wavelengths of 427.8nm and 630.0nm on this day are shown in Figure 4.3.1.(a) and (b), respectively. The colour scales for the intensities of the auroral emissions and the coordinate system in Figure 4.3.1(a) and (b) are defined the same as for Figure 4.2.1. It is seen from Figure 4.3.1(a) and (b) that the intensities for the two different wavelengths during this time period are high, up to 27 kR and 9 kR, respectively and the auroral arc during this time period is not quiet but distorted. An eastward movement of the most intense portion of the arc can be seen in Figure 4.3.1(a). The arc pattern for the wavelength of 630.0nm in Figure 4.3.1(b) is a little bit different from Figure 4.3.1(a) and is more uniform. The electric fields, deduced from the BARS-measured electron drift velocities, overlaid on the auroral arc contours for the wavelength of 427.8nm at each minute are shown in Figure 4.3.2, where the arc contours start from 2 kR and increase every 4 kR. In Figure 4.3.2 the electric field vectors are partially at the north side of the arc and partially in the arc for this case. The electric field vectors on the north side mainly point toward the south but the lower part tends to be northeastward or northwestward in the later time. The electric field vectors in the arc mainly cross the arc in a southwestward direction. The magnitudes of the electric field vectors outside and inside the arc are not very different in this case. Figure 4.3.2 also shows the relative location of the auroral arc and the electric field vectors.

### 4.3.1 The Calculated Ionospheric (horizontal) Current Vectors and Field-aligned Currents in the BARS Field of View

Applying the same procedures as to find the ionospheric current vectors in Figure 4.2.3, the ionospheric (horizontal) current vectors at each minute for this case could be calculated and the result of the calculation is shown in Figure 4.3.3, where the auroral arc contours for the wavelength of 427.8nm are overlaid on and the start contour is 2 kR and the interval of the contours is 4 kR. The calculated Pedersen and Hall conductivities in the auroral arc for this case range up to 20 mhos and 40 mhos, respectively and the ratio between the two conductivities is about 2 in the arc and also outside the arc. The current vectors outside of the arc, shown in Figure 4.3.3, are very small relative to the

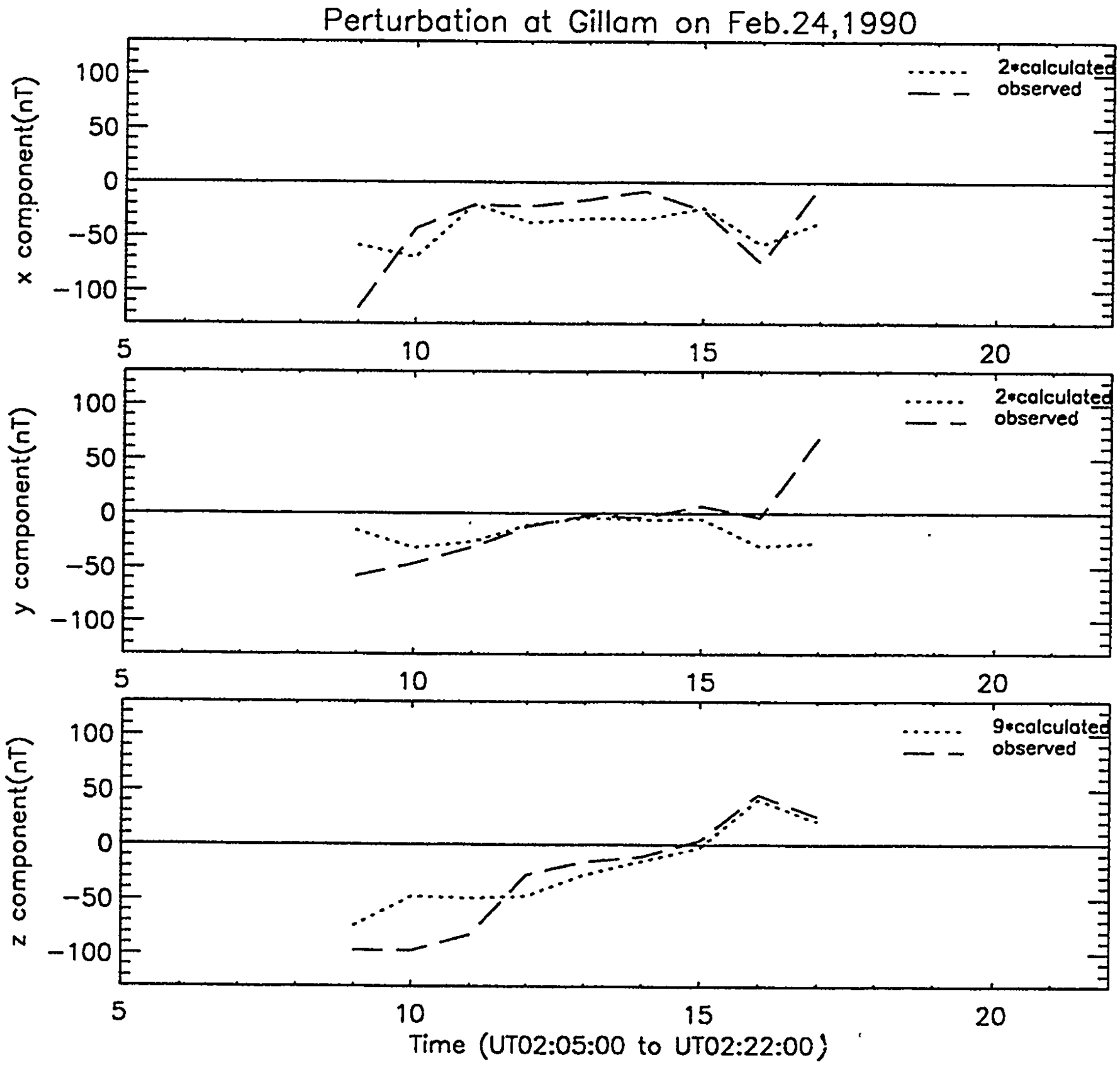


Figure 4.2.5 The time variations of the calculated and observed magnetic perturbations at Gillam during the time period of UT02:09:00 to UT02:17:00 on Feb.24, 1990. The dotted lines indicate the calculated perturbation and dash lines indicate the observed perturbation. There is a factor multiplying to each component of the calculated perturbation shown in the figure.

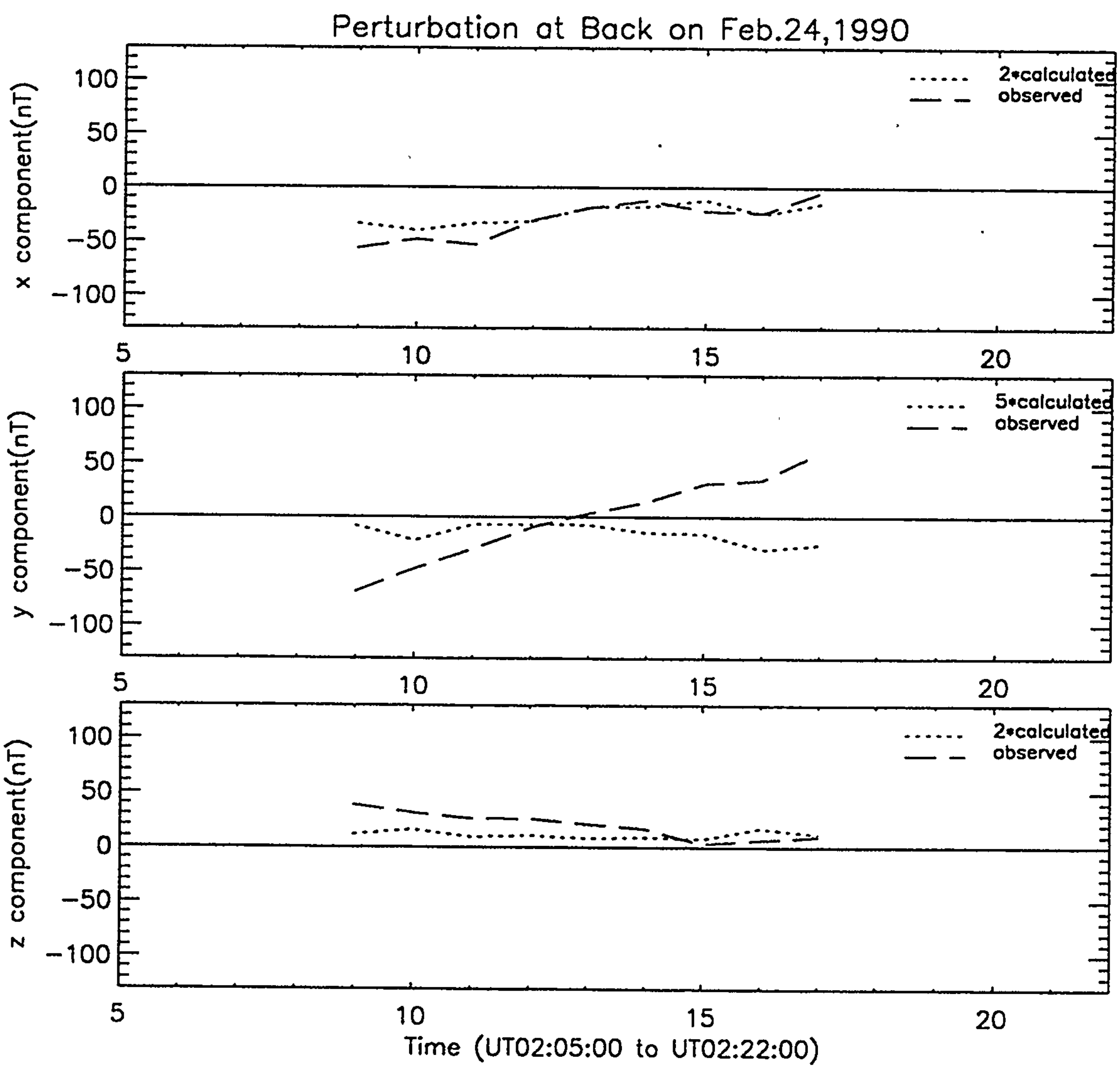


Figure 4.2.6 The time variations of the calculated and observed magnetic perturbations at Back during the time period of UT02:09:00 to UT02:17:00 on Feb.24, 1990. The dotted lines indicate the calculated perturbation and dash lines indicate the observed perturbation. There is a factor multiplying to each component of the calculated perturbation shown in the figure.

ones in the arc. The current vectors outside the arc mainly flow southwestward in the first few minutes, then the lower latitude part of it turns to be southeastward and southwestward at some times and forms two regions. The current vectors in the arc are strong and more active in this case. Since the arc is not uniform at this time, the current vectors flow around the most intensive portion of the arc counterclockwise at the time of UT04:35:00 and UT04:36:00 and change to southwestward in the following minute, then flow almost westward along the arc in the next minute but continue to change northward partially in a minute, and finally back to southwestward. The variation of the current is related to the movement of the aurora. When the most intensive portion of arc moves to the east, shown in Figure 4.3.1(a), the current vectors change their directions from northwestward to southwestward since the current flows around it counterclockwise. When the arc is more quiet and more uniform the current generally flows along the arc. From Figure 4.3.3, it is also seen that the current vectors are overhead of the Gillam station at most times. The calculated field-aligned currents from the current continuity of Eqn.(3.11), overlaid on the auroral arc contours for the wavelength of 427.8nm at each minute, are shown in Figure 4.3.4. The same colour code and the coordinate system in Figure 4.3.4 are defined as in Figure 4.2.4, so the upper colour region indicates the downward field-aligned currents and the lower colour region indicates upward field-aligned current. The EDFL latitudes and longitudes are for the north and east directions, respectively, in Figure 4.3.4. For this case the arc is more active and there is an eastward movement for the most intensive portion of the arc. The ionospheric current shown in Figure 4.3.3 flows mainly in the westward direction but it has a northward or

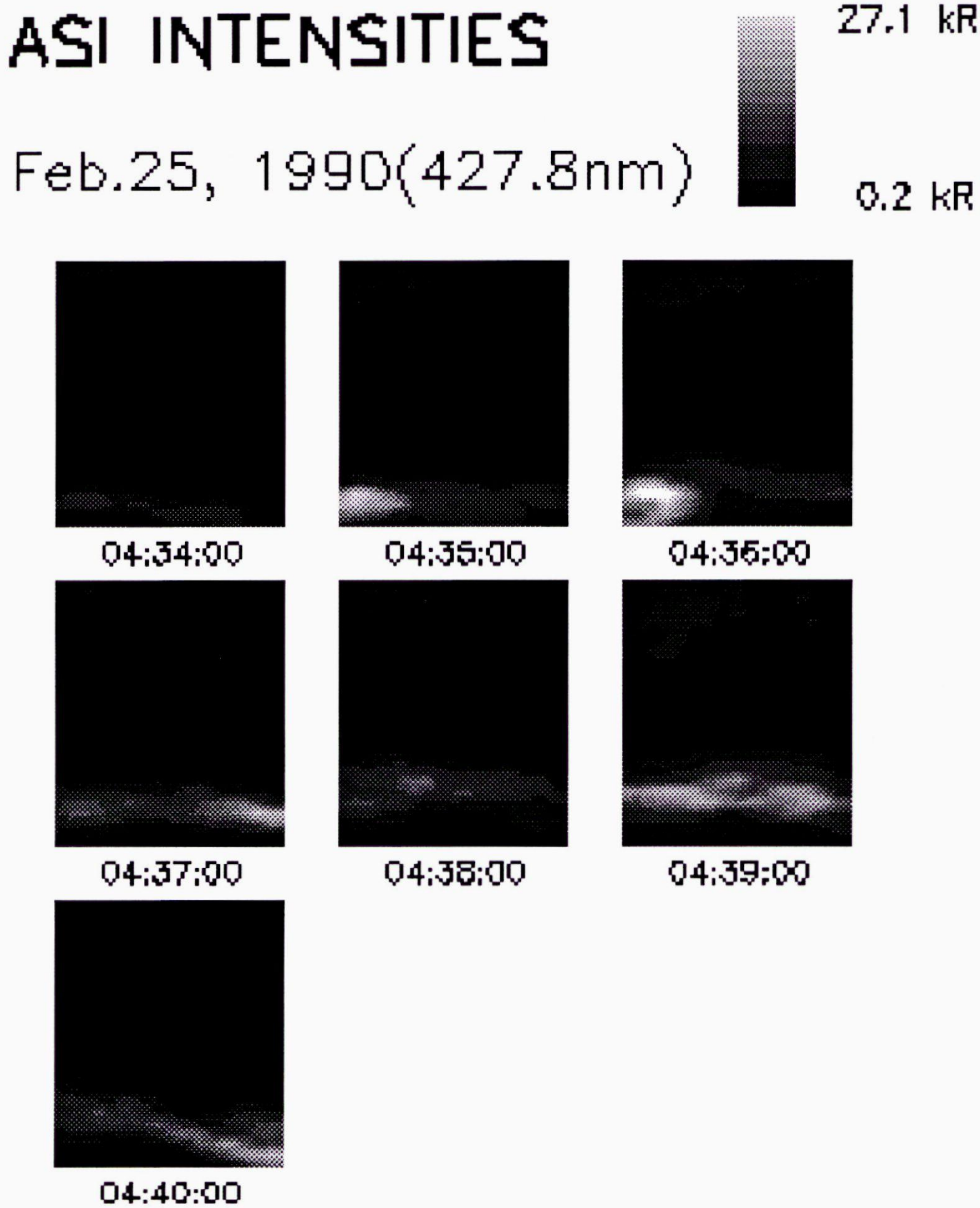


Figure 4.3.1(a) The one-minute averaged ASI images for the wavelength of 427.8nm during the time period from UT 04:34:00 to UT 04:40:00 on Feb.25, 1990. The intensities in Kilo-Rayleighs are colour coded with black indicating the minimum intensity and red indicating the maximum intensity. The coordinate system is in EDFL latitudes from $63.0^0$ to $67.8^0$ on the north and EDFL longitudes from $333.0^0$ to $340.5^0$ on the east.

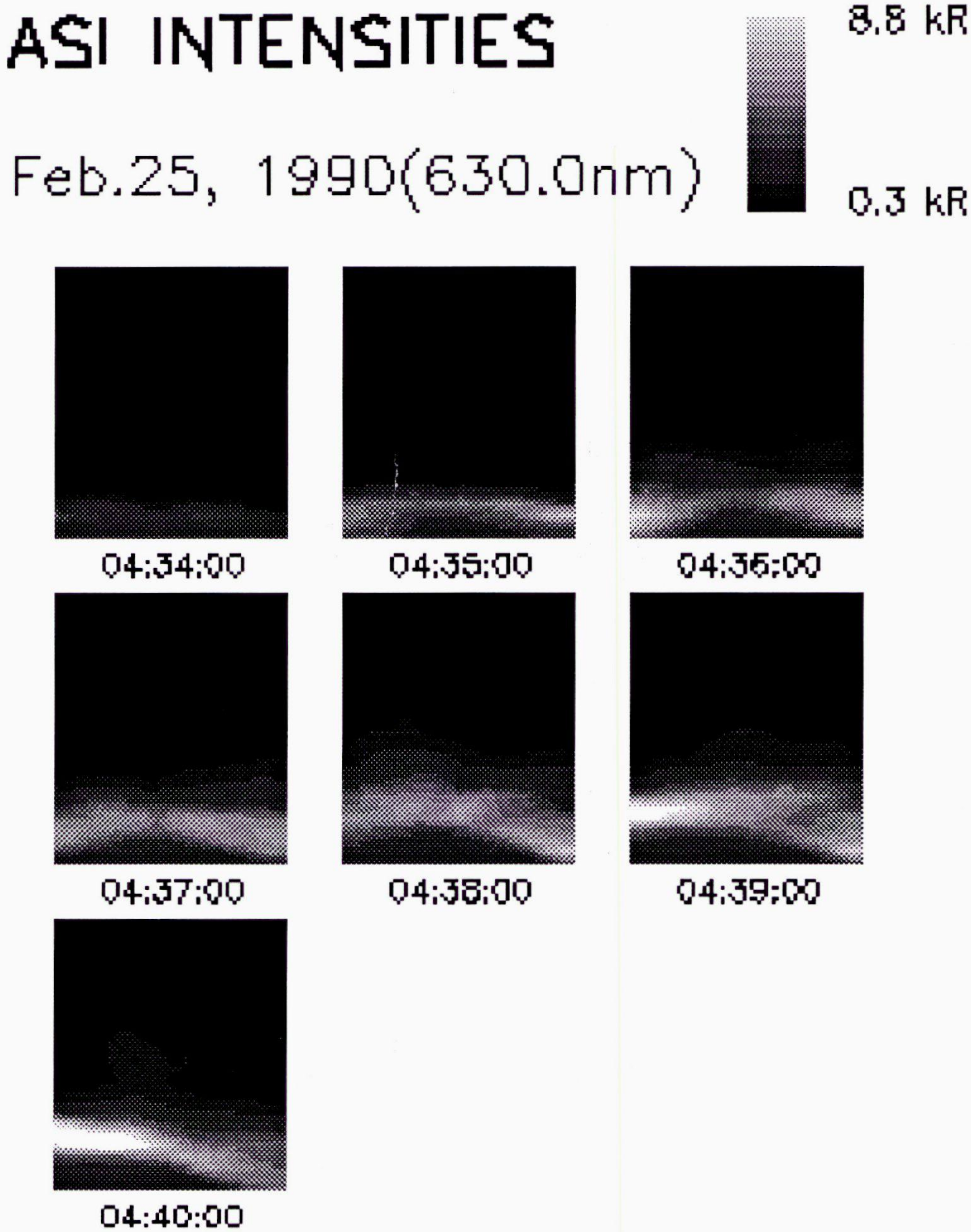


Figure 4.3.1(b) The one-minute averaged ASI images for the wavelength of 630.0nm during the time period from UT04:34:00 to UT 04:40:00 on Feb.25, 1990. The intensities in Kilo-Rayleighs are colour coded with black indicating the minimum intensity and red indicating the maximum intensity. The coordinate system is in EDFL latitudes from $63.0^0$ to $67.8^0$ on the north and EDFL longitudes from $333.0^0$ to $340.5^0$ on the east.

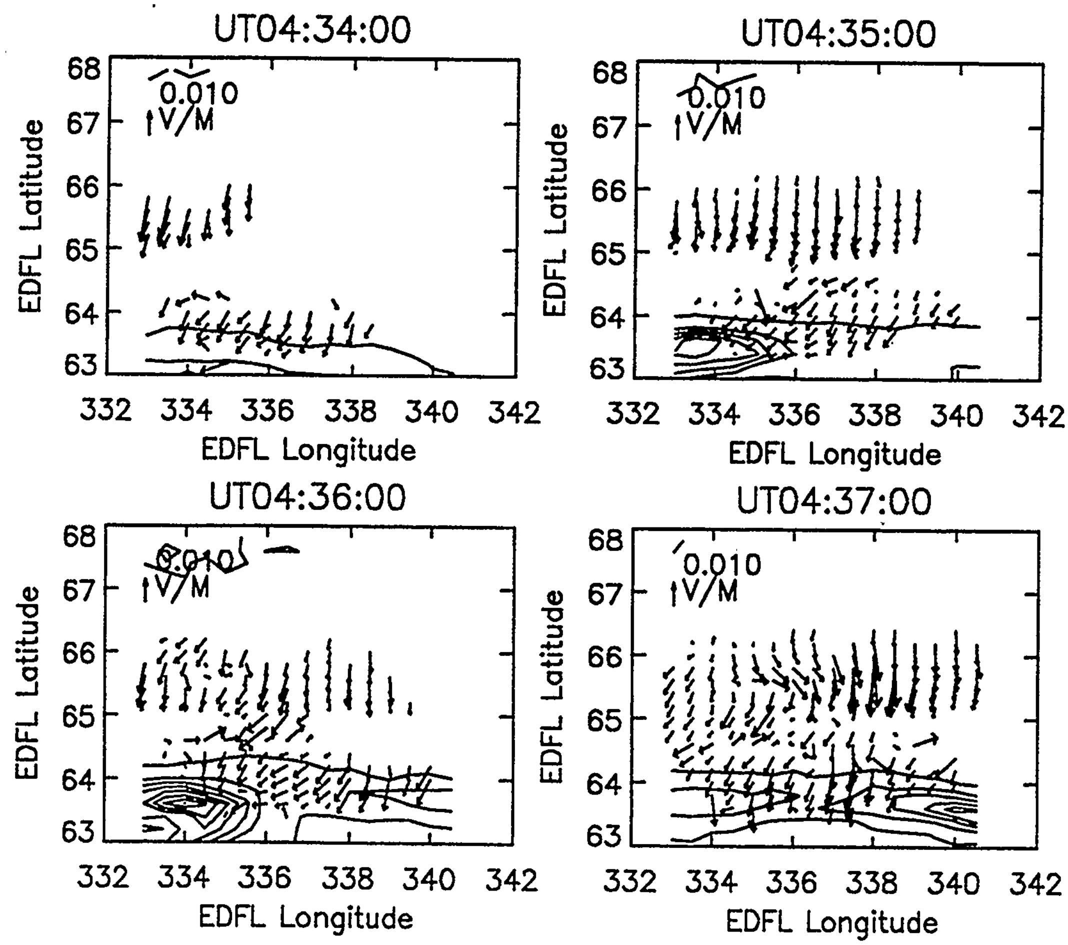


Figure 4.3.2(a) The electric fields, measured from the BARS, overlaid on the auroral contour during the time period of UT04:34:00 to UT04:37:00 on Feb.25, 1990. The vector length denotes the magnitudes of the electric field vectors referenced by the scale defined on the top. The arc contours start from 2 kR and increase by steps of 4 kR.

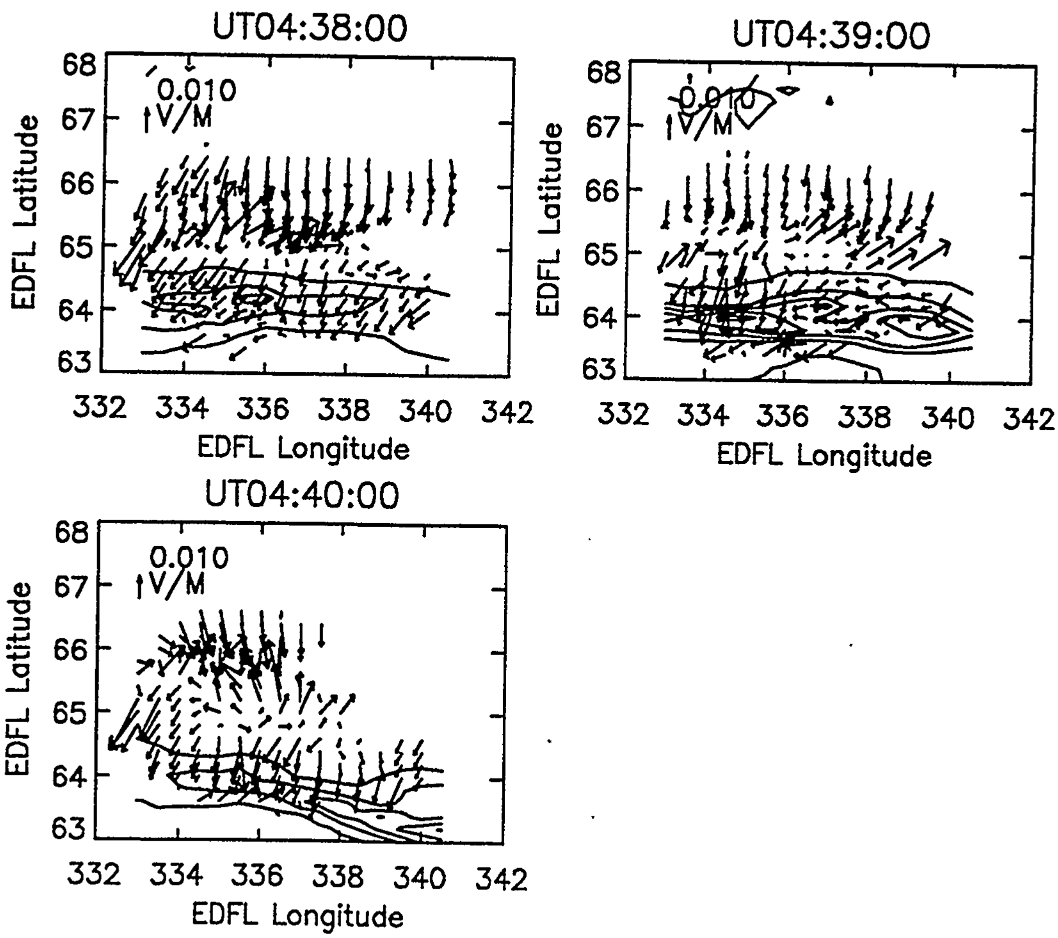


Figure 4.3.2(b) The electric fields, measured from the BARS, overlaid on the auroral contour during the time period of UT04:38:00 to UT04:40:00 on Feb.25, 1990. The vector length denotes the magnitudes of the electric field vectors referenced by the scale defined on the top. The arc contours start from 2 kR and increase by steps of 4 kR.

southward component due to the location of the most intensive portion of the arc. For this case the upward and downward field-aligned currents are mainly confined to the arc region. In the first three minutes there is a northward component of the ionospheric current around the most intensive portion of the arc on the southwest corner of the arc, so the upward field-aligned current locates at the northwest side and downward field-aligned current on the southeast side around that region. When this most intensive portion of the arc moved to the southeast corner in the following minute, the upward current changed to the southwest side since there is a southward component of the ionospheric current around that area. In the following two minutes, when the ionospheric current flowed in the northwestward direction, the upward field-aligned current returned to the northwest side and switched back to the southwest side in the last minute. The upward and downward field-aligned currents shown in Figure 4.3.4 and the ionospheric currents shown in Figure 4.3.3 consist of a three-dimensional current system in the BARS field of view in the ionosphere and satisfy the current continuity. The densities of the field-aligned currents for this case are of the order of $10^{-5}$ A/m$^2$.

### 4.3.2 Comparison of the Perturbations at Gillam Station

The time variations of the perturbations from the calculation and the observation at the Gillam station are shown in Figure 4.3.5. The x, y and z components of the computed perturbation were multiplied by 2.5, 1 and 8, respectively. In Figure 4.3.5, the x component and z component from the calculation match very well with the observation, respectively. The calculated y component is in very good agreement with the observation in spite of the appearance of a one-minute time delay.

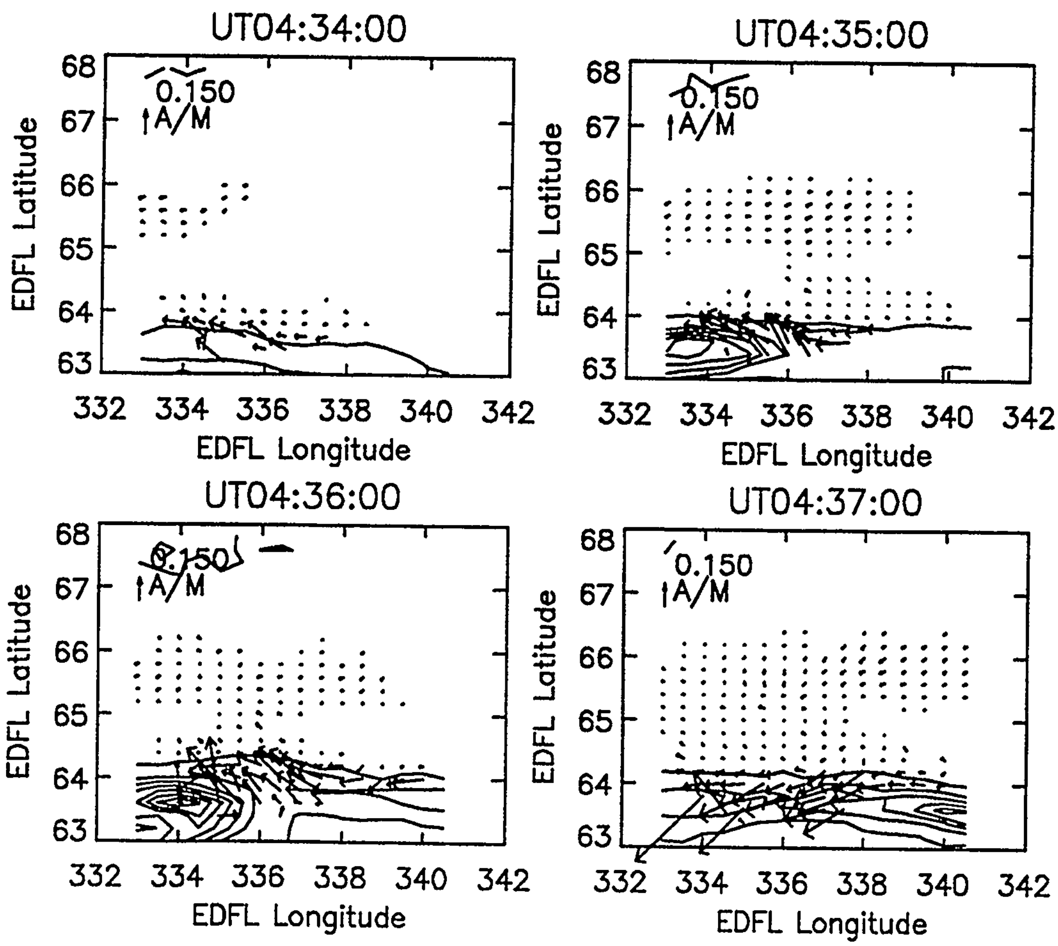


Figure 4.3.3(a) The calculated horizontal ionospheric electric current vectors, overlaid on the auroral contour during the time period of UT04:34:00 to UT04:37:00 on Feb.25, 1990. The vector length denotes the magnitudes of the current referenced by the scale defined on the top. The arc contours start from 2 kR and increase by steps of 4 kR.

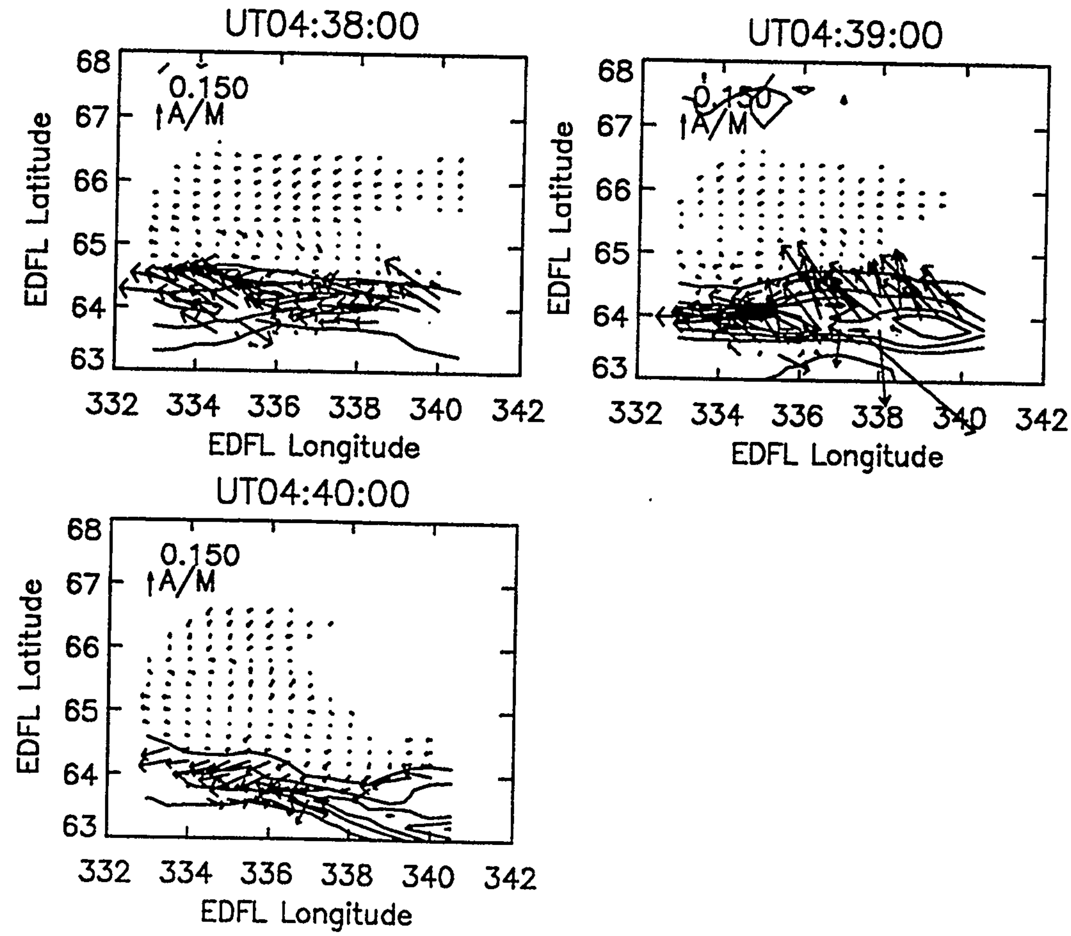


Figure 4.3.3(b) The calculated horizontal ionospheric electric current vectors, overlaid on the auroral contour during the time period of UT04:38:00 to UT04:40:00 on Feb.25, 1990. The vector length denotes the magnitudes of the current referenced by the scale defined on the top. The arc contours start from 2 kR and increase by steps of 4 kR.

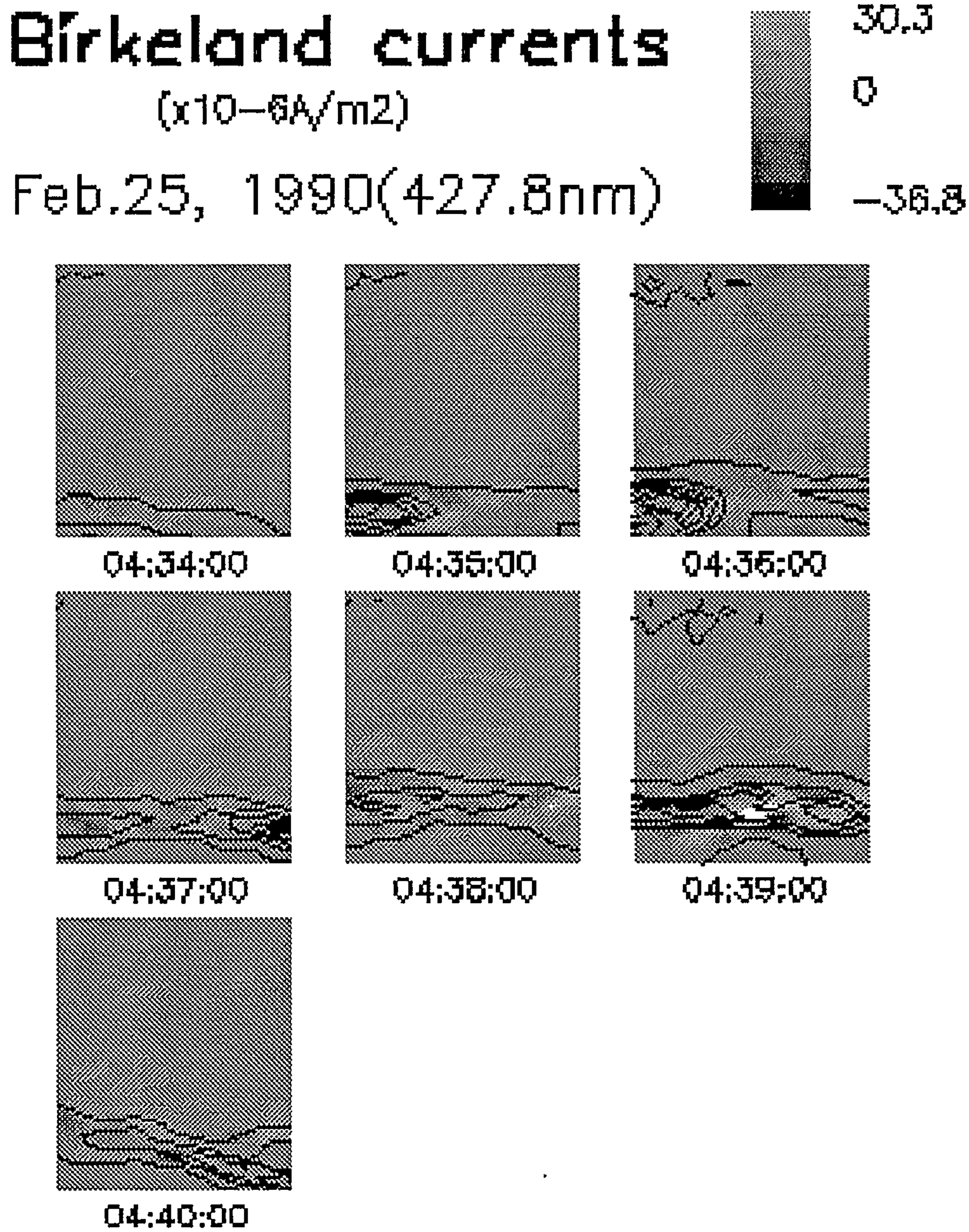


Figure 4.3.4 The calculated field-aligned currents overlaid on the auroral contour of the wavelength of 427.8nm during the time period from UT 04:34:00 to UT 04:40:00 on Feb.25, 1990. The densities in $\mu A/m^2$ are colour coded and the colour labelled zero divides the colour region to two region, with top colours indicating downward field-aligned currents and bottom colours indicating upward field-aligned currents. The coordinate system is in EDFL latitudes from $63.0^0$ to $67.8^0$ on the north and EDFL longitudes from $333.0^0$ to $340.5^0$ on the east.

### 4.3.3 Comparison of the Perturbations at Back Station

Figure 4.3.6. shows the time variations of the calculated and observed perturbations at Back station. The multiplying factors for the x, y and z components of the computed perturbation are 1, 2 and 1 , respectively. For the x component, its time variation from the calculation follows that of the observation. The calculated y component does not differ much from the observation. However, the z components do not agree. For this case the calculated ionospheric current vectors and field-aligned currents are about overhead Gillam, so the calculated perturbation at Gillam agrees with the observation better than that at Back.

## 4.4 March 21, 1990

The $k_p$ index sum for this day is 46. The one-minute averaged ASI images during the time period from UT03:39:00 to UT03:48:00 for the two wavelengths of 427.8nm and 630.0nm on this day are shown in Figure 4.4.1 (a) and (b), respectively. Figure 4.4.1 shows the intensities of the auroral emissions for the wavelengths of 427.8nm and 630.0nm and the intensities are colour coded as in Figure 4.2.1(a) and (b). The coordinate system in Figure 4.4.1 is also the same as the one in Figure 4.2.1. The arc pattern for the wavelength of 630.0nm is similar to that for the wavelength of 427.8nm, but is brighter. The intensities for both of the wavelengths in the arc are not uniform. The highest intensity is about 2 kR and 9 kR for the wavelengths of 427.8nm and 630.0nm, respectively, so the auroral emission for the wavelength of 427.8nm is much weaker than that for the wavelength of 630.0nm. The electric fields, deduced from

BARS-measured electron drift velocities, overlaid on the auroral arc contours for the wavelength of 427.8nm at each minute are shown in Figure 4.4.2, where the auroral arc contours start from 1 kR and increase every 1 kR. Since the auroral intensities in the middle portion of the arc are weaker than at the sides, the contour of the arc is broken into two parts, as seen in Figure 4.4.2. The electric field vectors are mostly at the north side of the arc, some are in the arc and very few are south of the arc. For this case the arc as a boundary divides the electric field vectors into two regions. The electric field vectors on the north side region point to the arc in the southwestward direction and those on the south side region point to the arc in the northeastward direction. When the arc gets weaker, the north side region becomes dominant. Figure 4.4.2 also shows the relative location of the arc and the electric field vectors at each moment.

### 4.4.1 The Calculated Ionospheric (horizontal) Current Vectors and Field-aligned Currents in the BARS Field of View

Figure 4.4.3 shows the calculated ionospheric (horizontal) current vectors at each minute of the time period obtained from the same procedure as that in Figure 4.2.3. Due to the fact that the intensities at the wavelength of 427.8nm are much smaller than at the wavelength of 630.0nm in this case, the calculated Pedersen and Hall conductivities in the arc are about 5 mhos and are therefore not larger than those outside the arc. The oncoming downward electrons to the auroral region were very soft and precipitated mainly in the relatively high altitude region. Therefore it is not the same as before in that the calculated ionospheric current vectors are present not only in the arc but also outside the arc. The current vectors outside the arc flow around the arc counterclockwise and

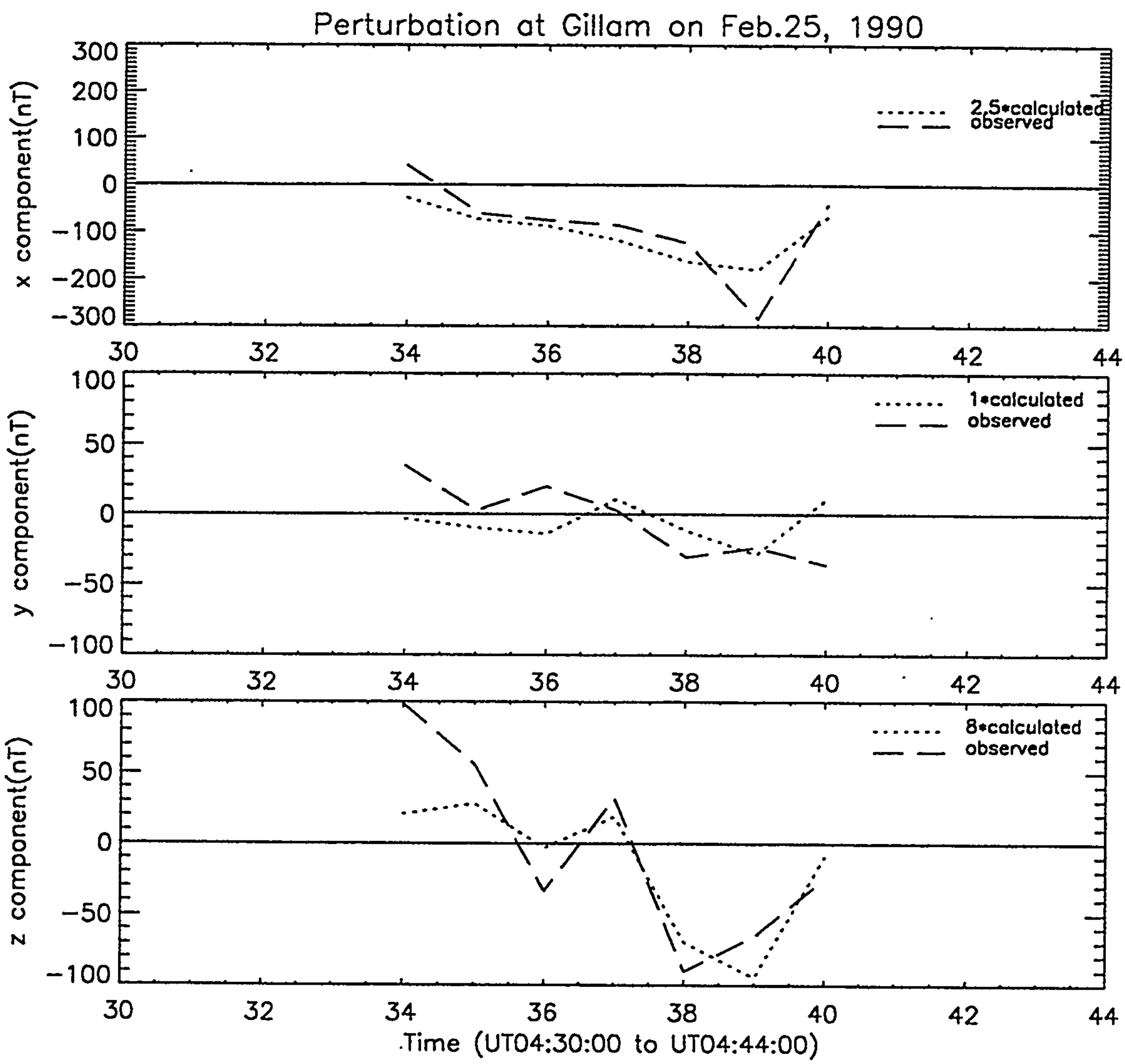


Figure 4.3.5 The time variations of the calculated and observed magnetic perturbations at Gillam during the time period of UT04:34:00 to UT04:40:00 on Feb.25, 1990. The dotted lines indicate the calculated perturbation and dash lines indicate the observed perturbation. There is a factor multiplying to each component of the calculated perturbation shown in the figure.

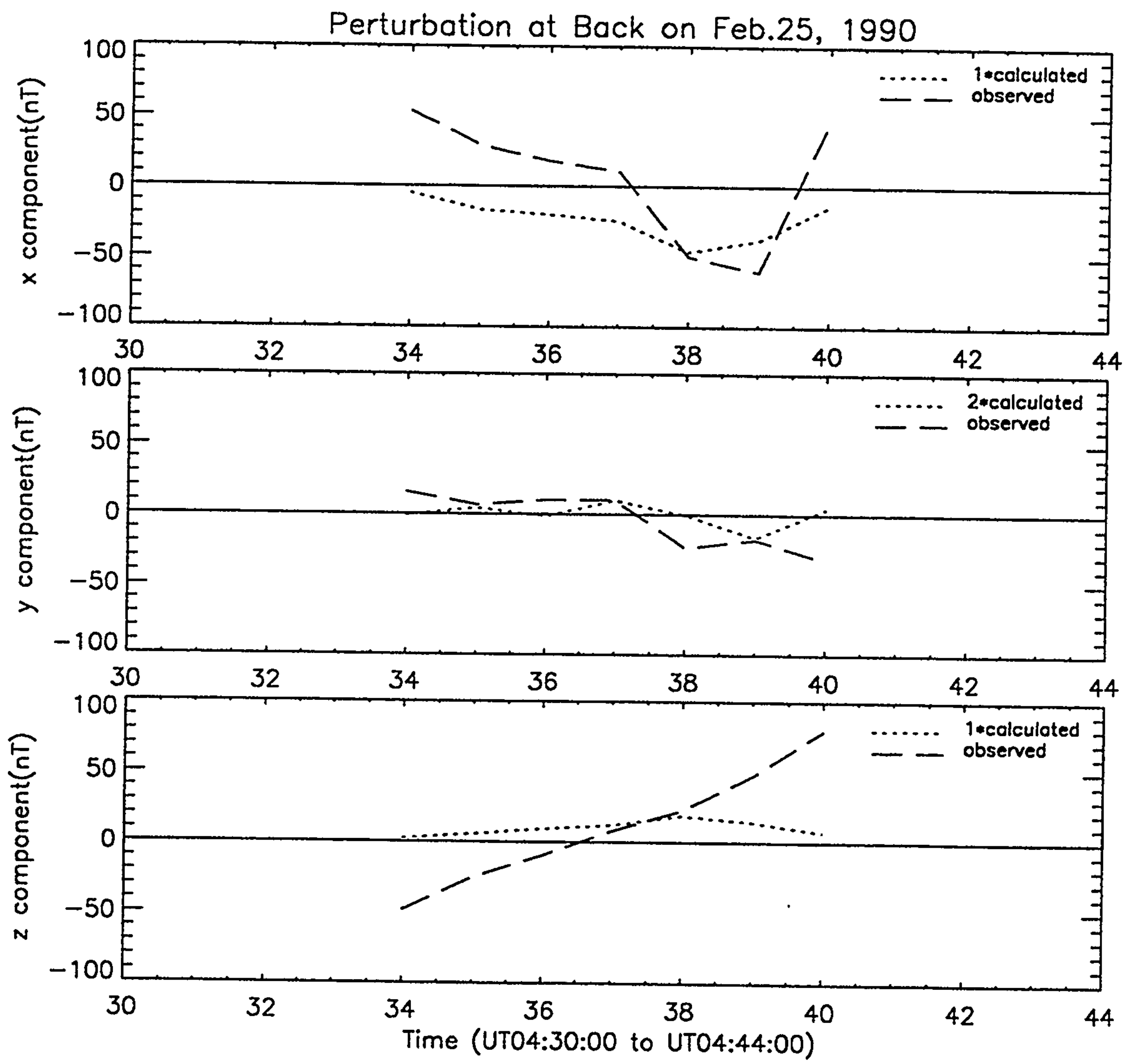


Figure 4.3.6 The time variations of the calculated and observed magnetic perturbations at Back during the time period of UT04:34:00 to UT04:40:00 on Feb.25, 1990. The dotted lines indicate the calculated perturbation and dash lines indicate the observed perturbation. There is a factor multiplying to each component of the calculated perturbation shown in the figure.

those in the arc tend to flow out of the arc in the northward direction. Figure 4.4.3 also shows the relative location of the ionospheric current and the auroral arc. The horizontal electric current vectors are located at the region between Gillam station and Back station, but are closer to the Back station. The ionospheric current intensity for this case is about ten times smaller than that for the former two cases. The calculated field-aligned currents from the current continuity of Eqn.(3.11), overlaid on the auroral arc contours for the wavelength of 427.8nm at each minute, are shown in Figure 4.4.4. As before the upper and lower regions separated by the colour labelled zero indicate the downward and upward field-aligned currents, respectively. In Figure 4.4.4, the north direction denotes the EDFL latitudes and the east direction indicates the EDFL longitudes. For this case the arc is very weak but more active. The contour of the arc is broken into two parts since the intensities in the region between the two parts are even weaker. The distribution of the field-aligned currents is divided into two regions, inside the arc and outside the arc. The field-aligned current outside the arc is relatively small and mainly downward. For the stronger arc the upward field-aligned current inside the arc is on the north side since there is a northward component of the ionospheric current shown in Figure 4.4.3. When the arc gets weaker the ionospheric current tends to flow along the same direction as the one outside the arc shown in Figure 4.4.3 and the upward field-aligned current appears on the west side and downward current on the east side. The densities of the field-aligned currents in this case are about ten times smaller than those for the former two cases. The upward and downward field-aligned currents and the ionospheric current consist of a three-dimensional current system in the BARS field of view in the ionosphere

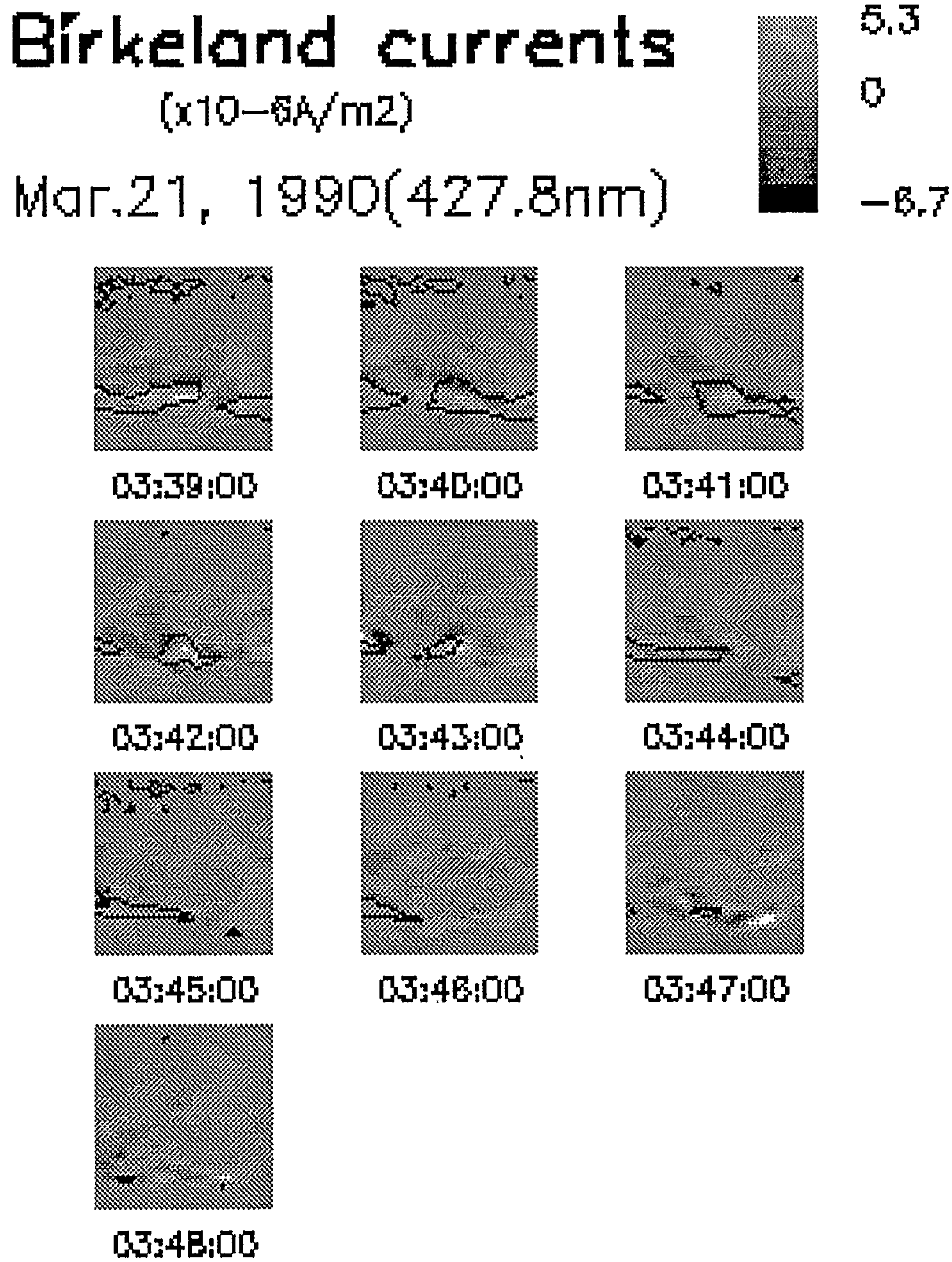


Figure 4.4.1(a) The one-minute averaged ASI images for the wavelength of 427.8nm during the time period from UT 03:39:00 to UT 03:48:00 on March 21, 1990. The intensities in Kilo-Rayleighs are colour coded with black indicating the minimum intensity and red indicating the maximum intensity. The coordinate system is in EDFL latitudes from $63.0^0$ to $67.8^0$ on the north and EDFL longitudes from $333.0^0$ to $340.5^0$ on the east.

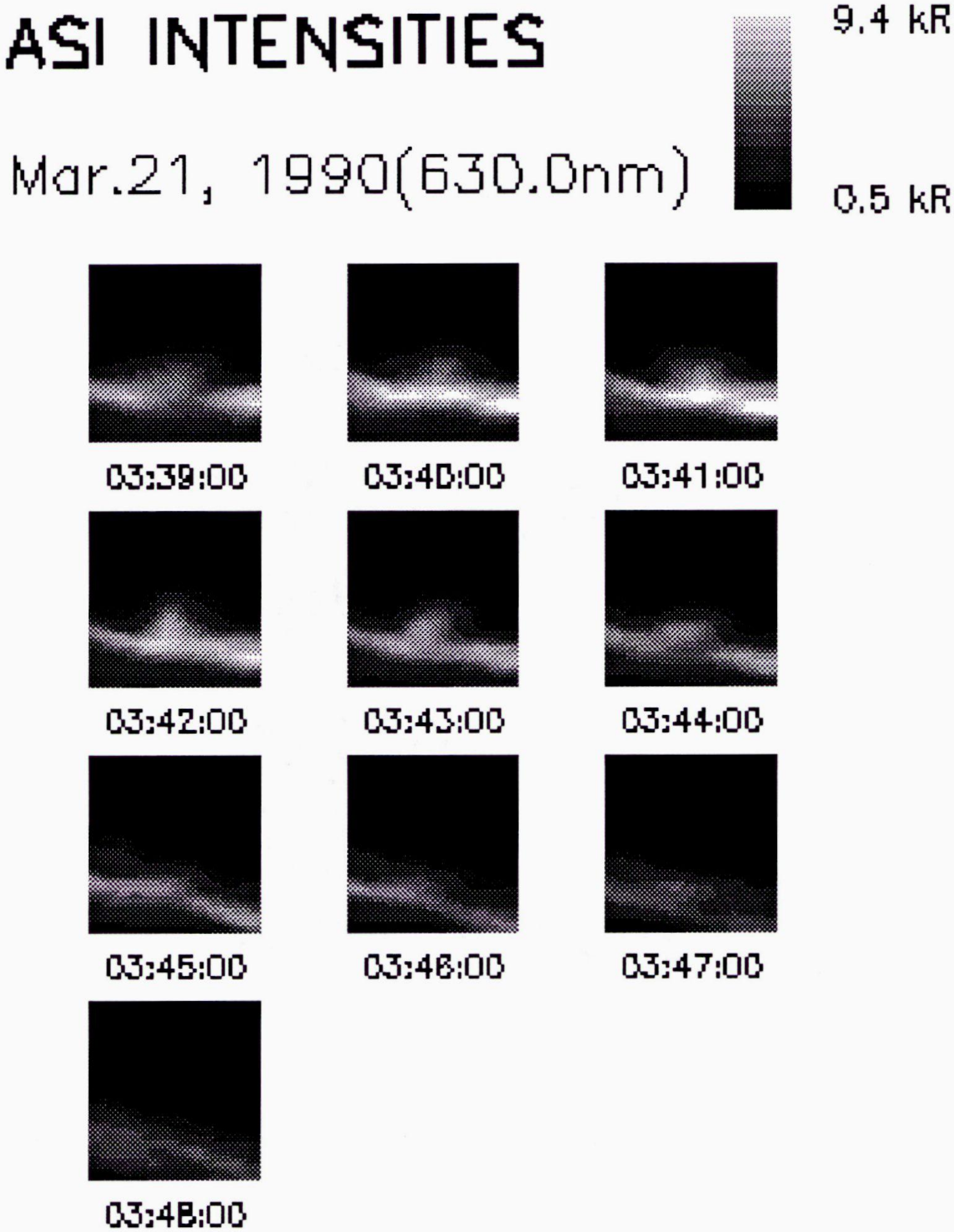


Figure 4.4.1(b) The one-minute averaged ASI images for the wavelength of 630.0nm during the time period from UT03:39:00 to UT 03:48:00 on March 21, 1990. The intensities in Kilo-Rayleighs are colour coded with black indicating the minimum intensity and red indicating the maximum intensity. The coordinate system is in EDFL latitudes from 63.0$^0$ to 67.8$^0$ on the north and EDFL longitudes from 333.0$^0$ to 340.5$^0$ on the east.

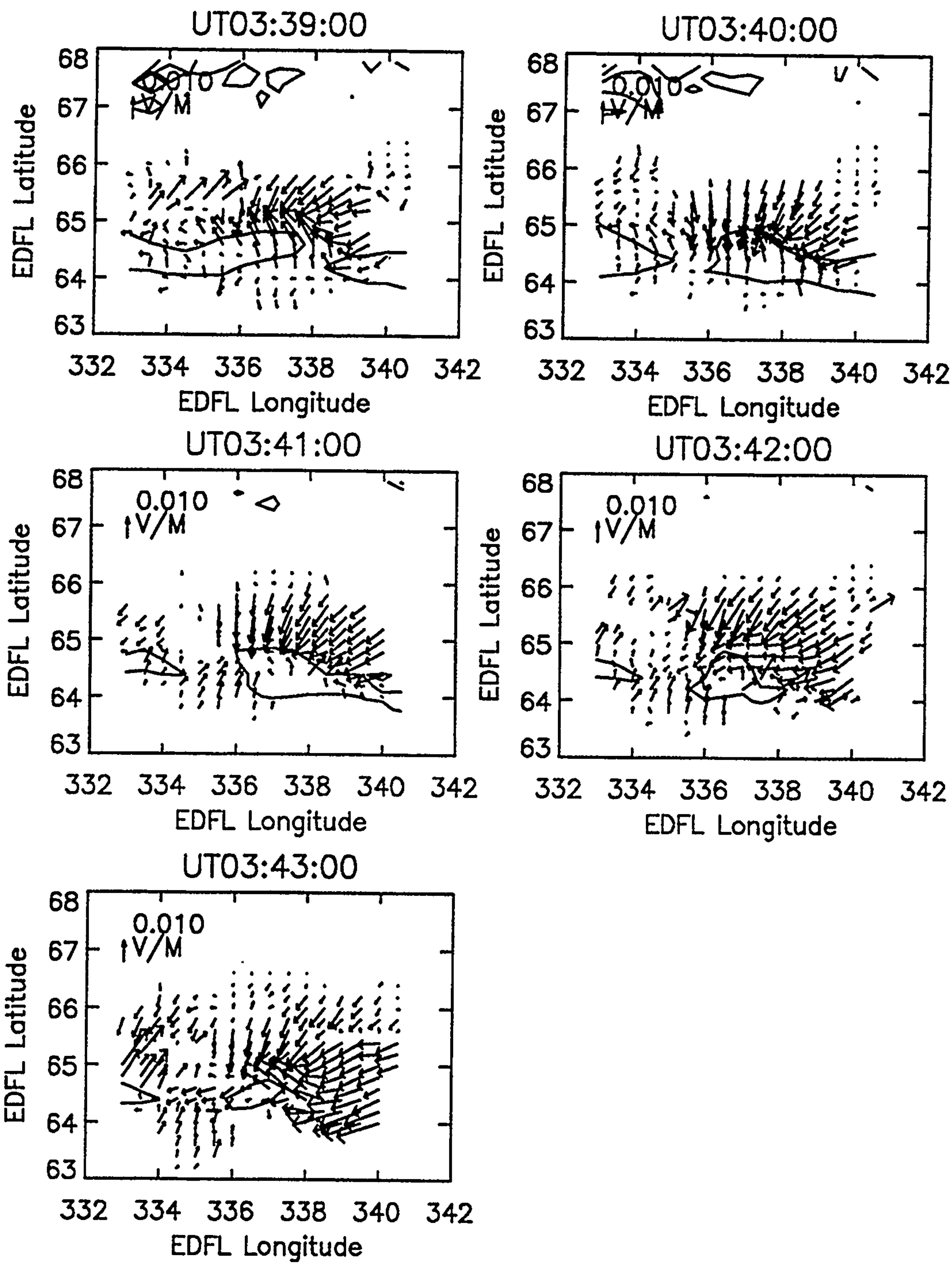


Figure 4.4.2(a) The electric fields, measured from the BARS, overlaid on the auroral contour during the time period of UT03:39:00 to UT03:43:00 on March 21, 1990. The vector length denotes the magnitudes of the electric field vectors referenced by the scale defined on the top. The arc contours start from 1 kR and increase by step of 1 kR.

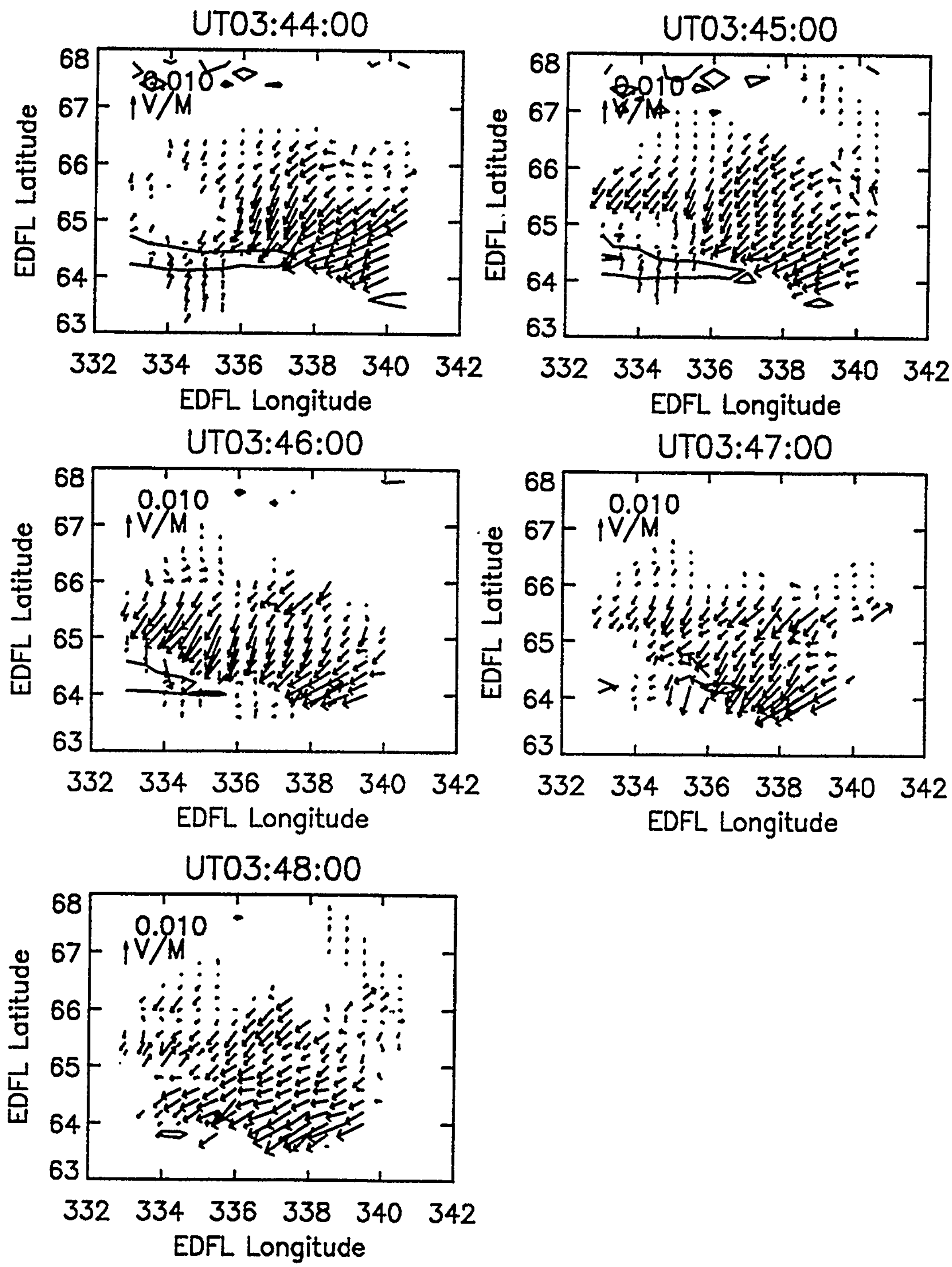


Figure 4.4.2(b) The electric fields, measured from the BARS, overlaid on the auroral contour during the time period of UT03:44:00 to UT03:48:00 on March 21, 1990. The vector length denotes the magnitudes of the electric field vectors referenced by the scale defined on the top. The arc contours start from 1 kR and increase by step of 1 kR.

and satisfy the current continuity.

### 4.4.2 Comparison of the Perturbations at Gillam Station

The calculated and observed perturbations at Gillam station during this time period on this day are shown in Figure 4.4.5. Each component of the calculated perturbation is multiplied by 14, 3 and 2, respectively. The variation of the calculated x component in this case is then very close to what was observed. The y component varied with time in a similar manner as the observation. The calculated z component is different from the observation and shows no change within the time period.

### 4.4.3 Comparison of the Perturbations at Back Station

Figure 4.4.6 shows the time variations of the calculated and observed perturbation at Back station during the same period as above from UT03:39:00 to UT03:48:00. The factors applied to each component of the calculated perturbation at Back is 7, 5 and 10, respectively. The calculated perturbation at Back agrees very well with the observation, since the current system in this case is located near the Back station.

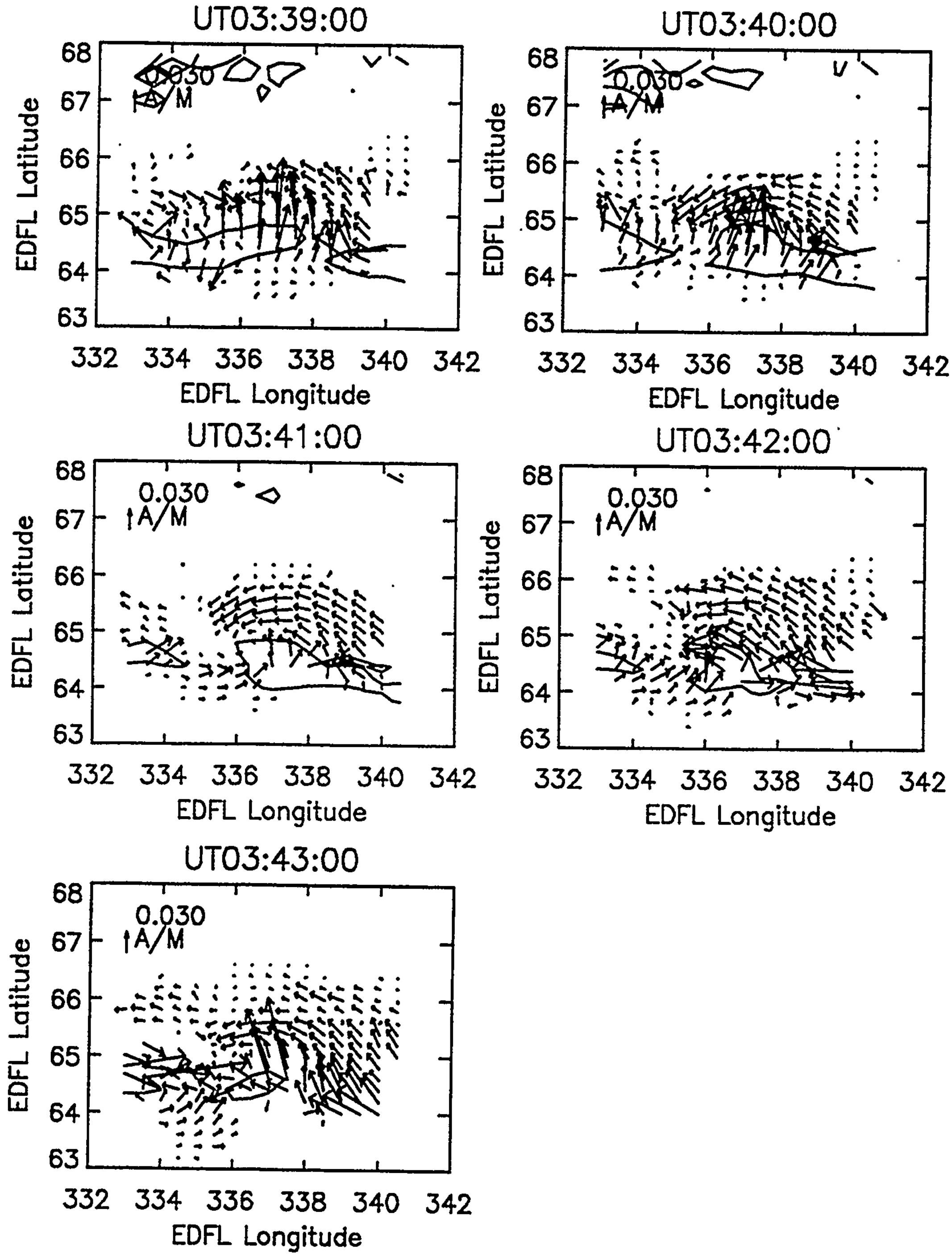


Figure 4.4.3(a) The calculated horizontal ionospheric electric current vectors, overlaid on the auroral contour during the time period of UT03:39:00 to UT03:43:00 on March 21, 1990. The vector length denotes the magnitudes of the current referenced by the scale defined on the top. The arc contours start from 1 kR and increase by step of 1 kR.

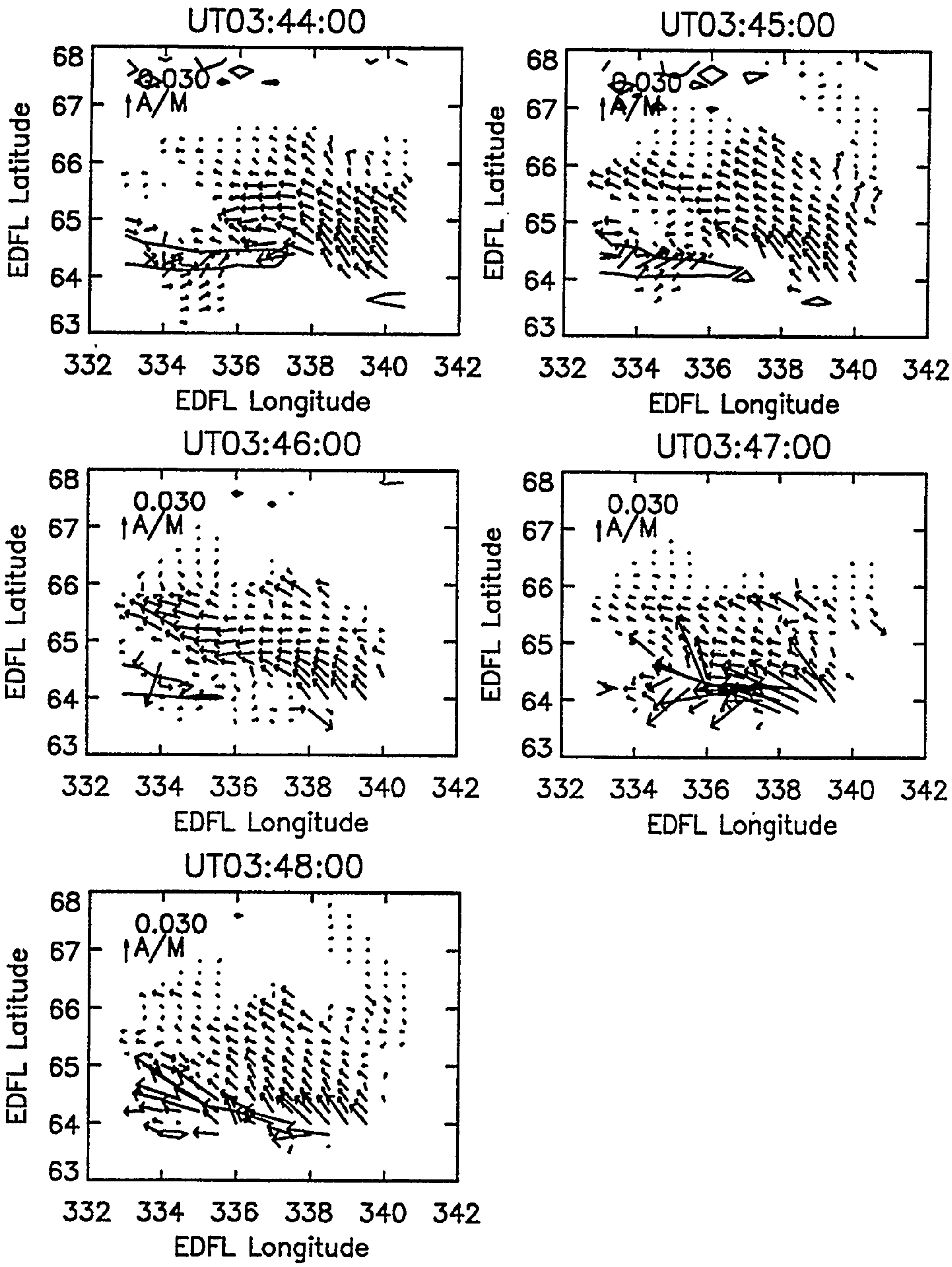


Figure 4.4.3(b) The calculated horizontal ionospheric electric current vectors, overlaid on the auroral contour during the time period of UT03:44:00 to UT03:48:00 on March 21, 1990. The vector length denotes the magnitudes of the current referenced by the scale defined on the top. The arc contours start from 1 kR and increase by step of 1 kR.

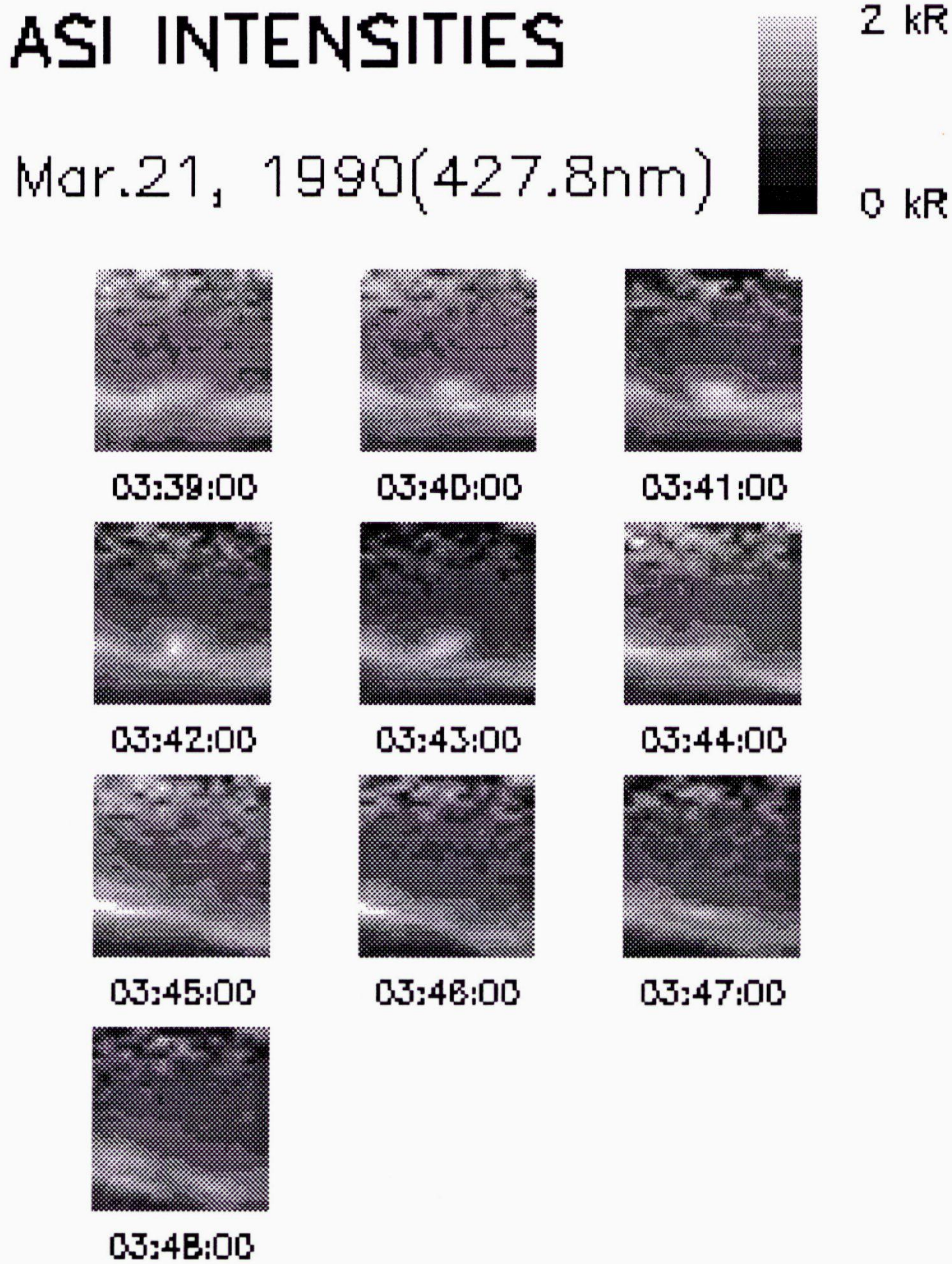


Figure 4.4.4 The calculated field-aligned currents overlaid on the auroral contour of the wavelength of 427.8nm during the time period from UT 03:39:00 to UT 03:48:00 on March 21, 1990. The densities in $\mu A/m^2$ are colour coded and the colour labelled zero divides the colour region to two region, with top colours indicating downward field-aligned currents and bottom colours indicating upward field-aligned currents. The coordinate system is in EDFL latitudes from $63.0^0$ to $67.8^0$ on the north and EDFL longitudes from $333.0^0$ to $340.5^0$ on the east.

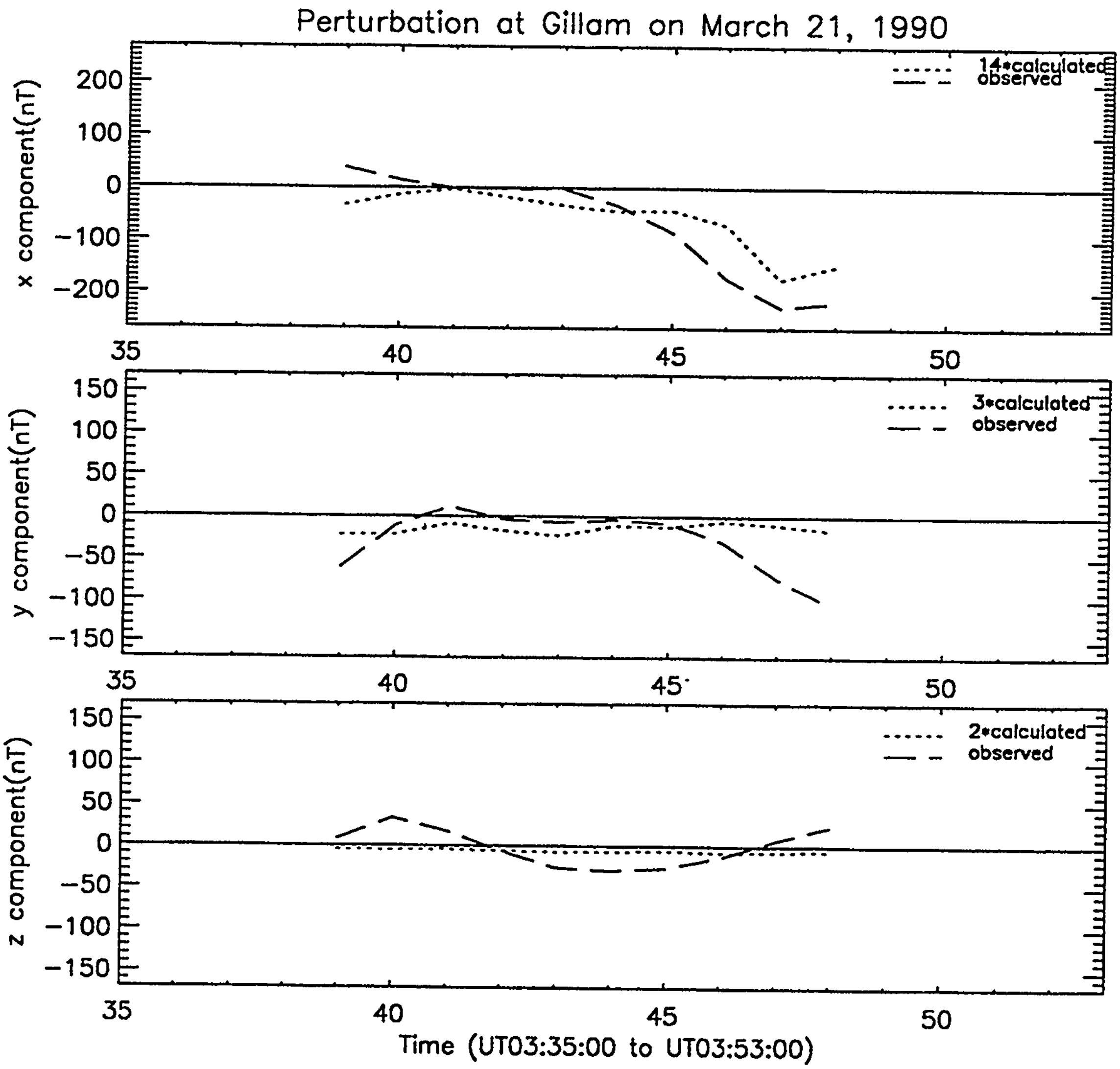


Figure 4.4.5 The time variations of the calculated and observed magnetic perturbations at Gillam during the time period of UT03:39:00 to UT03:48:00 on March 21, 1990. The dotted lines indicate the calculated perturbation and dash lines indicate the observed perturbation. There is a factor multiplying to each component of the calculated perturbation shown in the figure.

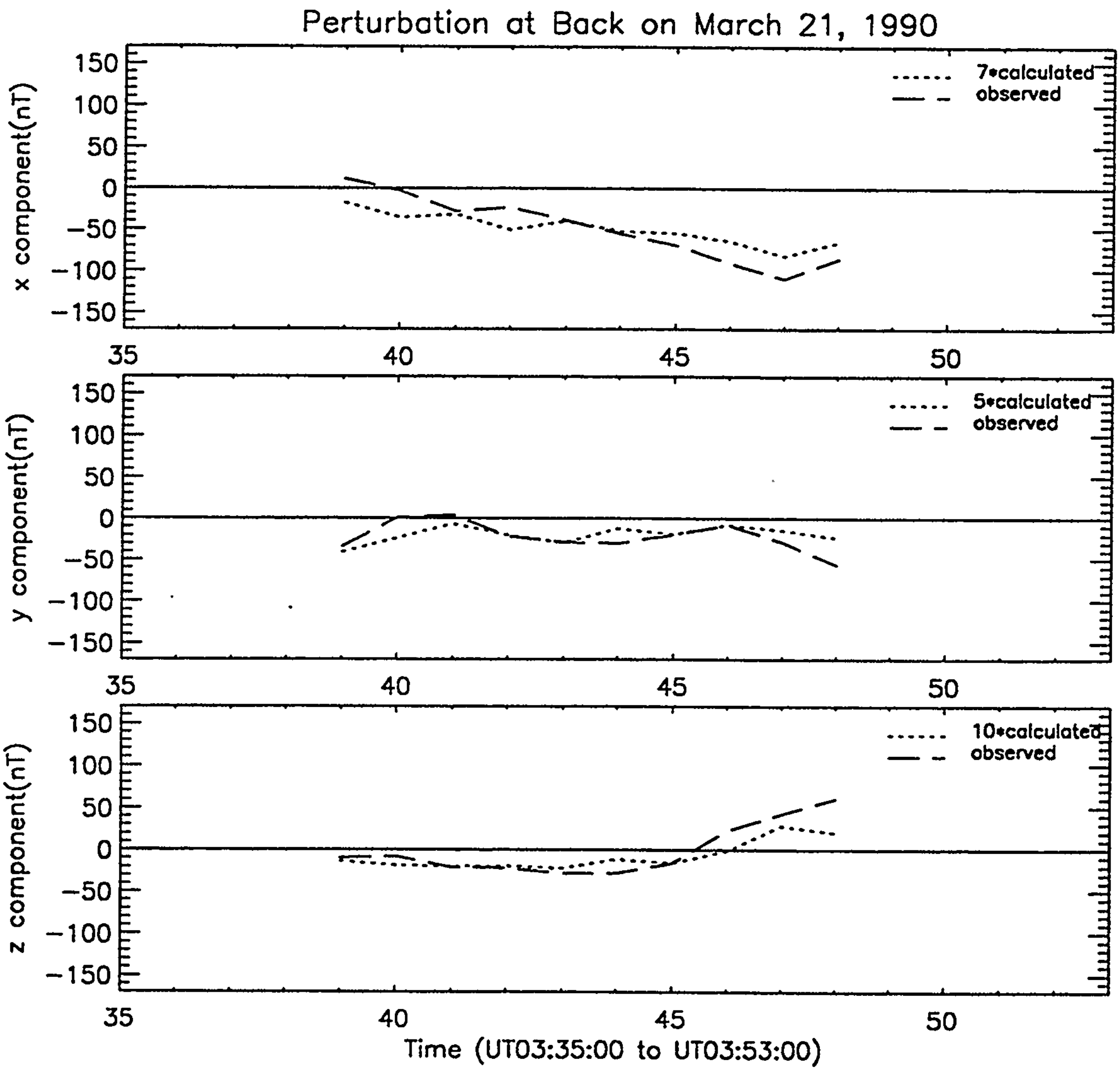


Figure 4.4.6 The time variations of the calculated and observed magnetic perturbations at Back during the time period of UT03:39:00 to UT03:48:00 on March 21, 1990. The dotted lines indicate the calculated perturbation and dash lines indicate the observed perturbation. There is a factor multiplying to each component of the calculated perturbation shown in the figure.

# CHAPTER V. DISCUSSION AND SUMMARY

## 5.1 Discussion

### 5.1.1 Discussion of the results

From the three evening cases selected for analysis, the important findings are that the ionospheric (horizontal) current is confined to the region of the auroral arc when the Pedersen and Hall conductivities in the arc are significantly enhanced and the inferred three-dimensional current system in the field of view is a combination of both Boström type 1 and type 2 current systems on a small scale. For the three cases the auroral arcs were observed in the evening sector and they were more active and not uniform at certain times. The ionospheric current flowed in the westward direction along the quiet arc or counterclockwise around the most intensive portion of the arc including the spiral situation. The upward and downward field-aligned currents found from the divergence of the ionospheric current appeared in pairs and was mainly confined to the arc region. For a quiet east-west arc the downward field-aligned current was in the east side of the arc and upward field-aligned current was in the west side. For a distorted arc the downward field-aligned current was in the north side or south side of the arc depending on the location of the most intensive portion of the arc in the west side or the east side of the arc. The upward field-aligned current was on the other side. This current system is distributed over a small region within the area of 500 km $\times$ 320 km about overhead of Gillam. Such a current system was examined by converting it to the magnetic perturbation on the ground and comparing it with the observed magnetic perturbation from the MARIA. The comparison showed a very good agreement between the time variations especially when the calculated current system was about overhead of the station at which the comparison was done. However there are still some discrepancies for the calculated and observed magnetic perturbation at the other stations and the magnitudes for both of the perturbations are also different. There are several things needed to be considered. first, for all the cases the auroral arcs appear near the southern edge of the BARS field of view, so not all current vectors were recorded. The missing current vectors would affect the magnetic field at the Gillam station or other stations because of the high conductivities in this region. Second, there is a limitation of BARS measurements. Only merged data from the two radars can be used to produce electric field vectors, which means if there are no data recorded by one of these two radars no electric field vectors are on the BARS map. Fig.5.1 shows such an example for the time of UT02:15:30 on Feb.24, 1990, where the radar in Red Lake recorded data on the south-east side of the map, but no electric field vectors could be obtained. Third, the calculated ionospheric current vectors and field-aligned currents refer to a small region of the auroral oval. Fourth, the baselines used to determine the observed magnetic perturbations are difficult to choose. MARIA recorded a total perturbation on the ground caused by many current sources overhead. However the calculated perturbation is related only to the current source which could be observed within the BARS field of view of the auroral region by the ASI. In order to better compare the perturbations from the same source, the baselines must include the perturbations caused by all the other possible current sources except the current within the BARS field of view. However, such a baseline may change with time. In other words, there is no simple way to determine it. Fifth, there were no measurement uncertainties considered here. The statistical and systematical error in ASI data is supplied in Pao's thesis ( 1991). The systematical error is relatively big and is slightly different for different wavelengths. It is estimated to be about 17%. The error in BARS measurements is very difficult to determine. Therefore the uncertainty in the calculated current system is hard to estimate. Sixth, there exist uncertainties in the empirical models which are used to estimate height-integrated Pedersen and Hall conductivities in auroral arcs from ASI. The equations (3.3) and (3.4) from Robinson and Vondrak et al. are based on the assumption of a Maxwellian energy distribution for precipitating electrons. A non-Maxwellian energy distribution may give a different result, but their calculation shows that the Maxwellian relations are valid for most common auroral electron spectra, and furthermore most auroral electron energy distributions are nearly Maxwellian in shape (Robinson and Vondrak et al., 1987). They estimated the uncertainty in the use of these equations to be about 20%.

Due to the reasons given above, it is probable that the determination of the baselines is one of the reasons that causes the time variations of some components of the calculated perturbations to differ from those of the observed perturbations. For the situation in which the calculated current did not locate at the region above the station where the perturbation was calculated, there might exist other current sources close to that station which affected the perturbation there strongly. For the first case of Feb.24,

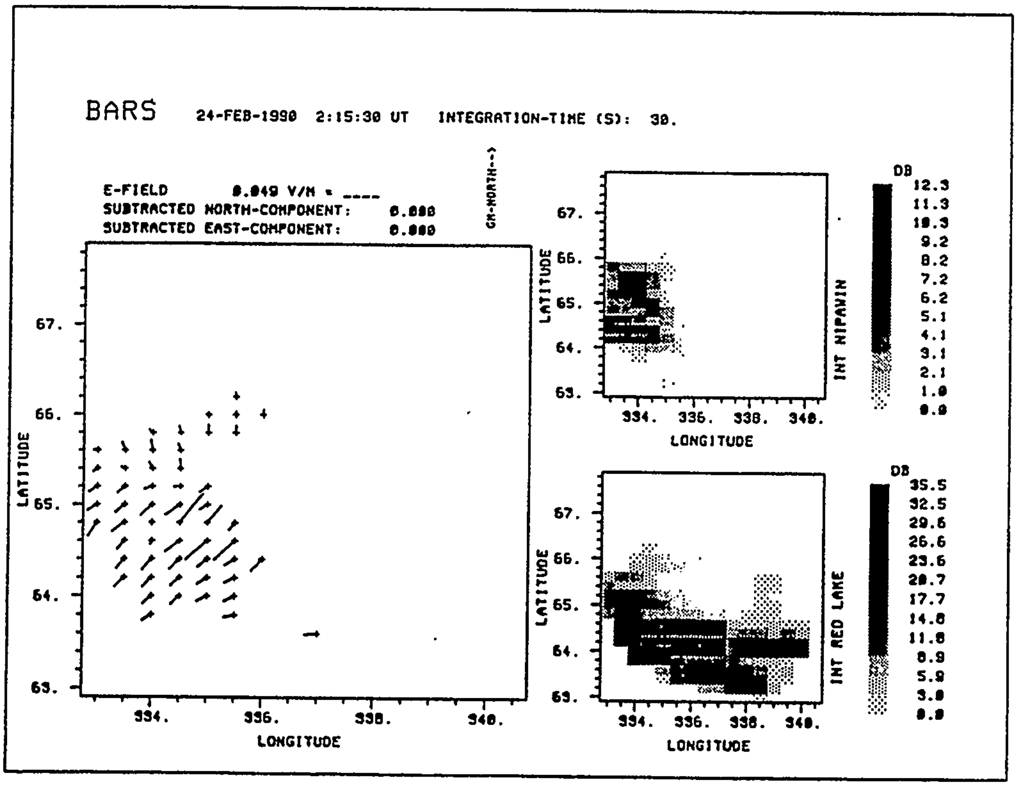


Figure 5.1 An example of radar measurement at 02:15:30 UT on Feb.24, 1990 which shows that no electric field was recorded on the south-east side of the field, since no echoes were obtained from the radar located at Nipawin.

1990 in Figure 4.2.6, the discrepancy that appeared on the y component at the Back station may be due to the baseline chosen there. It seems likely that another N-S current source existed somewhere close to Back which affected the y component of the observed perturbation there. For the case on Feb.25 of 1990 in Figure 4.3.5 and Figure 4.3.6, the calculated y component has a one minute delay at Gillam and the calculated z component at Back is different from the observations. For the case of March 21, 1990 shown in Figure 4.4.5 and Figure 4.4.6, the big discrepancy appears only in the calculated z component at Gillam.

What causes the differences between the calculated and observed perturbations is probably a serious problem. At the Gillam station, the factor used to magnify the calculated perturbation is small for the x and y components of the perturbation, and very big for the z component in the first two cases. The small factors may not be very difficult to explain, but the big factors seem very hard. In order to find the causes, several possibilities were considered. First, the chosen background intensity, when using ASI data to calculate conductivities, was thought to be a possible problem, but a calculation showed that a 50% change of this value did not affect the conductivities significantly. So, it should not be the reason. Second, the calculated conductivities from ASI data and the electric fields estimated from BARS measurements in the arc region are consistent with values in the literature (Brekke, 1974). However, the chosen background values for the Pedersen and Hall conductivities could be too small and so could the resulting current vectors outside the auroral arc. The reason is that the height-integrated Pedersen and Hall conductivities for the background caused only by the solar radiation and cosmic rays were assumed and the effect of the electron precipitation on that region was not considered. If the Pedersen and Hall conductivities on the background should increase to 5 and 10 mhos from 1 and 2 mhos, respectively, the calculation shows that the x and y components of the perturbation approximately remain the same but the z component will increase a factor of 2. For the background Pedersen and Hall conductivities of 10 mhos and 20 mhos, respectively, the x and y components of the perturbation increase by a factor of 2 and the z component increases by a factor of 4. Under this circumstance, the multipliers to the x and y components of the perturbation may easily be explained, but the factor for the z component is still not big enough. Third, the height of the ionospheric current in the auroral region was chosen as 110 km. If this value should be reduced to 90 km, the z component of the perturbation would increase by approximately a factor of 1.5 times. The reduced height does not change the x and y components very much. Fourth, the calculated ionospheric electric current in this study is confined to a small region of the auroral oval. Supposing the current should be continuous in the auroral oval, this can increase each component of the perturbation by a factor of two.

In summary, the above estimates can readily account for the x and y multipliers, but can not at the same time account for the large z component multiplier. For the perturbation at Back station in the third case, the situation is different. The multipliers for all the three components in this case are big. The auroral arc is very weak and the conductivities in and outside the arc are almost the same. If the conductivities on the background should be increased, the conductivities in the arc should also be increased so that the resulting perturbation would increase significantly. For the background Pedersen and Hall conductivities of 5 and 10 mhos, respectively, the perturbation at Back station increases approximately by a factor of 4 for the x and y components and 5 for the z component. For the background Pedersen and Hall conductivities of 10 and 20 mhos, respectively, the perturbation increases by a factor of 8 for the x and y components and 10 for the z component. Using these larger conductivities, the z component of the perturbation is very close to the observation but the x and y components are a little bit higher, which is consistent with the first two cases. For this case, the continuous ionospheric current in the auroral region beyond the field of view could increase the perturbation by a factor of 2 which is insufficient to account for multipliers of the three components.

### 5.1.2 Comparison with Earlier Studies

There have been a large number of theoretical and experimental studies on inferring three-dimensional current systems in the ionosphere. The model estimating the intensity of the ionospheric current in the system is usually the sheet current approximation (Baumjohann et al., 1980; Brekke et al., 1974; Chapman and Bartels, 1940; Nagata and Fukushima, 1971). Ground-based magnetometers have been the primary instrument to study the three-dimensional current system (e.g. Kisabeth and Rostoker, 1971; 1973). The combination of the ground magnetometer with another instrument (e.g. an incoherent radar) was also used to study the three-dimensional current system (Baumjohann et al., 1980; 1981; Brekke et al., 1974). There are several problems in the past work. First of all, it is the concept of " equivalent " current or the sheet current approximation. It represents the observed magnetic perturbations on the ground and is not the current overhead in the auroral region of the ionosphere. Nevertheless this concept was used to derive the current system ( Baumjohann et al., 1980; 1981; Kisabeth, 1979; Kamide et al., 1981) or to compare a current system with the observation (Brekke, 1974). Second, field-aligned currents could not be obtained and so they are ignored (Baumjohann et al., 1980; 1981; Brekke et al., 1974). Third, the very good agreement was only obtained for the northward component of the observed magnetic perturbation when comparing the calculation with the observation (Brekke, 1974). The analysis method developed here overcame all those problems.

The method used here is also different from the earlier studies. The "Forward" method (Kisabeth, 1979) used ground-based magnetometer data as input and assumed a ratio between Pedersen and Hall conductivities. A linear inversion was used to solve the three-dimensional current system. The KRM method (Kamide et al., 1981) also used the ground-based magnetic data as inputs and assumed a ratio of Pedersen and Hall conductivities. A partial differential equation was used to solve the electrostatic potential. The horizontal ionospheric current was obtained by Ohm's law and the field-aligned currents were obtained by solving the current continuity equation. In the analysis method here, the electric field measured from the BARS and the height-integrated Pedersen and Hall conductivities estimated from the auroral emission rates I(427.8nm) and I(630.0nm) observed by the ASI are inputs. Ohm's law is used to find the horizontal ionospheric current and the current continuity is used to find the vertical field-aligned currents.

It is found that the current system constructed here is a combination of two

Boström types of current system in a small scale since Boström types of current system distribute infinitely in the auroral oval. In the three cases selected here, the current along the arc is a W-E Hall current and is closed by the upward and downward field-aligned currents for the quiet auroral arc. The northward or southward component of the horizontal current is Pedersen current and closes the two sheets of field-aligned currents on the north and south edges of the arc for the distorted arc. For the combination of the quiet and distorted arcs the current system is the combination of the corresponding two situations.

The three-dimensional current system constructed is within the BARS field of view which is a small region relative to the whole auroral oval. In addition, whether or not this system in this case is independent of the other currents in the oval is an open question, since the early theories and experimental studies tried to show that the west-east component of the ionospheric current should be continuous in the oval (such as Boström, 1964; Brekke et al, 1974; Kamide et al, 1981; Kisabeth, 1979 and so on). However, Timofeev et al.(1990) constructed an extended Boström current loop model -- "Matreshka" model, which is the hierarchy of three encircled two sheet Boström current loops of different sizes shown in Figure 1.5. The smallest loop is within an auroral arc, which is very similar to the current system constructed here for the N-S scale, but it still has a problem of the E-W scale of the current system.

For the three cases in the evening sectors, the horizontal ionospheric current obtained is mainly northwestward or southwestward current since the electric fields were observed mainly southwestward. However, the northeastward ionospheric current was also obtained for the case on March 21 of 1990 when the electric field was observed northeastward in the lower region relative to the arc. Comparing it with the results of the " Forward " and KRM methods and other models, such as Figure 1.2, it is known that these cases are in the local time region after the Harang discontinuity, so the Hall current penetrates from the postmidnight to the premidnight region. One case shows that there is an eastward Hall current at the lower region to the arc which connects to the westward current, seen in Figure 4.4.3. It was also found that the ionospheric current is located within the auroral arc when the conductivities in the arc are significantly enhanced. Tsunoda and Presnell (1976) questioned whether the primary electrojet current flows within visual arcs. Some evidence showed an anticorrelation between the magnitude of the ionospheric electric field and particle precipitation (Aggson, 1969; Wescott et al., 1969; Maynard et al., 1973; Tsunoda and Presnell, 1976b). For the spiral case on Feb.24 of 1990, the result of the counterclockwise ionospheric current shows enhanced intensities and a similar rotational sense of the spiral which agrees with the result of Untiedt et al. (1978). For the locally intensified cases on Feb.25 of 1990 and March 21 of 1990, the locally intensified aurora existed in the arc and the arc in the W-E direction was distorted. The ionospheric current under this circumstance was enhanced locally and also flowed counterclockwise around that area, which has not been found in any references except spiral cases. For the field-aligned currents, the results have shown a combination of two types of Boström field-aligned currents within a small region. They distribute not only poleward or equatorward but also along the arc, which is different from the earlier work, such as the " Forward " method and KRM method. The reason is that the earlier work was all based on the large scale of the whole auroral oval. It is noticed that the magnitudes of the field-aligned currents required for the spiral agree with the spiral theory (Hallinan, 1976) but the observed electric field in that area is not up to or over 100 V/m as given by the theory. According to the theory, the field-aligned current in the spiral should be all upward, but the result here shows that there is also a downward current existing within that region. The same result was obtained for the distorted arc.

## 5.2 Summary

In this thesis, an algorithm was developed to construct a three-dimensional current system within the BARS field of view of the auroral region in the ionosphere. A background conductivity was assumed and conductivities in the arc were computed from the intensities of the two wavelengths 427.8nm and 630.0nm using equations (3.3), (3.4), (3.5) and (3.6). The auroral emission for the wavelength of 557.7nm was not needed in this situation. By combining the Pedersen and Hall conductivities calculated above with measured BARS data from which electric field vectors were deduced, 400 horizontal ionospheric electric current vectors and vertical field-aligned current vectors within the field of view could be calculated and a three-dimensional current system within a small region was inferred. The current system was tested by determining the perturbation produced by all those 400 ionospheric current vectors and field-aligned current vectors at the Gillam station and the Back station and comparing with the magnetic observation from the MARIA. Three cases were chosen here and the results of the comparison have been shown in the last chapter. The three cases used for analysis are all in the evening time before midnight. The aurora in each case is rather disturbed and not uniform at most times. The $k_p$ index during the time period discussed in each case is 5+, 5 and 6-. The aurora for the wavelength of 427.8nm is very important in the data analysis, since it can be an identification of an auroral arc to classify cases. The data analysis and discussions of the three cases can be summarized as follows:

(1) The observed electric field vectors in all the cases change spatially and temporally. The electric fields are observed mainly in the north side of the arc and in the arc, and sometimes also to the south of the arc. The electric field vectors on the north side of the arc mainly point toward the southwest and those on the south side toward the north when they exist. The electric field vectors inside the arc mainly cross the arc in the southwestward direction for the quiet situation but point toward the centre of the spiral pattern for the spiral situation.

(2) The calculated ionospheric current vectors are distributed in two regions, outside the arc and inside the arc. The current vectors outside the arc are on the north side and very small compared to the ones in the arc when the aurora for the wavelength of 427.8nm is more intense than that for the wavelength of 630.0nm. In other words, the horizontal ionospheric current is confined to the arc region whenever the conductivities in the arc are significantly enhanced.

(3) The calculated ionospheric current vectors outside the arc mainly flow

counterclockwise around the edge of the arc and those in the aurora also flow counterclockwise around the most intensive portion of the arc when the arc is distorted, otherwise the flow is along the arc in nearly westward direction when the arc is more quiet, which means that there is a N-S component of the ionospheric current for the distorted arc and only a component along the arc for the quiet situation.

(4) The calculated upward and downward field-aligned currents distribute in two regions, outside the auroral arc and inside the arc. The currents outside the arc generally are very small and the currents inside the arc are mainly in two sheets, upward current is on one side and downward is on the other side. For the quiet arc the upward field-aligned current is located at the west side and downward field-aligned current at the east side since the ionospheric current flows in the westward direction. When the arc is distorted and more intense locally at certain points the upward field-aligned current is usually on the north side and downward current is on the south side or vice-versa according to the location of this intensive part. The upward and downward field-aligned currents and the ionospheric current consist of a three-dimensional current system in a small region of the ionosphere and satisfy the current continuity. The resulting current system is a combination of two types of Boström current system in a small region.

(5) The calculated perturbation produced by the calculated ionospheric and

field-aligned current vectors have time variations that agree with the observations by the MARIA, especially when the calculated current is about overhead the station where the perturbation is calculated. There are some disagreements when the current is away from the station, which can result from additional currents located near the station that may affect the perturbation there strongly. In magnitude, there is a factor difference between the calculated and observed perturbations, the calculated perturbation is smaller than the observed perturbation. There are several reasons to be considered for this.

(6) From our analysis above it is obvious that the perturbation on the ground is mainly caused by the overhead ionospheric current and field-aligned current in the BARS field of view. However the currents outside the BARS field of view may also affect the perturbation at a certain station on the ground when they are close to the station. So, it can be said that the overhead ionospheric current and field-aligned current in the auroral region is the main source which produces the perturbation on the ground.

## 5.3 Further Work

So far, by combining and utilizing the ASI and BARS data, a three-dimensional current system was constructed by means of Ohm's law and the current continuity. The result was examined by converting the current to a magnetic perturbation and then comparing it with the magnetic observation from MARIA. After the comparison, it is found that there is a very good agreement on the time variation of the perturbations for each other. However, the absolute value of the calculated perturbation is much smaller than the observation. The reason may be due to the BARS measurements, and especially the extent of the calculated ionospheric current and field-aligned current. Further analysis should be undertaken.

# REFERENCES


Aggson, T. L., Probe measurements of electric fields in space, in **Atmospheric Emissions**, edited by B. M. McCormac, P. 305, Van Nostrand Reinhold, New York, 1969.

Akasofu, S.-I., C. R. Wilson, L. Snyder, P. D. Perreault, Results from a meridian chain of observatories in the Alaskan sector(1), **Planet. Space Sci.**, **19**, 477, 1971.

Akasofu, S.-I., Y. Kamide and J. Kisabeth, Comparison of two modelling methods for three-dimensional current systems, **J. Geophys. Res.**, **86**, 3389, 1981.

Alfven, H., A theory of magnetic storms and of the aurora, **1. Kgl. Sv. Vetenskapsakad. Handl. Ser. 3**, **18**, pp.1-39, 1939 (Partial reprint, EOS Trans. AGU, **51**, 181-193, 1970).

Araki, T., K. Schlegel and H. Luhr, Geomagnetic effects of the Hall and Pedersen current flowing in the auroral ionosphere, **J. Geophys. Res.**, **94**, 17185, 1989.

Armstrong, J. C., S. -I. Akasofu and G. Rostoker, A comparison of satellite observations of Birkeland currents with ground observations of visible aurora and ionospheric currents, **J. Geophys. Res.**, **80**, 575, 1975.

Atkinson, G., The current system of geomagnetic bays, **J. Geophys. Res.**, **72**, 6063, 1967.

Baumjohann, W., Ionospheric and field-aligned current systems in the auroral zone: a concise review, **Adv. Space Res.**, **2**, 55, 1983.

Baumjohann, W., J. Untiedt and R. A. Greenwald, Joint two-dimensional observations of ground magnetic and ionospheric electric fields associated with auroral zone currents, 1. three-dimensional current flows associated with a substorm-intensified eastward electrojet, **J. Geophys. Res.**, **85**, 1963, 1980.

Baumjohann, W., R. J. Pellinen, H. J. Opgenoorth and E. Nielsen, Joint two-dimensional observations of ground magnetic and ionospheric electric fields associated with auroral zone currents: current systems associated with local auroral break-ups, **Planet. Space Sci.**, **29**, 4, 431, 1981.

Birkeland, K., The Norwegian aurora polaris expedition 1902-1903Aschehoug, Christiana, 1908.

Birkeland, K., The Norwegian aurora polaris expedition 1902-1903, Vol. 1, On the cause of magnetic storms and the origin of terrestrial magnetism, sect. 2, H. Aschehong, Christiania, Norway, 1913.

Boström, R., A model of the auroral electrojets, **J. Geophys. Res.**,**69**,4983, 1964.

Brekke, A., J. R. Doupnik and P. M. Banks, Incoherent scatter measurements of E region conductivities and current in the auroral zone, **J. Geophys. Res.**, **79**, 3773, 1974.

Brekke, A., and C. Hall, Auroral ionospheric quiet summer time conductances, **Ann. Geophysicae**, **6**, 361, 1988.

Chapman, S., An outline of a theory of magnetic storms, **Proc. Roy. Soc.**, London, **95**, 61, 1918.

Chamberlain, J. W., **Physics of the aurora and airglow**, Academic Press, 1961.

Chapman, S. and Bartels, J., **Geomagnetism**, Vol.1, Clarendon Press, Oxford, 1940.

Czechowsky, P., Calculation of an equivalent current system in the polar E region, **Radio Sci.**, **6**, 247, 1971.

de la Beaujardière, O., M. J. Baron, V. B. Wickwar, C, Senior, and J. V. Evans, MITHRAS: A program of simultaneous radar observations of the high-latitudeauroral zone, **Contract report F49620-81-C-0042**, SRI International, Menlo Park, California, 1982.

Fukushima, N., Electric current systems of polar substorms and their magnetic effect below and above the ionosphere, **Radio Sci.**, **6**, 269,1971.

Hallinan, E. J., Auroral Spirals, **J. Geophys. Res.**, **81**, 3959, 1976.

Hughes, T. J., and G. Rostoker, Current flow in the magnetosphere and ionosphere during of moderate activity, **J. Geophys. Res.**, **82**, 2271, 1977.

Hughes, T. J., and G. Rostoker, A comprehensive model current system for high-latitude magnetic activity, 1, The steady state system, **Geophys. J. R. Astron. Soc.**, **58**, 525, 1979.

Iijima, T., and T. A. Potemra, The amplitude distribution of field-aligned currents at northern high latitude observed by Triad, **J. Geophys. Res.**, **81**, 2165, 1976.

Kamide, Y. and Brekke, A., Auroral electrojet current density deduced from the Chatanika radar and from the Alaska meridian chain of magnetic observations, **J. Geophys. Res., 80**, 587, 1975.

Kamide, Y. and Akasofu, S.-I, The auroral electrojet and global auroral features, **J. geophys. Res., 80**, 3585, 1975.

Kamide, Y., M. Kanamitsu and S.-I. Akasofu, A new method of mapping worldwide potential contours for ground magnetic perturbations: Equivalent ionospheric current presentation, **J. Geophys. Res., 81**, 3810, 1976.

Kamide, Y. and G. Rostoker, The spatial relationship of field-aligned currents and auroral electrojets to the distribution of nightside auroras, **J. Geophys. Res., 82**, 5589, 1977.

Kamide, Y., A. D. Richmond and S. Matsushita, Estimation of ionospheric electric fields, ionospheric currents and field-aligned currents from ground magnetic records, **J. Geophys. Res.,86**, 801, 1981.

Kamide, Y., S.-I. Akasofu, B.-H. Ahn, W. Baumjohann and J. L. Kisabeth, Total current of the auroral electrojet estimated from the IMS Alaska meridian chain of magnetic observations, **Planet. Space Sci., 30**, 621, 1982a.

Kamide, Y., A. D. Richmond, Ionospheric conductivity dependence of electric fields and currents estimated from ground magnetic observations, **J. Geophys. Res.,87**, 8331, 1982b.

Kisabeth, J. L., and G. Rostoker, Development of the polar electrojet during polar magnetic substorms, **J. Geophys. Res.,76**, 6815, 1971.

Kisabeth, J. L. and Rostoker, G., Current flow in auroral loops and surges inferred from ground-based magnetic observations, **J. geophys. Res., 78**, 5577, 1973.

Kisabeth, J. L., and G. Rostoker, The expansive phase of magnetospheric substorms, 1. Development of the auroral electrojets and auroral arc configuration during a substorms, **J. Geophys. Res.,79**, 972, 1974.

Kisabeth, J. L., On calculating magnetic and vector potential fields due to large-scale magnetospheric current systems and induced currents in an infinitely conducting earth, in **Quantitative modelling of magnetospheric processes, Geophys. Monogr. Ser.**, vol. 21, p.473, edited by W. P. Olson, Washington, D. C., 1979.

Lin, C. S., and R. A. Hoffman, Characteristics of the inverted V event, **J. Geophys. Res., 84**, 1514, 1979.

Loginov, G. A., E. P. Vasilev, and A. Grafe, Some results of the investigation of magnetic variations of the auroral electrojets concluded from observations of the geomagnetic meridian project (GMP), **Gerlands Beitr. Geophys.**, **87**, 249, 1978.

Maurer, H. and B. Theile, Parameters of the auroral electrojet from magnetic variations along a meridian, **J. Geophys. Res.**, **44**, 415, 1978.

Maynard, N. C, A. Bahnson, P. Christopherson, A. Egeland, and R. Lundin, An example of anticorrelation of auroral particles and electric fields, **J. Geophys. Res.**, **78**, 3976, 1973.

McNamara, A. G., D. R. McDiarmid, G. J. Sofko, J. A. Koehler, P. A. Forsyth, and D. R. Moorcroft, BARS - a dual bistatic auroral radar system for the study of electric fields in the Canadian sector of the auroral zone, **Adv. Space Res.**, **2**, 145, 1983.

Metha, N. C., Ionospheric electrodynamics and its coupling to the magnetosphere, **Ph. D. thesis**, Univ. of Calif., San Diego, 1979.

Nagata, T. and Fukushima, N., Morphology of magnetic disturbance, in **Encyclopedia of Physics**, Vol.49,PP.5-130, Springer, New York, 1971.

Oldenburg, D. W., A quantitative technique for modelling ionospheric and magnetospheric current distributions, **J. Geophys. Res.**, **83**, 3320, 1978.

Omholt, A., The optical aurora, Springer-Verlag, Berlin, 1971.

Pao, Qi, A thesis of **The physical processes of auroral arcs**, U of C, 1991.

Rasmussen, C. E., R. W. Schunk, and V. B. Wickwar, A photochemical equilibrium model of ionospheric conductivity, Submitted to **J. Geophys. Res.**, 1987.

Rees, M. H., and D. Luckey, Auroral electron energy derived from ratio of spectroscopic emissions, 1. Model computations, **J. Geophys. Res.**, **79**, 5181, 1974.

Rees, M. H. and R. G. Roble, excitation of O('D) atoms in auroral and emission of the [OI] 6300 Å line, **Can. J. Phys.**, **64**, 1608, 1986.

Rees, M. H., D. Lummerzheim, R. G. Roble, J. D. Winningham, J. D. Craven, and L. A. Frank, Auroral energy deposition Rate, Characteristic electron Energy and Ionospheric Parameters Derived from Dynamics, **J. Geophys. Res.**, **93**, 12841, 1988.

Rostoker, G., and M. Hron, The eastward electrojet in the dawn sector, **Planet. Space Sci.**, **23**, 1377, 1975.

Rostoker, G. and Hughes, T. J., A comprehensive model current system for high-latitude magnetic activity-II, the substorm component, **Geophys. J. R. astr. Soc.**, **58**, 571, 1979.

Robinson, R. M. and R. R. Vondrak, Measurements of E region ionization and conductivity produced by solar illumination at high latitudes, **J. Geophys. Res.**, **89**, 3951, 1984.

Robinson, R. M., R. R. Vondrak, K. Miller, T. Dabbs, and D. Hardy, On calculating ionospheric conductances from the flux and energy of precipitating electrons. **J. Geophys. Res.**, **92**, 2565,1987.

Schlegel, K., Auroral zone E-region conductivities during solar minimum derived from EISCAT data, **Ann. Geophysicae**, **6**, 129, 1988.

Scrase, F. J., The electric current associated with polar magnetic substorms, **J. Atmos. Terr. Phys.**, **29**, 567, 1967.

Senior, C., Les conductivitéionosphériques et leur rôle dans la convection magnétosphérique:Une étude expérimentale et théorique, Diplôme de docteur de 3$^{e}$ cycle, Univ. Pierre et Marie Curie, Paris, 1980.

Steele, D. P., and D. J. McEwen, Electron auroral excitation efficiencies and intensity ratios, **J. Geophys. Res.**, **95**, 10321, 1990.

Timofeev, E. E. and Yu. I. Galperin, Convection and currants in stable auroral arcs and inverted-vs, submitted to special issue of **J. of Geom. and Geoel.: proceedings of the 7th quadrennial STP symposium**, the Hague, Netherlands, June 25-30, 1990.

Tsunoda, R. T. and R. I. Presnell, Relationship of radar aurora, visual aurora, and auroral electrojets in the evening sector, **J. Geophys. Res.**, **81**, 6005, 1976a.

Tsunoda, R. T., R. I. Presnell, and T. A. Potemra, The spatial relationship between the evening radar aurora and field-aligned currents, **J. Geophys. Res.**, **81**(22), 3791, 1976b.

Vallance Jones, A., Aurora, D. Reidel Pub. Co., Dordrecht-Holland, 1974.

Vallance Jones, A., et al., CANOPUS, an automatic ground-based instrumentation array to support space projects, scientific objectives and system description, Space

Division, **Natl. Res. Counc. (Canada), Ottawa**, 1986.

Vickrey, J. F., R. R. Vondrak, and S. J. Matthews, The diurnal and latitudinal variations of auroral zone ionospheric conductivity, **J. Geophys. Res.**, **86**, 65, 1981.

Vondrak, R. R., Model of Birkeland currents associated with an auroral arc, **J. Geophys. Res.**, **80**, 4011, 1975.

Vondrak, R. R., and R. Robinson. Inference of high-latitude ionization and conductivity from AE-C measurements of auroral electron fluxes, **J. Geophys. Res.**, **90**, 7505, 1985.

Walker, J. K., Space-time association of the auroral and magnetic disturbances, **J. atmos. terr. Phys.**, **26**, 951, 1964.

Wescott, E. M., J. D. Stolarik, and J. P. Heppner, Electric fields in the vicinity of auroral forms from motions of barium vapour releases, **J. Geophys. Res.**, **75**, 3469, 1969.

Wilhjelm, J., Friis-Christensen, E., Magnetometer chain in Greenland, **Geophys. Papers**, R-48, Danish Meteorol. Inst., Copenhagen 1976.

Yasuhara, F., Y. Kamide and S.-I. Akasofu, Field-aligned and ionospheric currents, **Planet. Space Sci.**, **23**, 1355, 1975.

Zmuda, A. J., and J. C. Armstrong, The diurnal flow of field-aligned currents, **J. Geophys. Res.**, **79**, 4611, 1974.